

3527
741076
2005070
TR3521

**Evolution of point defect clusters during
ion irradiation and thermal annealing**

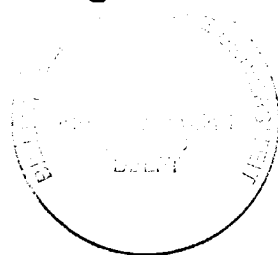


The research described in this thesis was performed within the Group Defects in Materials, Department of Reactor Physics of the Interfaculty Reactor Institute, Delft University of Technology, Mekelweg 15, 2629 JB, Delft, The Netherlands.

This research was performed within the framework of the European Fusion Technology Programme with financial support from the European Commission and the Netherlands Ministry of Economic Affairs

Evolution of point defect clusters during ion irradiation and thermal annealing

PROEFSCHRIFT



ter verkrijging van de graad van doctor
aan de Technische Universiteit Delft,
op gezag van de Rector Magnificus prof.ir. K. F. Wakker,
in het openbaar te verdedigen ten overstaan van een commissie,
door het College voor Promoties aangewezen,

op dinsdag 23 mei 2000 te 16.00 uur

door

Alexander Valerievich FEDOROV

Engineer in Experimental Nuclear Physics van het
Moscow Engineering Physics Institute, te Moskou in Rusland,
geboren te Moskou, Rusland

Dit proefschrift is goedgekeurd door de promotoren:

Prof.dr. A. van Veen

Prof.dr.ir. H. van Dam

Samenstelling promotiecommissie:

Rector Magnificus,	voorzitter
Prof.dr. A. van Veen	RU Groningen, promotor
Prof. dr. ir. H. van Dam	Technische Universiteit Delft, promotor
Prof. dr. D.O. Boerma	RU Groningen
Prof. dr. H. W. Zandbergen	Technische Universiteit Delft
Prof. dr. ir. C. W. E. van Eijk	Technische Universiteit Delft
dr. A.I. Ryazanov	RRC "Kurchatov Institute", Rusland
ir. J. G. van der Laan	NRG Petten

Published and distributed by:

Delft University Press
P.O. Box 98
2600 MG Delft
The Netherlands
Telephone: +31 15 2783254
Telefax: +31 15 2781661
E-mail: DUP@Library.TUDelft.NL

ISBN 90-407-2050-9

Copyright 2000 by A.V. Fedorov

All rights reserved. No part of the material protected by this copyright notice may be reproduced or utilized in any form or by any means, electronic or mechanical, including photocopying, recording or by any information storage and retrieval system, without written permission from the publisher: Delft University Press.

Printed in The Netherlands

To my parents

TABLE OF CONTENTS

Table of contents	VII
List of symbols	XI
List of publications	XIII
1. Introduction	1
2. Computer simulation of defect evolution: MODEX	5
Introduction	5
2.1. Physical model	6
2.2. Program algorithm and flow chart	15
2.3. Example of simulation: Helium-vacancy clustering in molybdenum	20
Conclusions	22
3. Experimental	23
Introduction	23
3.1. Thermal desorption technique	24
3.1.1. First-order desorption model	24
3.1.2. Apparatus	27
3.1.3. Data acquisition: Program DEC&DAP	29
3.1.4. Data processing. Program DECO	33
3.2. DANFYSIK accelerator	37
3.2.1. Apparatus	37
3.2.2. Control of the separation magnet: Program SMAC	39
3.3. Positron Beam Analysis	40

4. Helium traps in vanadium alloys and their thermal stability	43
Introduction	43
4.1. Helium trapping at room temperature implantation	44
4.2. Thermal stability of helium traps in vanadium alloys	52
4.3. Helium trapping at precipitates	55
Conclusions	60
5. Deuterium trapping in beryllium and beryllium pre-implanted with helium	61
Introduction	61
5.1. Deuterium trapping in Be	62
5.2. Deuterium in Be pre-implanted with He	64
Conclusions	67
6. Tritium retention in ceramic breeding materials	69
Introduction	69
6.1. Physical model and basic assumptions	71
6.2. Fitting to experiment. Results and discussion	78
Conclusions	81
7. Nanosize cavities in silicon and MgO	83
Introduction	83
7.1. Threshold implantation dose for nanocavity formation in Si	84
7.2. Interaction of cavities in Si with self-interstitials	87
7.3. Creation of nanocavities in MgO by helium and deuterium implantation	92
7.4. Permeation of deuterium from nanocavities formed in MgO and Si	96
Conclusions	100

Appendix A. Stationary diffusion equation	101
Appendix B. Non-stationary diffusion equation	105
Appendix C: Groups of clusters	107
Appendix D: Trapping at unstable sinks	111
Summary	115
Samenvatting	119
References	123
Acknowledgements	131
Curriculum vitae	135

X

LIST OF SYMBOLS

α	point defect type (= V, He, X, I), where V is vacancy He is helium or other implanted ion X is interstitially dissolved impurity I is self – interstitial	
β	defect cluster structure : (V_n , He_m , X_k , I_l), where n – number of vacancies m - number of helium atoms k - number of impurities l – number of self-interstitials	
C_α	concentration of point defects of type α	$[\text{cm}^{-3}]$
C_β	concentration of defect clusters of type β	$[\text{cm}^{-3}]$
D_α	$D_\alpha = D_{\alpha 0} \exp(-E_\alpha^m/kT)$ - diffusion coefficient of point defect of type α	$[\text{cm}^2\text{s}^{-1}]$
E_α^m	migration energy	$[\text{eV}]$
S_α	source of point defects of type α	$[\text{cm}^{-3}\text{s}^{-1}]$
K_α	trapping rate of point defects of type α	$[\text{s}^{-1}]$
$Z_{\alpha,\beta}$	sink strength of an isolated defect cluster of type β for point defect of type α	$[\text{cm}^{-2}]$

$R_{\alpha\beta}$	trapping radius of cluster of type β for point defect of type α	[cm]
I_{α}	implantation rate for $\alpha = \text{He}$ and Frenkel pair production rate for $\alpha = \text{V, I}$	[cm ⁻³ s ⁻¹]
$Q_{\alpha\beta}$	dissociation rate of point defect α from cluster type β	[s ⁻¹]
$v_{\alpha\beta}$	attempt frequency	[s ⁻¹]
$E_{\alpha\beta}^{\text{diss}}$	dissociation energy of point defect of type α from defect cluster of type β	[eV]
$M_{\beta\beta'}$	trap-mutation rate of cluster type β' to cluster β	[s ⁻¹]
Σ_{α}	number of point defects of type α originated in the sample during time step Δt	[cm ⁻²]
Ω_{α}	number of point defects of type α released through the outer surface during time step Δt	[cm ⁻²]
$\Theta_{\alpha,j}$	number of point defects of type α trapped in layer j during time step Δt	[cm ⁻²]
P_{α}^R	release probability for point defect of type α	
$P_{\alpha\beta}^{\text{tr}}$	layer trapping probability (to be trapped in layer j)	
$P_{\alpha\beta}^{\text{tr}}$	cluster trapping probability (to be trapped by cluster β)	
$N_{\beta,j}$	population of clusters of type β in layer j	

LIST OF PUBLICATIONS

Chapter 2

A. V. Fedorov, A. van Veen and J. Th. De Hosson, MRS fall Meeting 1996 .Mat. Res. Soc. Symp. Proc., Editors I. M. Robertson, G. S. Was, L. W. Hobbs, T. D. de la Rubia, **439** (1997) 383-388.

A.V. Fedorov and A. van Veen, Computational Materials Science **9** (1998) 309-324.

Chapter 4

A. V. Fedorov, G. P. Buitenhuis, A. van Veen, A. I. Ryazanov, J. H. Evans, W. van Witzenburg, K. T. Westerduin. Journal of Nuclear Materials **227** (1996) 312-321.

A. V. Fedorov, A. van Veen, A. I. Ryazanov. J. Nucl. Mat. **233-237** (1996) 385-389.

A. van Veen, A. V. Fedorov, A. I. Ryazanov, Proceedings, 2nd Workshop on Vanadium Alloy Development for Fusion, IEA Vanadium Alloy Working Group ECN Petten, 20-22 May 1996, The Netherlands, editor E.V. van Osch, 47-48.

A. V. Fedorov, A. van Veen, A. I. Ryazanov, The 8th International Conference on Fusion Reactor Materials, October 26-31 1997, Japan (Sendai), J. of Nuclear Materials **258-263** (1998) 1396-1399.

A. van Veen, A. V. Fedorov, A. I. Ryazanov, The 8th International Conference on Fusion Reactor Materials, October 26-31 1997, Japan (Sendai), J. of Nuclear Materials, **258-263** (1998) 1400 – 1403.

Chapter 5

A. V. Fedorov, A. van Veen, G. J. Busker, Proc. of the 3rd IAE International Workshop on Beryllium Technology for Fusion, October 22-24, 1997, Mito City, Japan, Eds. H. Kawamura and M. Okamoto, 152-157.

Chapter 6

A. V. Fedorov, A. van Veen, K. Bakker, J. G. van der Laan, Computer simulation of tritium release in Li_4SiO_4 in EXOTIC experiments, Proceedings CBBI-7, NRG Report 21099/99.23482, Petten, February 1999, 6/29-38, 6-33.

Chapter 7

A. van Veen, H. Schut, A. V. Fedorov, R. A. Hakvoort and K. T. Westerduin in: Microstructure of Irradiated Materials, eds. I.M. Robertson, S.J. Zinkle, L.E. Rehn, W.J. Phythian, Materials Research Society Symposium. Proceedings **373** (1995) 499-504.

A van Veen, H. Schut, A. Rivera, A. V. Fedorov, Mat. Res. Soc. Symp. Proc., editors D.B. Poker, D.Ila, Y-S.Cheng, L.R. Harriot, T.W. Sigmon, **396** (1996) 155-160.

E. A. C. Neeft, R. J. M. Konings, A. van Veen, H. Schut, A. V. Fedorov., In Proceedings of the World Ceramics Congress and Forum on New Materials, VIII, CIMTEC- 98, (1998) 531-539.

H. Schut, A. van Veen, F. Labohm, A. V. Fedorov, E. A. C. Neeft, R. J. M. Konings, E-MRS spring meeting, 1998, Nucl. Inst. and Meth. In Phys. Res. Sect. B **147** 1-4 (1998) 212-215.

A. van Veen, H. Schut, A. V. Fedorov, E. A. C. Neeft, R. J. M. Konings, B. J. Kooi, J. Th. M. de Hosson, E-MRS spring meeting, 1998, Strasbourg, Nucl. Inst. and Meth. in Phys. Res. Sect. B **147** 1-4 (1998) 216-220.

A.V. Fedorov, A. van Veen, H. Schut, A. Rivera, 11th International Conference on Ion Beam Modification of Materials, Aug.-Sept, 1998, Amsterdam, Nucl. Instr. and Meth. in Phys. Res. Sect. B (**148**) 1-4 (1999) 289-293.

A. van Veen, H. Schut, A. V. Fedorov, F. Labohm, E. A. C. Neeft, R. J. M. Konings, 11th International Conference on Ion Beam Modification of Materials, Aug.-Sept, 1998, Amsterdam, Nuclear Instr. and Meth. in Phys. Res. Sect. B (**148**) 1-4 (1999) 768-772.

A. V. Fedorov, A. van Veen, H. Schut, MRS Meeting 1999, Mat. Res. Soc. Proc. Editors S. J. Zinkle, G. E. Lucas, R. C. Ewing, J. S. Williams, Vol. **540** (1999) 231-236.

B. J. Kooi, A. van Veen, J. Th. M. De Hosson, H. Schut, A. V. Fedorov and F. Labohm, Appl. Phys. Lett., **76**, 9 (2000) 1110-1112.

CHAPTER 1

Introduction

Materials irradiated with energetic ions experience changes in their microstructure. Through a number of mechanisms, e.g. electron excitations, ionisation and atomic collisions, a fraction of the energy of the ions is deposited in the material in the form of point defects and point defect clusters. Historically, the necessity to understand the microstructural changes in materials under irradiation arose in the nuclear power industry. In a nuclear power plant various structural components are exposed to long-term neutron irradiation, which results in the modification of their material properties, e. g. swelling, hardening, creep [Ullmaier 1984, Schroeder 1983, Trinkaus 1986]. The mechanical properties are changed not only due to the damage produced by the neutrons but also because of accumulation of helium and hydrogen due to (n,α) and (n,p) nuclear reactions. In laboratory experiments the latter effects are usually simulated by implantations with H or He ions. Another field where the irradiation induced defects are of great concern is the microelectronic industry. Ion implantation is widely used in doping semiconductor substrates and in technological processes like the “smart cut” process [Bruehl 1998], in which a thin Si layer is separated from the wafers by implantation of hydrogen, or SIMOX in which a buried oxide layer is formed in a Si substrate by making use of Separation by Implantation of Oxygen [Izumi 1998]. In all the processes where ion implantation is used the irradiation defects formed during implantation have a strong effect on the electronic properties of the materials. Despite an

apparent difference between those two fields of application the processes responsible for the structural changes in the materials are very similar.

A number of theoretical approaches have been developed to model formation and evolution of the irradiation defects. Depending on the particular task and the scale of the problem different approaches are used. The potential field around an isolated point defect embedded in a perfect lattice or a small crystallite can be defined from quantum mechanical first principle or *ab initio* calculations [Adams and Foiles 1990, Baskes *et al.* 1989]. Methods of energy minimisation or molecular dynamics are used to calculate the migration energies of point defects for various diffusion mechanisms and the formation energies of the point defect clusters [Bacon and de la Rubia 1994, Adams *et al.* 1994]. Based on this data Lattice Monte Carlo methods are used to simulate the point defect diffusion and their agglomeration in the defect clusters [De la Rubia 1996]. In another approach the concentrations of mobile point defects are described by diffusion equations. In addition, the evolution of the defect clusters is described by a set of rate equations. The latter describe the evolution of immobile defects clusters [Mansur 1994, Brailsford and Bullough 1972]. Although every approach can highlight a particular process or effect, none of the methods so far has succeeded in providing full understanding of the processes which take place in a material under irradiation. Therefore, information on the irradiation damage in materials obtained from experimental studies is of great importance.

In the present thesis a theoretical and experimental study on point defect clustering is presented. In Chapter 2 the computer program MODEX aimed at simulating the evolution of point defect clusters during ion implantation and subsequent annealing is presented. MODEX is a Monte Carlo program in which the evolution of defect clusters is simulated through a number of elementary trapping/dissociation events. However, the diffusion of mobile point defects is described by a conventional set of diffusion equations which is solved numerically. The main features of the program are the following:

- the program is able to describe the clustering process of up to four different types of mobile point defects; usually those are the host vacancy, self-interstitial, implanted ion and mobile impurity;

- the diffusion equations for the point defects are solved in the stationary or non-stationary form depending on the point defect mobility;
- the concentrations of the point defect clusters are depth dependent, so that the effect of the outer surface as a sink for the point defects is taken into account.

The experimental studies on the irradiation effects are presented in chapters 4 through 8. They deal with the microstructural changes in a wide range of materials including metals, semiconductors and insulators.

In Chapter 4 various helium traps and their thermal stability in pure vanadium and vanadium based alloys are investigated. Vanadium based alloys, particularly V-4Cr-4Ti, are considered as an alternative to conventionally used austenitic and ferritic steels for the structural components of a fusion reactor. The interest in vanadium based alloys is driven by their low activation, good high temperature performance and excellent irradiation resistance. Although many studies have been performed in recent years [Chung *et al.* 1996, Matsui *et al.* 1992, Matsui *et al.* 1996, Smith *et al.* 1996] there is still a lack of understanding of the processes which define the behaviour of the alloys under irradiation. One of the main concerns is the production and accumulation of He inside the material.

In Chapter 5 a THDS study on beryllium is presented. Beryllium is used as a plasma facing material and a neutron multiplier [Matera and Federici 1996] in the present concept of ITER (International Thermal Experimental Reactor). One of the requirements for this material is low tritium retention. However, accumulation of helium inside beryllium can create stable traps for tritium [Chernikov *et al.* 1998]. In the study presented in this thesis deuterium trapping in beryllium which contains helium bubbles is investigated.

In Chapter 6 lithium containing ceramics are considered. These materials are to be used as the tritium breeder blanket for fusion reactors [Mattas and Billone 1996]. In the framework of the EXOTIC (EXtraction Of Tritium In Ceramics) programme an extensive study on a number of Li containing ceramics was carried out at ECN in Petten [Kwast *et al.* 1995]. In this chapter an analytical model describing tritium production and retention in Li_4SiO_4 in two different types of experiments from the EXOTIC programme is

presented. The model was used to fit the experimental data and to derive a number of important parameters including the diffusion coefficient of tritium in Li_4SiO_4 .

Among the materials of interest for microelectronics Si and MgO were studied in Chapter 7. In both materials formation and stability of nanosize cavities were investigated. Gettering of impurities on the inner surface of the cavity wall in Si is proposed as a promising way to purify the Si matrix far below the solubility levels [Follstaedt *et al.* 1996]. Nanocavities in MgO can be used to form metal nanoclusters which are known to change the optical properties [Chakraborty 1998, Zimmerman *et al.* 1998, White *et al.* 1998].

Various experimental techniques were used in this study: Thermal Helium Desorption Spectrometry (THDS), Positron Beam Analysis (PBA) and Neutron Depth Profiling (NDP). A detailed description of the THDS technique is presented in Chapter 3.

Most of the experimental studies were supported by computer simulations carried out with the program MODEX which proved to be helpful in the analyses of the experimental results as demonstrated in chapters 2, 4 and 7.

CHAPTER 2

Computer simulation of defect evolution: MODEX

Introduction

The program MODEX presented in this chapter aims at simulating the evolution of defect clusters in great detail both during ion implantation and subsequent annealing. As input the program uses the stopped ions and damage profiles generated by TRIM calculations [Ziegler *et al.* 1985] or profiles obtained from other sources, theoretical or experimental. The program also requires the following information about the irradiated material: diffusivities of the point defects and a list of dissociation energies for the defect clusters obtained from MD calculations, thermodynamic calculations or from experiments. The number of mobile point defect types is restricted to four, e.g. implanted ions, vacancies, self-interstitials and interstitially dissolved impurities. The transport of the point defects is described by solving the one-dimensional diffusion equation. The defect clusters are considered as an agglomeration of the same four types of point defects in any possible combination. Thus vacancy type defects and interstitial loops can be considered. The evolution of the defect clusters is simulated through a number of elementary trapping or dissociation events (reactions) which take place in a material under certain irradiation or thermal annealing conditions. Section 2.1 discusses the physical model and the equations involved in the program. In Section 2.2 the algorithm

and the flow chart of the program are presented. Section 2.3 presents a demonstration of the simulation of helium-vacancy clustering in molybdenum.

The program provides a versatile tool to test various physical models during the analysis of the experimental data, e. g. THDS spectra.

2.1 Physical model

During implantation the implanted ions stop inside the sample at a certain depth depending on their energy and the properties of the material. At sufficiently high irradiation energies, Frenkel pairs, i.e. vacancies and self-interstitials, are created. Profiles of both stopped ions and Frenkel pairs can be obtained from independent calculations, e.g. with the help of the TRIM simulation. Depending on the irradiation temperature any of the point defects introduced by implantation can be mobile. The penetration depth of the ions is usually much less than the characteristic size of the area under irradiation. Therefore, the diffusion of the point defects will be considered as one-dimensional. The transport of the point defects of type α is described by the following diffusion equation:

$$\frac{\partial C_\alpha}{\partial t} = D_\alpha \frac{\partial^2 C_\alpha}{\partial x^2} + S_\alpha(x) - K_\alpha(x)C_\alpha, \quad (2.1)$$

with homogeneous radiative boundary conditions:

$$\left. \frac{dC_\alpha}{dx} \right|_{x=0} - \frac{1}{L_a} C_\alpha \Big|_{x=0} = 0, \quad (2.2)$$

$$\left. \frac{dC_\alpha}{dx} \right|_{x=l} + \frac{1}{L_d} C_\alpha \Big|_{x=l} = 0 \quad (2.3)$$

at the surface and depth l , respectively. The initial value condition is:

$$C_{\alpha}(x, t = 0) = C_{\alpha, 0}(x), \quad (2.4)$$

where $C_{\alpha}(x, t)$ is the volume concentration of the point defects with $\alpha = \text{He, V, I, X}$. Indices V, I and X denote vacancies, self-interstitials, and interstitially dissolved impurities, respectively. It is assumed that implantation is carried out with helium ions, $\alpha = \text{He}$, but there is no restriction in the program on the type of the implanted ions provided the boundary conditions 2.2-2.3 are valid. D_{α} is the diffusion coefficient: $D_{\alpha} = D_{\alpha 0} \exp(-E_{\alpha}^m / (kT))$, where E_{α}^m is the migration energy, k is the Boltzmann constant and T is the absolute temperature in Kelvin. $L_a \sim 0.15 \text{ nm}$ is of the order of the jump length of the point defect. l is the depth location of the boundary beyond which no irradiation induced defects are expected and is usually chosen a few times larger than the mean stopping range of the implanted ions. L_d is the diffusion length of the mobile defects in the bulk while no irradiation-induced defects are present. Usually $L_d \sim 500 \text{ nm}$ is taken to account for trapping at pre-existing defects. This choice of the parameters L_a and L_d describes the boundary conditions which are typical for THDS experiments.

The second term on the right-hand side in Eq. 2.1 represents the source of the point defects and has the following form:

$$S_{\alpha}(x) = I_{\alpha}(x) + \sum_{\beta} C_{\beta} Q_{\alpha\beta}, \quad (2.5)$$

where $I_{\alpha}(x)$ is the depth dependent ion implantation rate for $\alpha = \text{He}$, and the creation rate of Frenkel pairs for $\alpha = \text{V, I}$. C_{β} is the depth dependent concentration of clusters of type β with $\beta = (\text{He}_n, \text{V}_m, \text{I}_k, \text{X}_l)$. Indices n, m, k, l denote the number of point defects of appropriate type constituting the cluster. The second term in Eq. 2.5 describes the dissociation of the point defects of type α from the defect clusters of type β with the dissociation rate:

$$Q_{\alpha\beta} = q_{\alpha\beta} \exp\left(-\frac{E_{\alpha\beta}^{\text{diss}}}{kT}\right), \quad (2.6)$$

where $E_{\alpha\beta}^{diss}$ is the dissociation energy for the reaction: $\beta \rightarrow \alpha + \beta'$. The pre-exponent factor $q_{\alpha\beta} = n_{\alpha\beta}v_{\alpha\beta}$ is the product of the attempt frequency $v_{\alpha\beta}$ and the number of point defects $n_{\alpha\beta}$ of type α accumulated in the defect cluster. The dissociation parameters $E_{\alpha\beta}^{diss}$ and $v_{\alpha\beta}$ can be obtained from MD calculations [Adams *et al.* 1994, Adams and Wolfer 1989, Reed 1977], thermodynamic models [Mills 1980] or experiments [Van Gorkum and Kornelsen 1979, Fedorov *et. al* 1996].

The third term on the right-hand side of Eq. 2.1 describes the trapping of the point defects at the clusters. The trapping rate K_α has the following form:

$$K_\alpha = \sum_\beta C_\beta Z_{\alpha\beta}, \quad (2.7)$$

where $Z_{\alpha\beta}$ is the specific trapping rate of the cluster type β for the mobile point defect type α . $Z_{\alpha\beta}$ is defined for every combination of α and β . In the diffusion limited approximation [Brailsford and Bullough 1972], and disregarding the interactions between different sinks, $Z_{\alpha\beta}$ can be written as follows:

$$Z_{\alpha\beta} = 4\pi R_{\alpha\beta} D_\alpha, \quad (2.8)$$

where $R_{\alpha\beta}$ is the effective trapping radius of the cluster type β for the point defect α .

From the set of equations 2.1-2.8, concentrations of the point defects C_α can be obtained provided the cluster concentrations C_β are known. The specific trapping rates $Z_{\alpha\beta}$ and the dissociation rates $Q_{\alpha\beta}$ are functions of temperature and assumed to be known. The numerical solutions of the boundary-value problem Eqs. 2.1-2.8 for stationary and non-stationary cases are given in Appendix A and Appendix B, respectively.

The system of rate equations describing cluster evolution with time in the most general form can be written as follows:

$$\begin{aligned} \frac{dC_\beta}{dt} = & \sum_{\alpha\beta'}' Z_{\alpha\beta'} C_\alpha C_{\beta'} + \sum_{\alpha\beta'}' C_\beta Q_{\alpha\beta'} + \sum_{\beta'}' C_\beta M_{\beta\beta'} \\ & - \sum_\alpha Z_{\alpha\beta} C_\alpha C_\beta - \sum_\alpha C_\beta Q_{\alpha\beta} - \sum_{\beta'} C_\beta M_{\beta'\beta}, \end{aligned} \quad (2.9)$$

where the only undefined coefficient $M_{\beta\beta'}$ so far is the rate of trap mutation events during which cluster β changes into β' (For example $V_2I \rightarrow V$). The first term on the right-hand side of Eq. 2.9 describes the increase of the concentration C_β due to trapping of the defects of type α at clusters of type β' yielding clusters of type β : $\alpha + \beta' \rightarrow \beta$. The second term represents the dissociation reaction yielding clusters of type β : $\beta' \rightarrow \alpha + \beta$. The third term represents all the trap mutations, e. g. by loop punching, resulting in clusters of type β : $\beta' \rightarrow \beta + \beta''$. The prime over the first three sums indicates that the summation is taken only over the reactions which yield clusters with the structure β . The last three terms describe the decrease of the concentration C_β due to trapping, dissociation and trap mutation, respectively. Equations of type 2.9 written for every cluster type β form a system of rate equations describing the evolution of the clusters with time.

Table 2.1. Algorithm of the simulation of the point defect clustering used in MODEX.

step no.	Description	
1	Define the sample temperature T	
2	Compute $Z_{\alpha\beta}$ and $Q_{\alpha\beta}$,	Eqs. 2.6 and 2.8
3	Compute the source term $S_\alpha = I_\alpha + \sum C_\beta Q_{\alpha\beta}$,	Eq. 2.5
4	Compute the trapping term $K_\alpha = \sum C_\beta Z_{\alpha\beta}$,	Eq. 2.7
5	Solve the diffusion Eqs. 2.1-2.3 and obtain C_α	
6	Evaluate a new time step Δt for the system of rate equations 2.9 and obtain C_β (return to step 1)	

The scheme of calculations based on the equations discussed above is shown in Table 2.1. First, the temperature of the sample is defined and all temperature dependent

parameters are evaluated, e.g. diffusion coefficients, dissociation rates, etc. Then the point defect source S_α and the trapping term K_α are computed. During the next step the diffusion equations 2.1-2.3 are solved for every type of point defect α to obtain the point defect concentrations C_α . The C_α values are used in the rate equations 2.9 to obtain the defect cluster concentration C_β . Eventually, a new iteration in time propagation can be evaluated. The algorithm is valid both for ion implantation and for annealing. It should be noted that the index β in Eq. 2.9 is five dimensional : $\beta = (n, m, l, k, j)$ where n, m, k and l define the structure of the cluster and j defines the depth interval. The total number of equations in the system 2.9 is the product of five limiting values: N_V, N_{He}, N_X, N_I and N , where N_V, N_{He}, N_X and N_I are the maximum possible number of vacancies, helium atoms, impurities and self-interstitials, respectively, in the cluster structure and N is the number of slabs used to describe the depth dependence. However, most of the elements in this five dimensional matrix can be neglected because not all the possible structures are realised during the simulation. In order to avoid solving the equations for all possible structures, only structures with significant concentrations are considered. The Monte Carlo approach allows one to do that in a straightforward manner.

After introducing the slabs $x_j, j = 0, 1, \dots, N$ as shown in Figs. 1 and 2, the diffusion equation 2.1 can be rewritten as follows:

$$\frac{\partial C_{\alpha,j}}{\partial t} = D_\alpha \frac{\partial^2 C_{\alpha,j}}{\partial x^2} + S_{\alpha,j} - K_{\alpha,j} C_{\alpha,j}, \quad (2.10)$$

where, as in Eq. 2.1, $S_{\alpha,j}$ and $K_{\alpha,j}$ denote the point defect source and the trapping rate respectively. Both are assumed to be constant within the slab j . The point defect concentration $C_{\alpha,j}$ in the non-stationary case is approximated by the value taken in the node x_j while in the stationary case it is a function of depth described by Eq. A.6 (see Appendix A). The balance equation for the changes in the point defect concentration $C_{\alpha,j}$ in the slab j during the time step Δt can be written as follows:

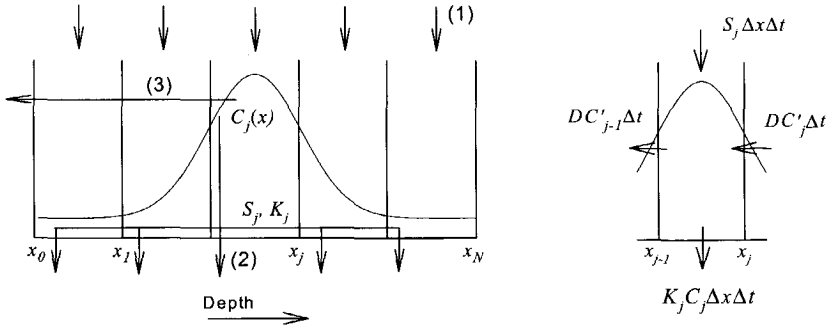


Fig. 2.1. The flow of point defects for the stationary case. $C_j(x)$ is the point defect concentration in the slab $[x_{j-1} \dots x_j]$. The point defect source S_j and the trapping rate K_j are constant within the layer j . The arrows indicate: 1) point defects generated in the sample due to implantation or dissociation, 2) point defects trapped inside the sample, 3) point defects released from the sample.

$$\Delta x_j (C_{\alpha,j}(t + \Delta t) - C_{\alpha,j}(t)) = \int_t^{t+\Delta t} D_\alpha \left(\frac{\partial C_{\alpha,j}(t')}{\partial x} - \frac{\partial C_{\alpha,j-1}(t')}{\partial x} \right) dt' +$$

$$S_{\alpha,j} \Delta t \Delta x_j - K_{\alpha,j} \Delta x_j \int_t^{t+\Delta t} C_{\alpha,j}(t') dt'. \quad (2.11)$$

The first term on the right-hand side of the equation represents the net flow of the point defects through the boundaries of the layer j due to diffusion. The second term yields the number of point defects implanted or dissociated inside the layer during the time step Δt , and the third term yields the number of point defects trapped within the layer during the same time interval. The flows of point defects for stationary and non-stationary cases are schematically demonstrated in Figs. 2.1 and 2.2, respectively. The concentration of point defects in the stationary case (see Fig. 2.1) is defined by the point defects created in the sample due to direct implantation or cluster dissociation (arrows 1), point defects trapped in the sample (arrows 2), and those released through the outer surface (arrow 3). In the diagram on the right of Fig. 2.1, the flow of point defects inside one slab is shown. In the case of non-stationary diffusion in Fig. 2.2 the point defect concentration is not

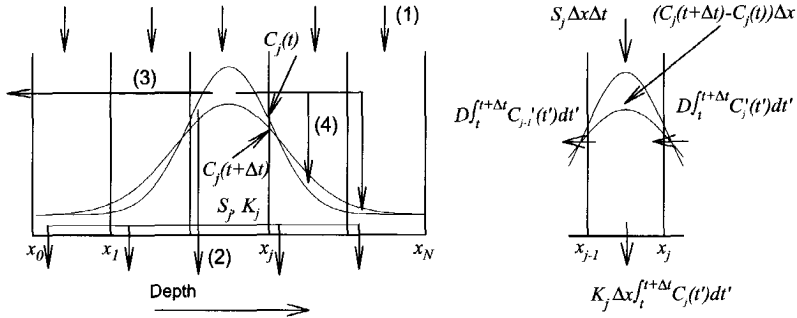


Fig. 2.2. The flow of point defects for the non-stationary case. C_j , S_j and K_j respectively are the point defect concentration, source term and trapping rate in node x_j . The arrows indicate: 1) point defects generated in the sample due to implantation or dissociation, 2) point defects trapped inside the sample, 3) point defects released from the sample, 4) point defects diffused from layer j to other layers.

constant within the time step Δt . Implanted point defects can diffuse from the layers where $C_{\alpha j}(t+\Delta t) < C_{\alpha j}(t)$ to the layers where $C_{\alpha j}(t+\Delta t) > C_{\alpha j}(t)$ (arrow 4, Fig 2.2). This redistribution of the point defects is described by the term in the left part of Eq. 2.11.

Equations of type 2.11 can be written for every layer j with the exception of the first and the last layers ($j = 0, j = N$). For these layers the boundary conditions from Eqs. 2.2 and 2.3 should be used instead of the concentration gradients in the diffusion term. The equations can be summed throughout the whole set of layers. The flows through the boundaries of the adjacent layers will compensate each other. According to the boundary condition Eq. 2.3 the particle flow through the last boundary $j = N$ vanishes. Thus we arrive at the following balance equation for the point defects of type α written for the entire sample:

$$\Sigma_{\alpha} = \Omega_{\alpha} + \sum_j \Theta_{\alpha,j}, \quad (2.12)$$

where Σ_{α} is the number of point defects implanted and dissociated during the time interval $[t, t+\Delta t]$:

$$\Sigma_{\alpha} = \sum_j S_{\alpha,j} \Delta x_j \Delta t + \sum_j \Delta x_j (C_{\alpha,j}(t) - C_{\alpha,j}(t + \Delta t)), \quad (2.13)$$

where

$$S_{\alpha,j} = I_{\alpha,j} + \sum_{\beta} C_{\beta,j} Q_{\alpha\beta}. \quad (2.14)$$

The second term in Eq. 2.13 is present only in the non-stationary case. Ω_{α} is the number of defects released through the outer surface during the same time interval:

$$\Omega_{\alpha} = D_{\alpha} \int_t^{t+\Delta t} \frac{dC_{\alpha,j=0}(t')}{dx} dt'. \quad (2.15)$$

$\Theta_{\alpha,j}$ is the number of defects of type α trapped in layer j :

$$\Theta_{\alpha,j} = K_{\alpha,j} \Delta x_j \int_t^{t+\Delta t} C_{\alpha,j}(t') dt'. \quad (2.16)$$

Evidently, the probability for a point defect to be released from the sample is:

$$P_{\alpha}^R = \frac{\Omega_{\alpha}}{\Omega_{\alpha} + \sum_j \Theta_{\alpha,j}}. \quad (2.17)$$

The probability for a point defect to be trapped in the layer j is

$$P_{\alpha,j}^{tr} = \frac{\Theta_{\alpha,j}}{\Omega_{\alpha} + \sum_j \Theta_{\alpha,j}}. \quad (2.18)$$

Released point defects are registered as a function of the implanted dose or the sample temperature. Every trapping event is considered separately. The layer where the defect is trapped is chosen according to Eq. 2.18. The next task is to define the particular cluster at which the defect is trapped. The probability for a point defect α to be trapped at a defect cluster type β is

$$P_{\alpha,\beta}^{\pi} = \frac{Z_{\alpha,\beta} C_{\beta,j}}{\sum_{\beta'} Z_{\alpha,\beta'} C_{\beta',j}}, \quad (2.19)$$

where the effective trapping rate $Z_{\alpha,\beta}$ is defined previously in Eq. 2.8 .

Usually the actual numbers for Σ_{α} , Ω_{α} and $\Theta_{\alpha,j}$ are too large to simulate the history for every defect. To save processor time a scaling factor ρ is introduced. The choice of ρ is a compromise between the desired accuracy and the computation time. Later, all the values Σ_{α} , Ω_{α} and $\Theta_{\alpha,j}$ are assumed to be scaled, i.e. divided by ρ . In the same manner the cluster concentrations $C_{\beta,j}$ in the layer j will be replaced by the number of clusters or the cluster population of type β according to: $N_{\beta,j} = (C_{\beta,j} \Delta x_j) / \rho$. Thus, for every layer j , a list of clusters $N_{\beta,j}$ is formed. Since $N_{\beta,j}$ are integer numbers the actual value of the scaling factor ρ provides the limiting concentration for the clusters to be included in the cluster list :

$$N_{\beta,j} = \frac{C_{\beta,j} \cdot \Delta x_j}{\rho} > 1 \quad (2.20)$$

The mobile point defects can also be presented in the cluster list if their concentrations $C_{\alpha,j}$ are sufficiently high.

2.2 Program algorithm and flow-chart

The flow chart of the program MODEX is shown in Fig. 2.3 and 2.4. The flow chart shown in Fig. 2.3 describes the propagation in time with the time step Δt and is the same for both simulations: ion implantation and annealing: The first step is to define the sample temperature. During ion implantation the temperature of the sample is usually kept constant. During ramp annealing the temperature is changed as follows: $T(t+\Delta t) = T(t) + \beta \Delta t$, where $T(t+\Delta t)$ and $T(t)$ are the new and the old values of the sample temperature, β is the annealing rate and Δt is the time step. If the temperature is changed, the values for the diffusion coefficients D_α , sink strengths $Z_{\alpha\beta}$ and dissociation rates $Q_{\alpha\beta}$ should be updated. During the next step the mobility of the point defects is checked. The program considers three different types of mobility: *immobile*, *slow* and *fast*. Mobility type *immobile* means that the defect is not mobile at the current temperature and solving the diffusion equations is not necessary. For the *slow* and *fast* defects the diffusion equations are solved in the non-stationary and stationary form, respectively. The criteria used to switch between the different mobility types are shown in Table 2.2. The diffusion equation in the non-stationary case is evaluated numerically with the time step δt ; $\delta t \ll \Delta t$ (see Appendix B). The transition between the non-stationary and stationary solutions takes place when the non-stationary solution is no longer stable. This occurs when the size of the spatial grid Δx and the time step δt used in the finite element scheme fail to match the following requirement [Press *et al.* 1989] : $D\delta t/(\Delta x)^2 < 1$. The transition between *immobile* and *slow* point defects takes place when the changes in the mobile

Table 2.2. The criteria used to define the mobility type of the point defects.

immobile \rightarrow slow	slow \rightarrow fast
	$D\delta t / \Delta x^2 > 1$,
$(C_{\alpha j}(t+\Delta t) - C_{\alpha j}(t))\Delta x_j / \rho > 1$ see Eq. 2.11	δt is the time step used in the numerical solution procedure of the non-stationary diffusion Eq. 2.1: $\delta t \ll \Delta t$

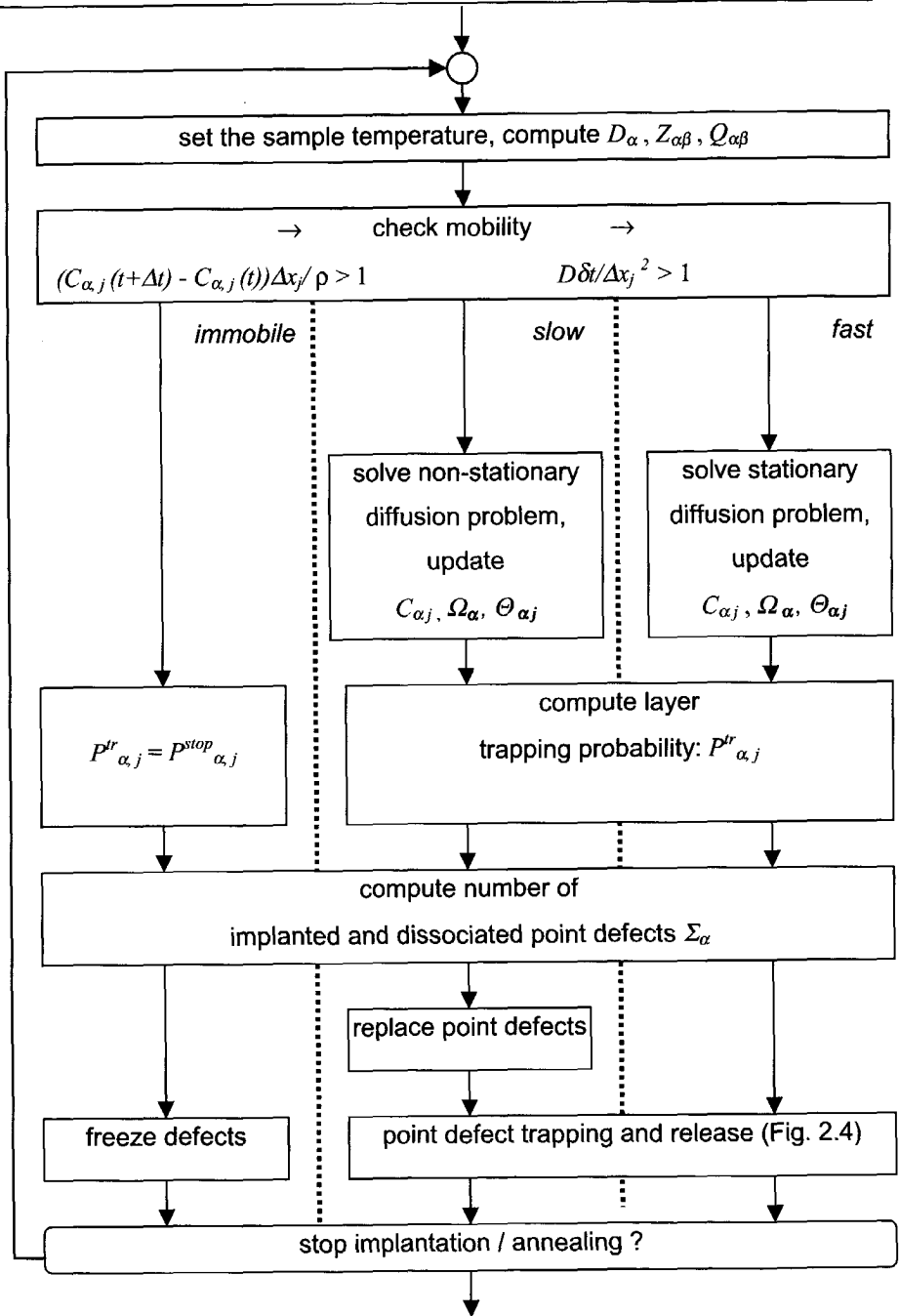


Fig. 2.3. The flow-chart of the main cycle of the program MODEX. Different routes are shown for immobile, slow and fast point defects

point defect concentrations within the time step Δt are significant enough to be accounted for in the balance equation 2.11. The point defects of different mobility type are treated separately as shown in the flowchart in Fig. 2.3. For the *immobile* point defects no transport equation is solved. The layer trapping probabilities $P_{\alpha,j}^{tr}$ are substituted by the probability that the implanted particle is stopped or a Frenkel pair is created inside the layer j : $P_{\alpha,j}^{stop}$. The latter are provided by TRIM simulations. The actual number of point defects originated in the sample during the time step Δt is estimated according to the Poisson distribution with the mean value Σ_{α} . During the next step the defects are frozen in the layer where they originated without any transport.

For the *slow* defects the boundary value problem 2.1-2.3 is solved and new concentrations $C_{\alpha,j}(t+\Delta t)$ are obtained. Next, the released and trapped fractions R_{α} and $T_{\alpha,j}$ and the layer trapping probabilities $P_{\alpha,j}^{tr}$ are computed, Eqs. 2.15 - 2.18. Then the number of implanted or dissociated defects Σ_{α} is computed, Eq. 2.13. The concentrations of *slow* defects are usually high enough to be included in the cluster list $N_{\beta,j}$ (see Eq. 2.20). During the next step the point defects are replaced from the layers where $C_{\alpha,j}(t+\Delta t) < C_{\alpha,j}(t)$ to the layers where $C_{\alpha,j}(t+\Delta t) > C_{\alpha,j}(t)$ (see Fig. 2.2). At the next step the defects are transported through the sample according to the layer trapping probability $P_{\alpha,j}^{tr}$. The transport algorithm is shown separately in Fig. 2.4 and will be discussed below.

The *fast* defects are treated in almost the same way as the *slow* ones except for the following simplifications: 1) the diffusion equation is solved in the stationary form; 2) the concentrations of the *fast* defects $C_{\alpha,j}$ are usually too low to be included in the cluster list $N_{\beta,j}$; therefore no replacement of the defects is needed.

Every step shown in the flow-chart in Fig. 2.3 is carried out four times, i.e. for every $\alpha = V, He, I$ and X . The whole cycle is repeated until the implantation dose or the maximum annealing temperature are reached.

The flow chart of the transport algorithm is shown in Fig. 2.4. First, according to the release and the layer trapping probabilities, $P_{\alpha}^R, P_{\alpha,j}^{tr}$, it is determined whether the defect is released through the outer surface or trapped in the layer j . Then according to the

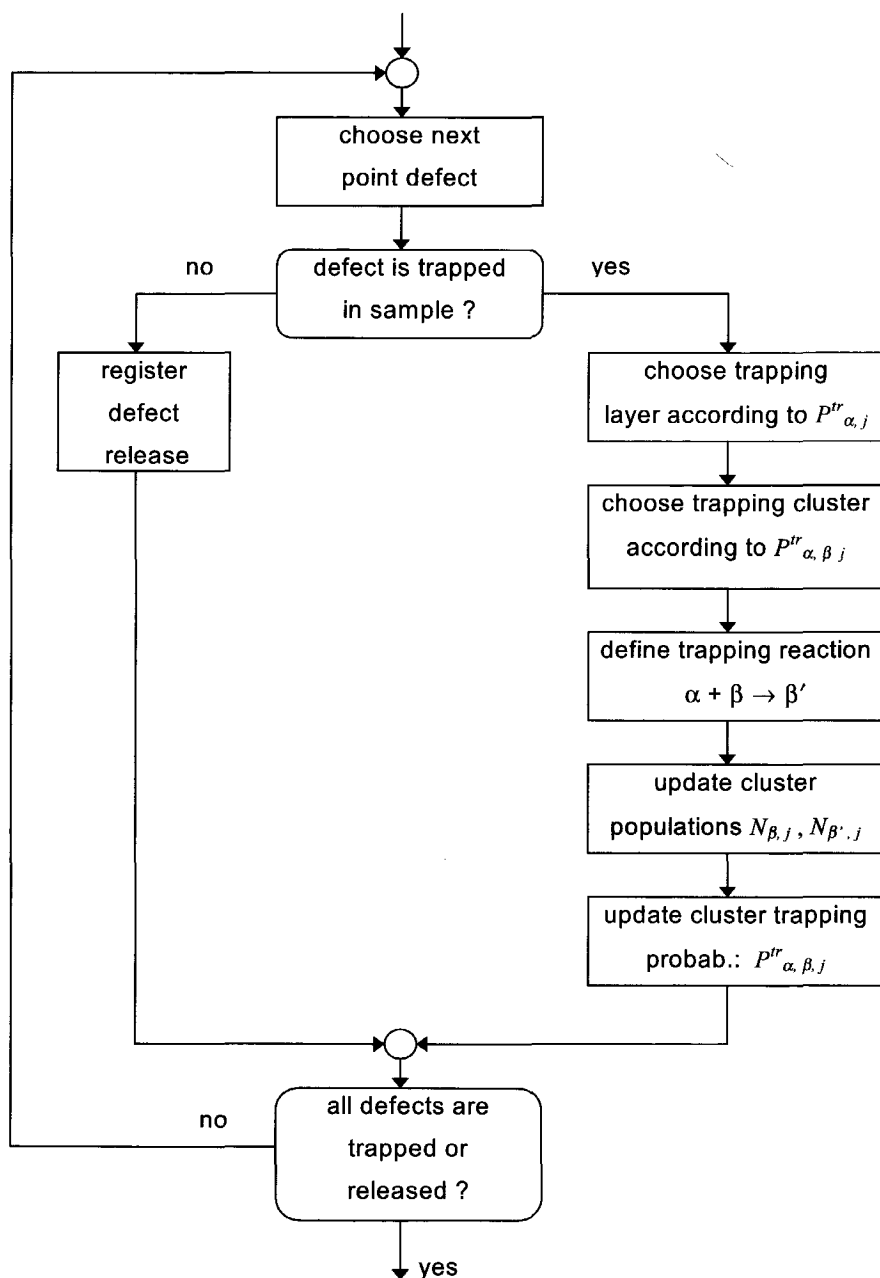


Fig. 2.4. The flow-chart of the point defect transport algorithm of the program MODEX.

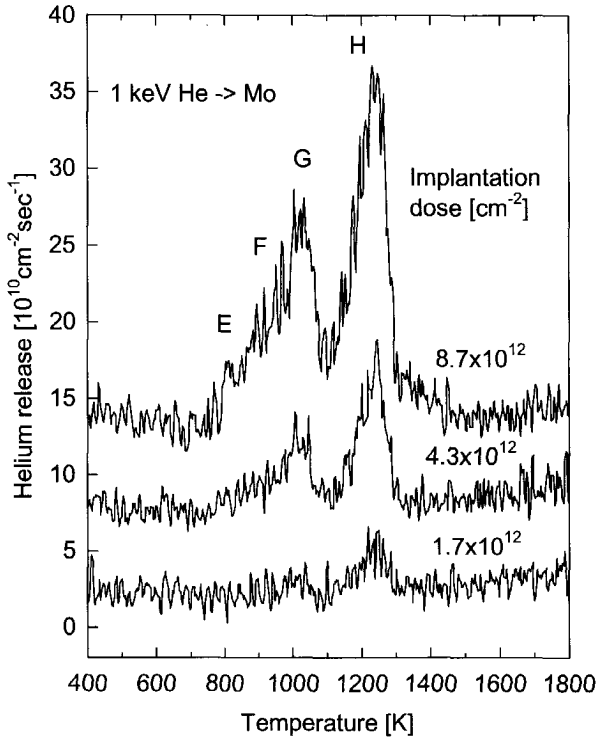


Fig. 2.5. THDS spectra for 1 keV helium implantation in Mo for various implantation doses: 1.7×10^{12} , 4.4×10^{12} and $8.7 \times 10^{12} \text{ cm}^{-2}$. Desorption peaks denoted as H, G, F and E are discussed in the text.

cluster trapping probabilities $P_{\alpha\beta,j}^r$ (see Eq. 2.19) the particular cluster with the structure β from the cluster list $N_{\beta j}$ is chosen at which the point defect of type α will be trapped. Consequently, the reaction which takes place is established and the final structure β' is defined: $\alpha + \beta \rightarrow \beta'$. For example: $\text{He} + \text{VHe}_2 \rightarrow \text{VHe}_3$. During the next step the populations of the clusters type β and β' in the cluster list of layer j are updated in the following way:

$$N_{\beta} = N_{\beta} - 1$$

$$N_{\beta'} = N_{\beta'} + 1.$$

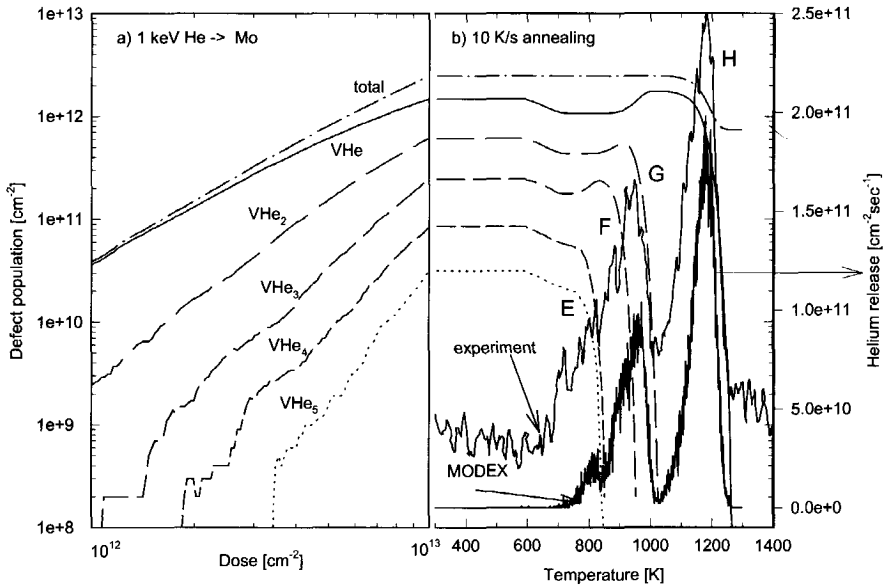


Fig. 2.6. MODEX simulation of 1 keV helium implantation in Mo: Populations of VHe, VHe₂, VHe₃, VHe₄, VHe₅ clusters are plotted versus the implantation dose and then the annealing temperature. Helium release spectrum obtained from the simulation and from the experiment are also shown. Note that the experimental spectra is shifted upwards because of the background.

If the changes in the cluster list are considerable the cluster trapping probabilities $P_{\alpha,\beta,j}^{tr}$ are updated. The loop on the flow chart in Fig. 2.4 is repeated until all point defects are trapped or released.

2.3 Examples of simulations. Helium-vacancy clustering in molybdenum

Originally, MODEX was developed to simulate Thermal Helium Desorption Spectrometry (THDS) experiments. The technique is described in detail in Chapter 3. The THDS spectra after 1 keV helium implantation in molybdenum with various doses are shown in Fig 2.5. Every peak in the spectrum is related to the dissociation of a certain

Table 2.3. Input parameters used for the simulations of He implantation and desorption in Mo.

Parameter	unit	value
implantation energy E_{He}	[keV]	1.0
Frenkel pair production rate	[ion ⁻¹]	0.6
vacancy migration energy E_v^m	[eV]	1.3
helium migration energy E_{He}^m	[eV]	0.2
self-interstitial migration energy E_I^m	[eV]	0.1
dissociation energies E^{diss} for:	[eV]	
VHe		3.18
VHe ₂		2.57
VHe ₃		2.4
VHe ₄		2.13
VHe ₅		2.13

type of defect cluster. With the increase of the implantation dose more types of clusters are created and consequently more peaks can be observed in the spectrum. In details THDS measurements in Mo are described in [Van Veen 1983]. The input parameters used in the simulation are given in Table 2.3. MODEX simulation results are presented in Fig. 2.6 where the populations of different types of clusters are plotted versus the implantation dose in the left-hand part of the figure and versus the annealing temperature in the right-hand part. Vacancies created during the implantation are not mobile at room temperature ($E_v^m = 1.3$ eV) while helium atoms and self interstitials are mobile and therefore are free to go to the outer surface or to be trapped by the vacancies. The defect clusters created during the implantation are mostly overpressurized, i.e. the number of helium atoms is larger than the number of vacancies. During the ramp annealing helium-vacancy clusters VHe₄ and VHe₅ are the first to dissociate, at 800 K: VHe₄ → He* + VHe₃ and VHe₅ → He* + VHe₄ (see peak E in Figs. 2.5 and 2.6). The asterisk in these reactions denotes mobility at the current temperature. The reactions which take place provide both helium release observed in the spectrum and the increase in the VHe₃ - cluster population. At higher temperatures (800-1000 K) VHe₃ and VHe₂ - clusters

dissociate providing contributions to peaks F and G, respectively. Despite the changes in the cluster populations the total number of clusters remains constant until 1300 K. At this temperature VHe-clusters become unstable (peak H). When VHe's dissociate, i.e. helium atoms leave the substitutional position, the total cluster population drops to the level determined by the presence of the clusters with two and more vacancies. Helium release from this type of cluster takes place at temperatures higher than 1300 K and was not simulated in this work. In the right-hand part of Fig. 2.6 the THDS spectra, obtained from simulations and experiment, are shown. A reasonable agreement between both spectra is observed.

Conclusions

1. A Monte-Carlo program MODEX is written which is capable of simulating the defect clustering process during ion implantation and annealing.
2. The Monte-Carlo approach used in the program has proved to be an efficient way for solving the rate equations.
3. The results of simulations for helium implantation in Mo demonstrated in this chapter are in fair agreement with the experimental observations.

CHAPTER 3

Experimental

Introduction

This chapter contains the description of the experimental techniques used in this study. Thermal Helium Desorption Spectrometry (THDS), extensively used in the experimental studies presented in Chapters 3, 4 and 5, is described in Section 3.1. This section presents:

- the description of the first-order desorption model,
- the computer code DEC&DAP developed for data acquisition of the THDS experiments
- the computer code DECO developed for the processing of the THDS spectra.

This chapter also presents the description of the 30 keV electrostatic implanter DANFYSIK and the computer code SMAC developed for the control of the separation magnet.

In the last part of this chapter a brief description of the Positron Beam Analysis (PBA) technique is presented.

3.1. Thermal helium desorption technique

Thermal helium desorption spectrometry with helium used as a probing atom has been shown to be a powerful tool to investigate the thermal stability of defects created by ion implantation [Van Veen 1991]. Thermal helium desorption experiments can be split into a number of steps: During the first step, a sample is subjected to ion implantation. Implantation can be carried out by gas or metal ions. For a number of materials described in this thesis the parameters characterising the profile of the stopped ions and the amount of Frenkel pairs produced by an ion are shown in Table 3.1. The values are obtained from TRIM simulations [Ziegler *et al.* 1985]. The point defects introduced in the material, i.e. implanted gas atoms, self-interstitials and vacancies, depending on their actual mobility and the amount of traps inside the material, can be trapped in the sample or can migrate back to the outer surface and be released. In the first case the implanted gas is accumulated inside the sample trapped at the pre-existing defects and at the defects created by the implantation. The second step is to anneal the created defects at a certain temperature. During the third step, low energy helium implantation is used to decorate the defects with helium atoms. Helium is chosen because of low solubility in most materials and therefore high sensitivity for open volumes. Consequently, the fourth step is to anneal the sample with a constant annealing rate β which is chosen in the range 1-10 K/s. In this thesis the ions used for creating damage are often the same kind as the probing atoms, primarily helium. Therefore the third step is not always required. Implantation with helium has an extra advantage. It is used to simulate nucleation of helium-vacancy clusters which takes place due to (n,α) reactions in reactor structural materials subjected to neutron irradiation.

3.1.1. First-order desorption model

During the ramp annealing the defects dissociate at certain temperatures depending on their dissociation energies. The dissociation of the gas from the traps in many cases can be described by the first-order dissociation model:

$$\frac{dN_{tr}}{dt} = -N_{tr} \nu \exp\left(-\frac{E^{diss}}{kT}\right), \quad (3.1)$$

where N_{tr} is the number of traps filled with gas, ν the attempt frequency, E^{diss} the dissociation energy, k the Boltzmann constant and T the absolute temperature. Diffusion from the traps to the sample surface and escape from the surface also result in gas release from the sample. If the desorption process is determined by the dissociation rate from traps, and the dissociation is the first-order process, the desorption is called first-order desorption. The first-order desorption model is valid in most cases of helium and hydrogen trapping provided the following requirements are fulfilled:

1. Diffusion for the dissociated gas atoms inside the sample is fast, i. e. $E^{migr} \ll E^{diss}$.
2. Gas atoms do not experience any surface barrier or recombination at the surface. If recombination takes place, like in the case of hydrogen the process should be fast and not rate determining.
3. Every dissociation reaction provides only one dissociated atom.
4. No interactions between the traps are taken into account, e. g. the dissociated atoms are not retrapped by more stable sinks.

For the first-order desorption mechanism the desorption rate $L(T)$ is:

$$L(T) = -\frac{dN_{tr}}{dt} = N_{tr} \nu \exp\left(-\frac{E^{diss}}{kT}\right) \quad (3.2)$$

In this case the temperature T_{max} where the release in the desorption peak attains its maximum is related to the dissociation energy E^{diss} as follows:

$$\frac{E^{diss}}{kT_{max}^2} = \frac{\nu}{\beta} \exp\left(-\frac{E^{diss}}{kT_{max}}\right), \quad (3.3)$$

where $\beta = dT/dt$ is the ramp rate. Assuming that the initial concentration of traps is $N_{tr,0}$, the desorption rate can be written explicitly:

$$L(T) = N_{tr,0} \nu \exp\left(-\frac{E^{diss}}{kT} - \frac{\nu}{\beta} \int_0^T \exp\left(-\frac{E^{diss}}{kT'}\right) dT'\right), \quad (3.4)$$

Release of multiple filled traps and other complicated cases is described by computer program MODEX presented in Chapter 2. In the case of molecular gases, e. g. hydrogen and its isotopes, the recombination process at the surface should be taken into consideration. As an example, thermal release of tritium from spherical grains is discussed in Chapter 6.

Table 3.1. Parameters characterising the profiles of depth distributions for the stopped ions. The profiles are characterised by the mean implantation depth (range) and standard deviation or straggling. The values are obtained from TRIM simulations. The number of Frenkel pairs formed per ion is given without taking into account direct recombination within the cascade.

Material	Ion	Energy (keV)	Range (nm)	Straggling (nm)	Frenkel pairs/ion
V	^4He	1.0	10	5	6.7
Mo	^4He	1.0	9	5	4.4
Be	^3He	3.0	34	11	16.6
	D	1.2	18	5	3
Si	^3He	30	264	80	56
	D	15	252	66	16
MgO	^3He	30	158	42	23
	D	15	150	34	6

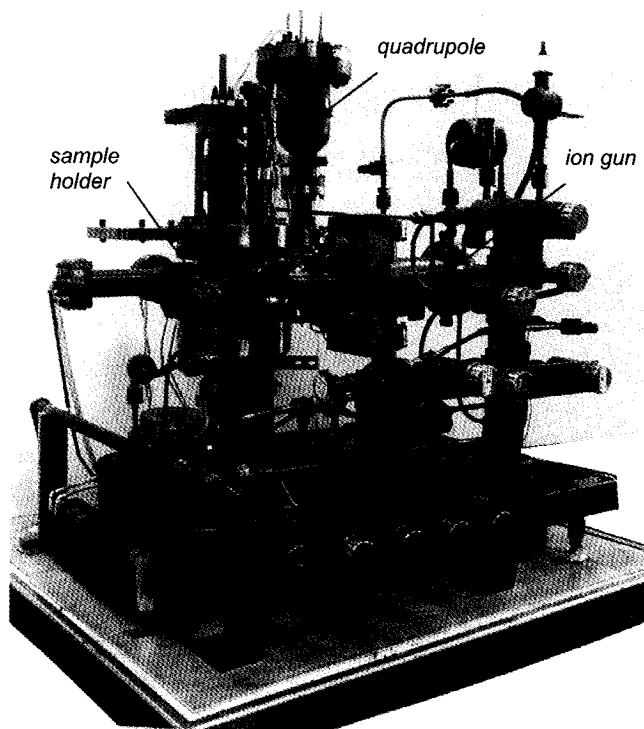


Fig. 3.1. View of the Thermal Helium Desorption Spectrometry set-up.

3.1.2. Apparatus

A typical experimental set-up of a thermal desorption experimental facility described earlier by Van Veen *et al.* [1980] is shown in Fig. 3.1. It consists of an ultra high vacuum (UHV) working chamber, an ion gun, a quadrupole, a sample holder with an electron gun for heating, and a calibration system. The ultra high vacuum in the working chamber is achieved by the sequence of a turbo-molecular pump, a diffusion pump and a backing pump in series. This combination provides the low hydrogen background

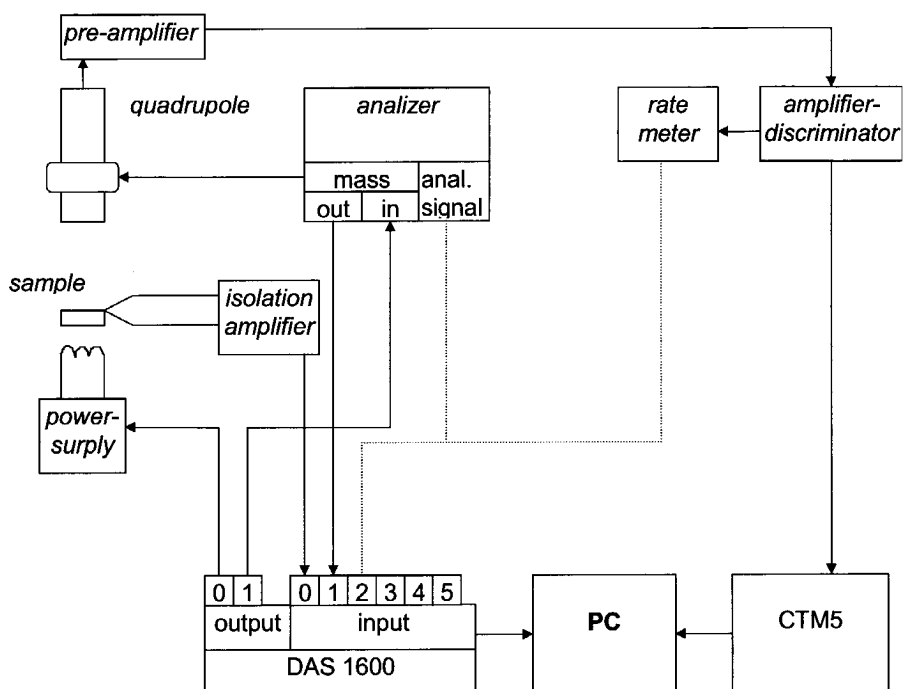


Fig. 3.2. Data acquisition set-up for Thermal Helium Desorption Spectrometry experiment.

pressure necessary for measurements of deuterium and helium release. The quadrupole used in the particular set-up shown in Fig. 3.3. is a Balzers QMG 111B analyser. The ion gun is capable of forming gas ions and implanting them in the target with a maximum energy of 3 keV. The Wien $E \times B$ filter provides mass separation so that only the desired ions are implanted. Sweep plates located directly in front of the sample ensure a uniform dose distribution over the implanted area. The electron gun used for the annealing of the sample consists of a filament and a grid. Both are put at a 1.5-2 kV negative potential relative to the sample. Typical values for the emission current of 20-30 mA provide a power of 60 W, sufficient to heat a sample with dimensions $10 \times 10 \times 0.5 \text{ mm}^3$ to 1600 K at a heating rate of 10 K/s.

The calibration system consists of a 1 l volume filled with the calibration gas of a known pressure, typically 2×10^{-5} mbar. During the calibration procedure 1 cm^3 of gas from the 1 l volume is released into the working chamber and is measured by the quadrupole. The volume of 1 cm^3 at 2×10^{-5} mbar pressure and at room temperature

contains 5.3×10^{11} molecules (or atoms for noble gases). The number of gas atoms or molecules divided by the total number of recorded pulses or counts yields the sensitivity Q . For helium typical value is $Q = 10^6 - 10^7$ He/count.

As was mentioned earlier, gas release from the sample during the annealing stage is monitored by the quadrupole. The measured signal is proportional to the partial pressure of gas in the desorption chamber $P(t)$ and through $P = \frac{N}{V} kT$ to the number of gas atoms N . Due to the finite residual time of the gas in the desorption chamber the measured signal $P(t)$ is different from the desorption rate $L(t)$. Both are related as follows:

$$L(t) = \frac{dP(t)}{dt} + \frac{S}{V} P(t) = \frac{dP(t)}{dt} + \frac{P(t)}{\tau}, \quad (3.6)$$

where τ is the averaged residence time of gas in the desorption chamber, V is the volume of the desorption chamber and S is the pumping speed. The solution of this equation is discussed in Section 3.1.4.

3.1.3. Data acquisition: Program DEC&DAP

The apparatus used for data acquisition in the THDS measurements is shown schematically in Fig. 3.2. Two Keithley PC cards are used in the data acquisition process: a CTM5 counter with internal clocks and a DAS1600 with 8 differential analogue (ADC) inputs and two analogue outputs (DAC).

The CTM5 counter is used to register the pulses coming from the *electron multiplier* after they are amplified and converted into TTL standard by the *pre-amplifier* and the *amplifier-discriminator*. The internal clocks of the CTM5 card are used for pacing the measuring time. The ADC input channels of the DAS1600 are used to collect the following data signals:

- thermocouple signal after it has been amplified by the *isolation-amplifier*;

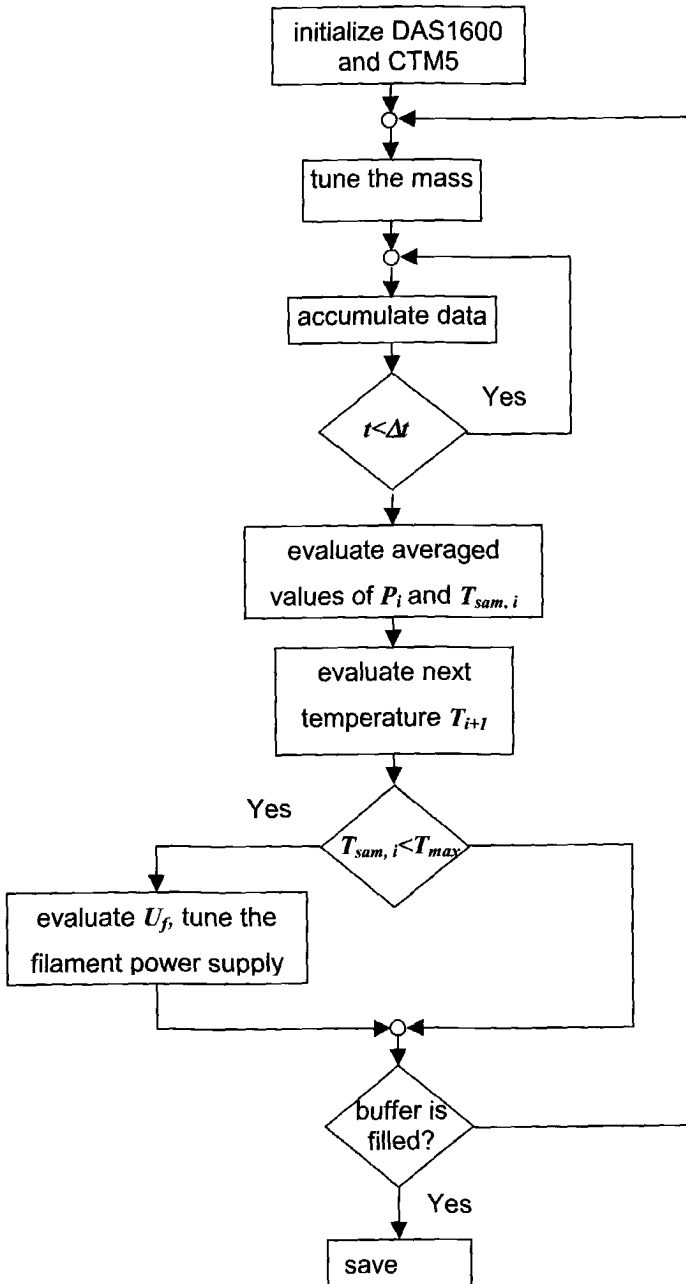


Fig. 3.3. Flow-chart of the data acquisition program DEC&DAP.

- current mass to which the *quadrupole* is tuned;
 - analogue pressure signal from the *quadrupole* or analogue signal from the *rate meter*.
- Both are optional because usually the CTM5 card already records the quadrupole signal.

Two analogue output DAC channels of the DAS1600 card are used to

- control the filament *power supply*;
- control the *quadrupole* mass tuning.

The Desorption Experiment Control and Data Acquisition Program DEC&DAP was designed to carry out the following tasks:

- acquisition of the experimental data during the desorption experiment;
- control of the filament power supply to achieve a linear annealing rate;
- measurement of the partial pressure of maximum five different masses simultaneously;
- mass scan around the desired value if necessary.

The flow chart of the program DEC&DAP is shown in Fig 3.3. After the initialisation of both cards, DAS1600 and CTM5, and starting the internal clocks of CTM5, the program begins the main loop of controlling the filament power supply and collecting the data. The main loop consists of the following steps:

1. Tuning of the quadrupole to the desired mass (switches between different masses take place after every 5-8 measured points);
2. Accumulation of data during the measuring time interval Δt which corresponds to one channel i ;
3. Calculation of the averaged values for the sample temperature $T_{sam,i}$ and the quadrupole pressure P_i corresponding to the channel i after the measuring time Δt expires;
4. The temperature value for the next time step is calculated as follows:

$$T(t_{i+1}) = T_0 + \beta(i+1) \Delta t, \quad (3.7)$$

where β is the annealing rate in K/s. If the sample temperature is higher than the maximum annealing temperature T_{max} , step 5 is skipped;

5. Voltage setting for the filament power supply U_f is calculated according to the following equation

$$U_f = U_{\text{offset}} + (dU/dt)t + U_{\text{corr}}, \quad (3.8)$$

Table 3.2. Format of data file used by DAC&DAP program. Dollar sign means hexadecimal format.

Block	size [bytes]	Position [hex]	Description
Header	64	\$0	Version
		\$4	PC
		\$A	HDS no
		\$C	Sample time [ms]
		\$E	Sample dead time [ms]
		\$10	Calibration time [ms]
		\$12	Calibration dead time [ms]
		\$14	Thermocouple
			0 – CrAl
			1 – Wre
		\$16-18	Date
		\$1A-1E	Time
		\$22	Energy [eV]
		\$24	Dose [m^{-2}]
Buffer 0	2048	\$26	Amount of calibration gas [molecules]
		\$28	Pumping speed τ [ms]
Buffer 1	2048	\$0-840	Temperature
Buffer 2	2048	\$841-1040	Quadrupole pressure
Buffer 3	2048	\$1041-1840	Calibration
		\$1841-2040	Mass

where U_{offset} is the voltage corresponding to the start of the emission of the filament. dU/dt is the constant increase of the voltage. Both depend on β and the particular set-up. U_{corr} is the feedback correction calculated at every step as follows:

$$U_{corr} = P(T(t_i) - T_{sam,i}) + I \sum_{\text{last } n \text{ points}} (T(t_i) - T_{sam,i}) + D \sum_{\text{last } n \text{ points}} \left(\beta - \frac{T_s(t_i) - T_{sam,i}}{\Delta t} \right) \quad (3.9)$$

where P , I and D are the input parameters and are determined experimentally.

The loop is repeated until the buffer of 1024 channels is filled. After the measurements are finished the data is saved in a data file according to the format shown in Table 3.2.

The program runs under DOS and the programming language is Turbo Pascal.

3.1.4. Data processing. Program DECO

The processing of the TDS experimental data is naturally split into a number of rather independent tasks, which will be discussed separately:

- filtering of scatter-points;
- time deconvolution;
- subtraction of the background;
- calibration;
- fitting.

In Fig. 3.4 it is shown how the original data is subsequently processed through filtering, deconvolution and fitting. The aim of the filtering is to eliminate scatter-points shown in Fig 3.4 without making changes to the original data. As shown, the data points are confined within a certain band. The points falling outside the band are eliminated from the spectrum. The upper and the lower boundaries of the band are calculated according to the following procedure. First, the Fourier transformation of the spectrum is performed. In the Fourier space the data is substantially filtered and the back transform is carried out. The obtained smooth curve is shifted up- and downwards to form the

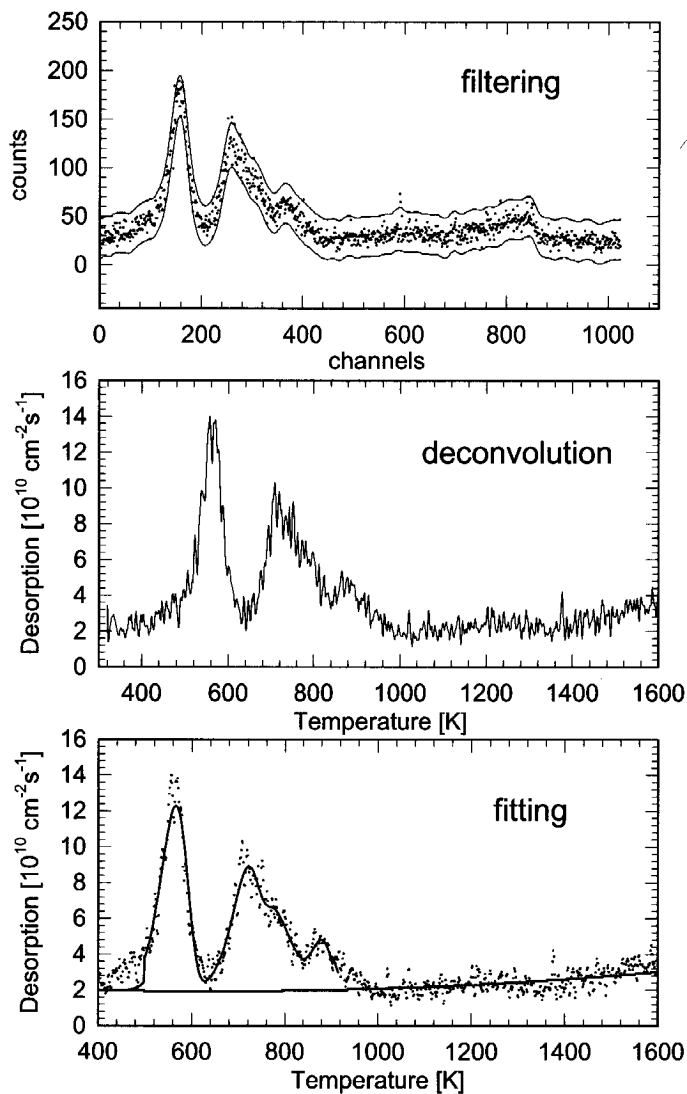


Fig. 3.4. Example of evolution of the original THDS spectrum data during filtering, deconvolution and fitting procedures carried out with the program DECO.

boundaries of the band. The width of the band can be successively reduced until all the scatter-points are eliminated.

The next step is the deconvolution. As was mentioned in the previous section the measured changes in the partial pressure dP/dt and the actual flux from the sample $L(t)$ are related according to Eq 3.6. This equation in the integral form looks as follows:

$$P(t) = \int_0^t L(t') \exp\left(-\frac{t-t'}{\tau_{res}}\right) dt' \quad (3.10)$$

where $\tau = V/S$ is the residence time. After taking the Fourier transform of both sides of the equation the desorption rate in the Fourier space L^F can be explicitly written as

$$L^F(f) = \frac{P^F(f)}{E^F(f)} \varphi(f, f_{cutoff}), \quad (3.11)$$

where the superscript F means the Fourier image, $E^F = (\exp(-(t-t')/\tau_{res}))^F$ and $\varphi(f, f_{cutoff})$ is a filter usually taken as

$$\varphi(f, f_{cutoff}) = \frac{1}{1 + \left(\frac{f}{f_{cutoff}}\right)^{2n}} \quad (3.12)$$

with $n = 1$ or 2 . The introduction of the filter φ is necessary because of mathematical incorrectness in the deconvolution procedure. Eventually, the desorption rate L is obtained as the back Fourier transform of L^F . For all the Fourier transforms the Fast Fourier Transform (FFT) algorithm is used [Press *et al.* 1989].

The spectrum fitting procedure implemented in the program DEC&DAP has the following assumptions and constraints:

- every peak n in the spectrum is related to the dissociation of one type of cluster with a characteristic dissociation energy E_n^{diss} , attempt frequency ν_n and initial concentration of clusters $N_{0, n}$;
- the dissociation takes place according to the first-order desorption model (see Eq. 3.2);

- no interactions between the clusters, e.g. retrapping of the dissociated point defects, are taken into account.

Regarding the assumptions presented above, the desorption spectrum is fitted with the following function:

$$F(T, \{\bar{N}_0, \bar{V}, \bar{E}^{diss}\}) = \sum_{n=1}^{n_{max}} f(T; N_{0,n}, v_n, E_n^{diss}). \quad (3.13)$$

Each term in the sum has the following form:

$$f(T; N_{0,n}, v_n, E_n^{diss}) = N_{0,n} v_n \exp\left(-\left(\frac{E_n^{diss}}{kT} + \frac{v_n}{\beta} \left(-\frac{kT}{E_n^{diss}} e^{-\frac{E_n^{diss}}{kT}} - \text{Ei}\left(1, -\frac{E_n^{diss}}{kT}\right)\right)\right)\right), \quad (3.14)$$

Here, for technical reasons, the integral in the solution for the first-order desorption model Eq. 3.4 is substituted by the exponential integral defined as follows:

$$\text{Ei}(n, x) = \int_1^{\infty} \frac{e^{-xt}}{t^n} dt, \quad (3.15)$$

In Eq. 3.13, n_{max} is the maximum number of the release peaks present in the spectrum (up to 10), $N_{0,n}$, v_n and E_n^{diss} , denoting the initial concentration of the clusters, the attempt frequency and the dissociation energy, respectively, are the fitting parameters related to the peak n . The total number of the fitting parameters is $3 \times n_{max}$. However, during the fitting procedure a number of parameters can be fixed at the desired values. The fitting is carried out with the Levenberg-Marquardt method, which is a combination of the steepest descent method and the Hessian method [Press *et al.* 1989].

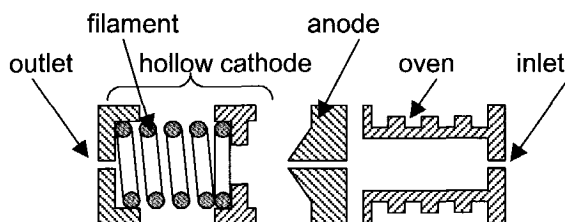


Fig. 3.5. Hollow cathode ion source of DANFYSIK.

3.2. DANFYSIK accelerator

3.2.1. Apparatus

All high-energy implantations ($E = 10\text{--}60\text{ keV}$) presented in the thesis were carried out with the 30 kV electrostatic accelerator DANFYSIK. The scheme of the “hollow cathode” ion source, which is capable to produce both gas and metal ions, is shown in Fig. 3.5. The gas is supplied through the *inlet* in order to create a pressure of ± 1 Pa sufficient to obtain ion discharge between the *anode* and the *cathode*. The electrons emitted from the filament produce the ionisation inside the source to generate plasma. The working value for the anode current is around 1 A with the anode voltage of 60–90 V. Typical values for the filament current are 20–25 A. In order to produce metal ions the metal is introduced inside the oven which is heated at 2000°C . Argon gas is used to sustain a stable anode discharge. The source is surrounded by the coils to increase the local density of electrons emitted from the filament. The ion source is kept at high voltage potential, while the target is at the ground potential.

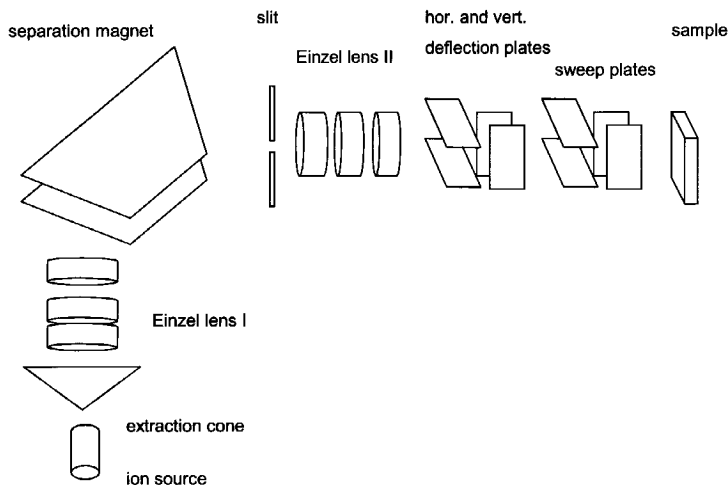


Fig. 3.6. Geometry of the ion beam transport of DANFYSIK.

The transport and mass analysis of the ions between the source and the target is shown schematically in Fig. 3.6. First, the ions are extracted from the ion source by the extraction cone which is at ground potential. Then, with the help of the Einzel lens the beam is focused before the double focus separation magnet. Inside the magnet the beam makes a turn of 90° . Since the allowed trajectory is fixed by the geometry of the magnet only the ions which match the following equation pass the magnet:

$$R = \frac{\sqrt{2}}{B} \sqrt{\frac{m}{q}} \sqrt{U}, \quad (3.15)$$

where $R = 40$ cm is the radius of the magnet, B is the magnetic field, m and q are the mass and the charge of ions, respectively, and U is the high potential of the source. Evidently, the energy of ions is $E = qU$. Typical values of the magnetic field are 625 Gauss

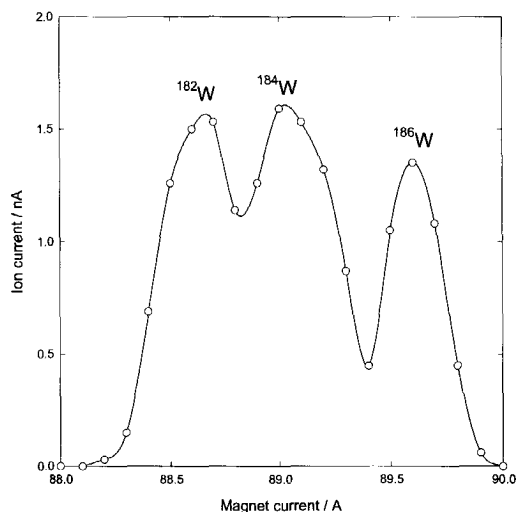


Fig. 3.7. An example of isotope separation for W performed with the separation magnet of the DANFYSIK accelerator and the program SMAC.

for 30 keV H^+ and 1250 Gauss for 30 keV $^4\text{He}^+$. Because of its special geometry the magnet focuses the beam in both vertical and horizontal directions. After the magnet the ion beam passes another focusing Einzel lens, a set of deflection plates and the sweep plates located directly before the target. The target is usually set to a positive potential of about 10 V to collect the secondary electrons. The target can be heated up to 700 K by a halogen lamp which does not have an influence on the measurements of the ion current.

3.2.2. Control of the separation magnet: Program SMAC

The program SMAC (Separation Magnet Control) was written to allow automatic control of the separation magnet. The hardware used includes the DELTA SM 15-200 D power supply and the PC card DAS1600. The output DAC channel of the DAS1600 is used to control the DELTA power supply “by current”. The DAS1600 ADC input is used to measure the ion current from the output of the nanoammeter. In order

to calculate the necessary ion current for the separation magnet the program uses the known settings for 10 keV Ar⁺ implantation. In this case the magnet field of 2270 Gauss is achieved by the magnet current of 29.4 A. Using Eq. 3.15, the magnet field for the ions X can be calculated as follows:

$$B_X = \frac{B_{Ar}}{\sqrt{400}} \sqrt{\frac{m_X}{q_X}} \sqrt{U_X} \quad (3.16)$$

where m_X , q_X and U_X are the isotope mass, ion charge and the high potential, respectively. Within 5% accuracy the magnetic field is linear with the magnet current. Using the experimentally defined value of 29.4 A necessary for 2270 Gauss, one can estimate the current necessary to obtain the desired field according to Eq. 3.16. The program has a possibility of making a scan of the magnet current around the estimated value. As an example, three isotopes of tungsten emitted by the tungsten filament from the ion source are shown in Fig. 3.7. After setting the magnet current the program starts the main loop of integrating the ion beam current measured by the ADC input of DAS1600. The accumulated dose is compared to the required dose and when the required dose is reached, the program sets the magnet current to zero which removes the ion beam from the target. The program runs under Windows 3.x and is written in Delphi 1.0.

3.3. Positron Beam Analysis

Evolution of the implantation induced defects in a number of experiments from Chapters 7 and 8 was monitored by the Positron Beam Analysis (PBA) described in detail by Van Veen *et al.* [1990]. With this technique the sample is probed by a mono-energetic beam of positrons with energies ranging from 0.1 to 25 keV which corresponds to the depths ranging from the surface up to 3000 nm. After thermalization, positrons are preferentially trapped at defects with a low electron density, e.g. vacancy related defects or cavities. Annihilation of a positron with an electron at rest results in two

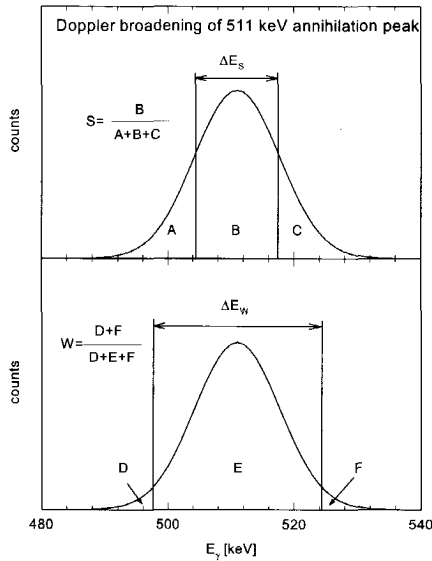


Fig. 3.8. Definition of the S - and W -parameters used in the analysis of the PBA experimental data.

photons of 511 keV each. If the electron has a non-zero momentum the energy of the photons is shifted resulting in a broader energy distribution, called Doppler broadening. The energy distribution of the 511 keV photon annihilation peak is characterised by the two parameters shown in Fig. 3.8. The S -parameter is defined by the contribution of the central part of the peak and is related to annihilations with valence or conduction electrons. The maximum value of the S -parameter is restricted by the detector resolution which for this particular set-up was $S_{res} = 0.9$. The W -parameter is defined by the “wings” contribution in the spectrum and is related to annihilations with core electrons. Analysis of the annihilation spectra is done with the help of the program VEPFIT [Van Veen *et al.* 1990]. The program makes use of the fact that the S and W -parameters are linear combinations of the S/W values related to all defects involved in the annihilation. The program describes the sample by a number of stacked slabs each characterised by its own S and W -parameter. By fitting the S and W -curves measured as a function of the positron energy the S/W values related to each slab are defined.

CHAPTER 4

Helium traps in vanadium alloys and their thermal stability

Introduction

Vanadium-based alloys are considered as potential candidates for the structural materials in fusion applications, because of their low activation under neutron irradiation and good mechanical performance at high temperatures. Recent investigations [Chung *et al.* 1996, Matsui *et al.* 1996, Smith *et al.* 1996] carried out in the framework of the ITER programme on a number of vanadium-based alloys, V-5Cr, V-5Cr-5Ti, V-4Cr-4Ti, V-3Ti-1Si, have demonstrated that the nucleation of helium-vacancy clusters to a great extent affects their radiation resistance. The conditions for the nucleation of helium-vacancy clusters are influenced by various pre-existing helium traps present in the alloy: interstitially dissolved gas impurities, such as oxygen, and nanosize VO or TiO precipitates [Chung and Smith 1992, Matsui 1996].

The Thermal Helium Desorption Spectrometry (THDS) technique described in Chapter 3 was used to investigate the sink strength and thermal stability of both pre-existing and irradiation induced helium traps. In this chapter a THDS study on pure vanadium and vanadium based alloys, primarily V-4Cr-4Ti, is presented. In Section 4.1 various types of traps present at room temperature in pure-V and alloys will be considered. Section 4.2 discusses the study of the thermal stability of helium-vacancy clusters. Section 4.3 deals in detail with the pre-existing traps present in vanadium alloys.

4.1. Helium trapping at room temperature implantation

Table 4.1. presents helium traps observed in pure V and alloys at room temperature depending on the implantation energy. At low implantation energies only the pre-existing traps can be observed. Production of Frenkel pairs at high energy implantation provides vacancies for He-V clustering. Table 4.1 suggests the strategy to isolate helium interactions with various types of traps: in the case of low energy implantation alloys contain only pre-existing traps; He-V clustering takes place in pure vanadium at high implantation energies. And finally, in the case of high energy implantation in alloys both types of traps can be studied.

Table 4.1. Helium traps present in pure vanadium and vanadium alloys depending on irradiation conditions

low energy ($E < 1$ keV)		high energy ($E > 1$ keV)
pure V		1. He - V clusters
alloy	pre-existing traps	1. He - V clusters 2. pre-existing traps

Helium-vacancy clustering

In order to eliminate the effects of the pre-existing traps, e.g. precipitates and alloying elements, helium-vacancy clustering was first studied in pure vanadium. A series of THDS spectra after various doses of 1 keV helium implantation in pure vanadium is shown in Fig. 4.1. With the increase of the implantation dose more peaks are observed in the spectra. Every new peak corresponds to a new type of cluster created by the implantation. In order to relate the desorption peaks to particular types of clusters one has first to consider the mobility of the point defects present in the material during the implantation. Literature values for the migration energies of the point defects which are present in vanadium are shown in Table 4.2. According to this data all point defects are mobile at room temperature except for oxygen. The concentration of the mobile point

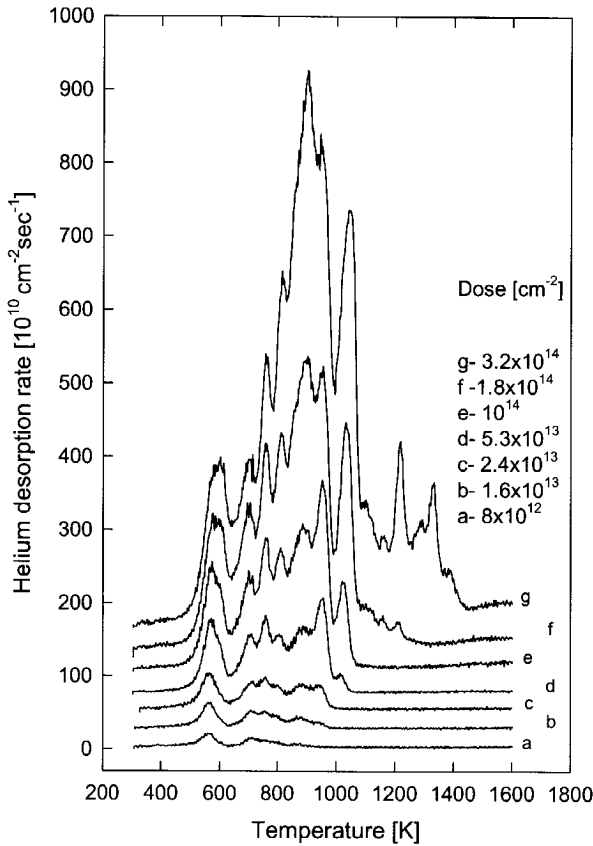


Fig. 4.1. THDS spectra measured after 1 keV He implantation in pure vanadium with the following doses: a - 8×10^{12} , b - 1.6×10^{13} , c - 2.4×10^{13} , d - 5.3×10^{13} , e - 10^{14} , f - 1.8×10^{14} and g - 3.2×10^{14} cm^{-2} .

Table 4.2. Data on the mobility of point defects in vanadium.

Point defect	Migration energy [eV]	Source
helium	< 0.1	Lewis 1988
vacancy	0.72-1.3	Adams and Foiles 1989
self-interstitial	0.6	Adams and Foiles 1989
impurity (oxygen)	1.21	Nakajima et al. 1993
	1.26	Stanley et al. 1972

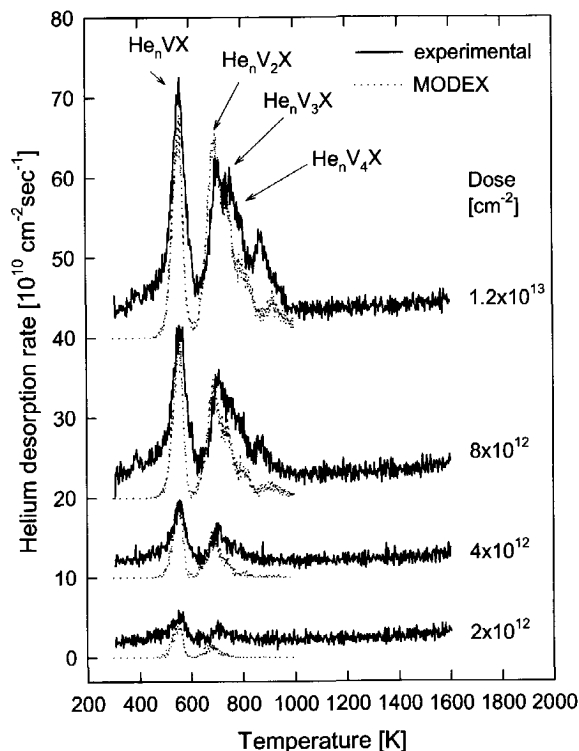
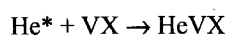
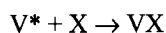
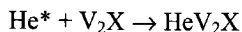
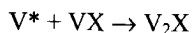


Fig. 4.2. Experimental THDS spectra (solid line) measured after 1 keV He implantation in pure vanadium are compared to the results of simulation (broken line) carried out with MODEX.

defects is very low making the probability for those defects to cluster negligible. On the other hand the concentration of oxygen in vanadium and vanadium based alloys is reported to be as high as 800-1000 appm [Chung and Smith 1992]. Therefore, it is more reasonable to assume that the nucleation process starts from trapping of the mobile vacancies at immobile interstitial impurities. Later those vacancy - impurity clusters act as trapping centres for helium and vacancies, and the nucleation process proceeds according to the following chain of reactions:



(4.1)



...,

where He denotes a helium atom, V denotes a host vacancy and $X = \text{C, N, O}$, stands for interstitially dissolved carbon, nitrogen and oxygen, respectively. An asterisk denotes mobility at room temperature. Consequently, the first peak in the release spectrum which is located at 570 K can be ascribed to the first helium containing cluster in the chain of Eq. 4.1, i.e. the HeVX - cluster. Using the relation between the peak maximum temperature in the desorption spectrum and the corresponding dissociation energy Eq. 3.3 the dissociation energy of the HeVX - cluster is estimated as $E^{\text{diss}} = 1.5$ eV. The dissociation energies for other desorption peaks are shown in Table 4.3. Keeping in mind that the vacancy formation energy in vanadium is relatively high, $E_v^f = 2.1$ eV [Adams and Foiles 1990], one can assume that adding a vacancy to a cluster should substantially change the dissociation energy, shifting the release peak to higher temperatures.

Table 4.3 Dissociation energies and other parameters used in the MODEX simulations. The dissociation temperatures T_{diss} are obtained from the experimental THDS spectra .

Defect complex	E^{diss} [eV]	T_{diss} [K]
He_nVX	1.5	570
$\text{He}_n\text{V}_2\text{X}$	1.88	710
$\text{He}_n\text{V}_3\text{X}$	2.0	755
$\text{He}_n\text{V}_4\text{X}$	2.1	790
$\text{He}_n\text{V}_5\text{X}$	2.31	870
$\text{He}_n\text{V}_6\text{X}$	2.48	930
$\text{He}_n\text{V}_{>6}\text{X}$	stable	
VX	1.17	450
$\text{V}_{>1}\text{X}$	2.15	800
He_nX	unstable	< RT
He_n	unstable	< RT

Therefore, every new peak in the spectrum can be ascribed to helium-vacancy clusters with subsequently increasing number of vacancies. Hence, the relation between the desorption peaks and $\text{He}_n\text{V}_m\text{X}$ clusters is established according to the following rules:

1. Every peak is related to helium dissociation from clusters with the same number of vacancies and different number of helium atoms, $\text{He}_n\text{V}_m\text{X}$ – clusters with $n > 0$ and m fixed.
2. The number of He atoms in the cluster is restricted by $n < \gamma m$ with $\gamma = 4-5$. If $n > \gamma m$ the cluster experiences a trap mutation, i.e. punching out an interstitial atom: $\text{He}_n\text{V}_m\text{X} \rightarrow \text{He}_n\text{V}_{m+1}\text{X} + \text{I}^*$.

The relation between the dissociation energies and the cluster structure found in vanadium is shown in Table. 4.3. This model of helium-vacancy clustering at interstitial impurities was successfully simulated by MODEX described in Chapter 2. The results are compared to the experimental THDS spectra in Fig. 4.2.

Trapping at pre-existing traps

In order to separate helium trapping at pre-existing traps from trapping at $\text{He}_n\text{V}_m\text{X}$ -clusters, low energy helium implantations were used. THDS spectra after 100 eV helium implantation with various doses in pure V and V-4Cr-4Ti are presented in Fig. 4.3. At this energy no irradiation vacancies are produced and therefore, helium can be trapped only at the pre-existing sinks, e.g. alloying elements or precipitates. Obviously, much more trapping is observed in the alloy than in pure vanadium. The desorption spectra do not contain well separated sharp peaks as in the case of 1 keV implantation in pure vanadium (see Fig. 4.1). Helium release is ascribed to helium trapped at the precipitate-matrix interfaces or other structural imperfections. The dissociation energy is defined by the particular environment and is unique for every defect. Being mainly overpressurized, these defects have low dissociation energies, ranging from 1.3 to 2 eV providing a broad halo in the helium release spectrum at 400 K - 800 K (see Fig. 4.3). Another helium release region in the spectra is located at 1300-1400 K. This release is observed only in the alloys and not in pure vanadium and is related to small helium filled

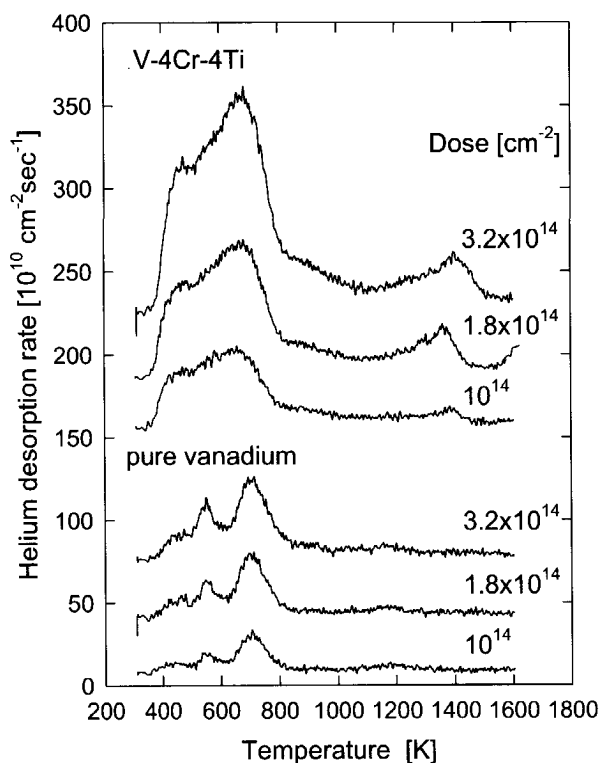


Fig. 4.3 THDS spectra measured in pure vanadium and V-4Cr-4Ti after 100 eV He ion implantation with indicated doses

bubbles formed at the precipitates interfaces. Contrary to the overpressurised helium-vacancy clusters the bubbles are relaxed according to the following considerations. Around 1200 K the outer surface of the sample acts as a source of thermal vacancies which are trapped by the overpressurized defects. Using the self-diffusion energy for vanadium of $Q = 3.2$ eV [Adams and Foiles 1990] it can be calculated that this process should take place around $T \sim 1200$ K. All the overpressurized clusters which survive at this temperature relax to helium bubbles by accumulation of the necessary number of vacancies to equalise the gas pressure and the surface tension: $P = 2\gamma/R$, where γ is the surface tension coefficient and R is the defect radius. Helium release from the bubbles at high temperatures can proceed by shrinkage [Van Veen 1991]. On the scale of activation

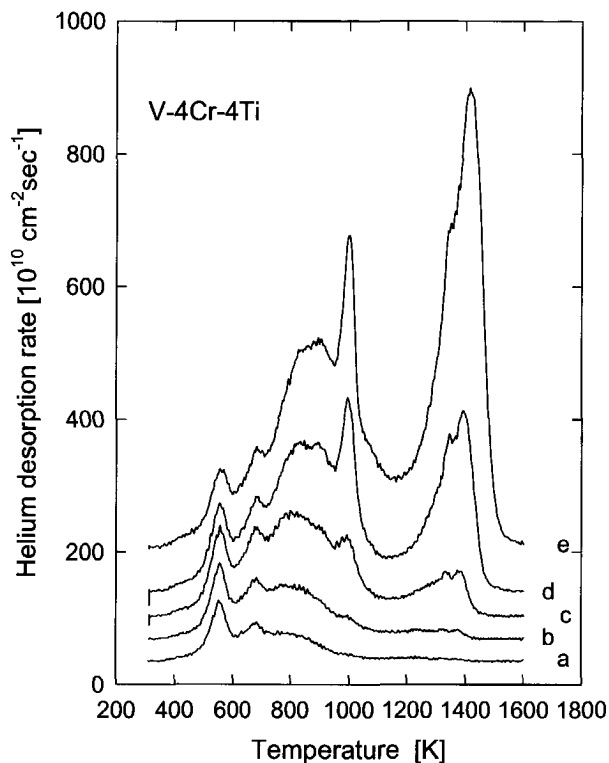


Fig. 4.4. THDS spectra measured in V-4Cr-4Ti after 1 keV He implantation with doses a) 3.2×10^{13} , b) 5.3×10^{13} , c) 10^{14} , d) 1.8×10^{14} , e) $3.2 \times 10^{14} \text{ cm}^{-2}$.

energies it coincides with the high temperature self - diffusion mechanism discussed by Adams and Foiles [1990] with the activation energy of 4.12-4.81 eV.

Helium trapping in vanadium-based alloys

At 1 keV helium irradiation in vanadium alloys one would expect both types of helium trapping processes to take place. In Fig. 4.4 THDS spectra for 1 keV helium irradiation in V-4Cr-4Ti are presented. In the temperature range $T = 500\text{-}1200$ K helium is released both from the $\text{He}_n\text{V}_m\text{X}$ clusters and the pre-existing traps, while in the range of $T = 1300\text{-}1400$ K helium is released from the bubbles. The contribution of these two types of release appear to vary in magnitude depending on the material. A comparative analysis of

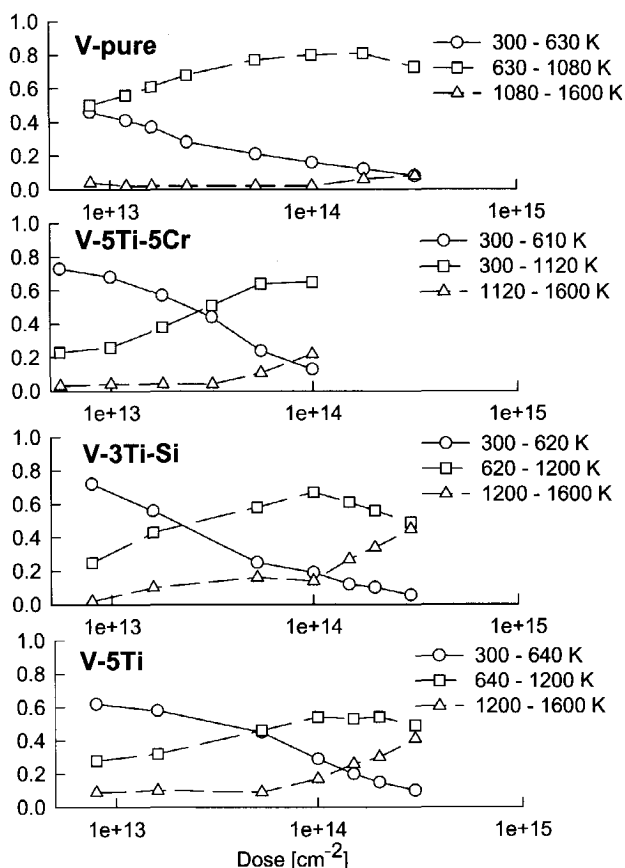


Fig. 4.5. Contributions from different temperature regions in THDS spectra for pure-V, V-5Ti-5Cr, V-3Ti-Si and V-5Ti

helium release in different temperature regions in pure vanadium and the alloys is presented in Fig. 4.5. It appears that the release from bubbles is present for the alloys but not for pure vanadium. For the alloys this release is most pronounced for V-5Ti-5Cr which might be caused by the presence of ultra-fine size TiO precipitates. Such precipitates have been observed in alloys of a similar composition [Chung and Smith 1992]. The bubble contribution starts to increase at the dose of about 5×10^{13} He/cm² in the case of V-5Ti-5Cr and at 10^{14} He/cm² for the other alloys. In all samples the contribution to the low temperature release peak decreases with the dose while the contribution to the intermediate temperature increases. From the above observations it

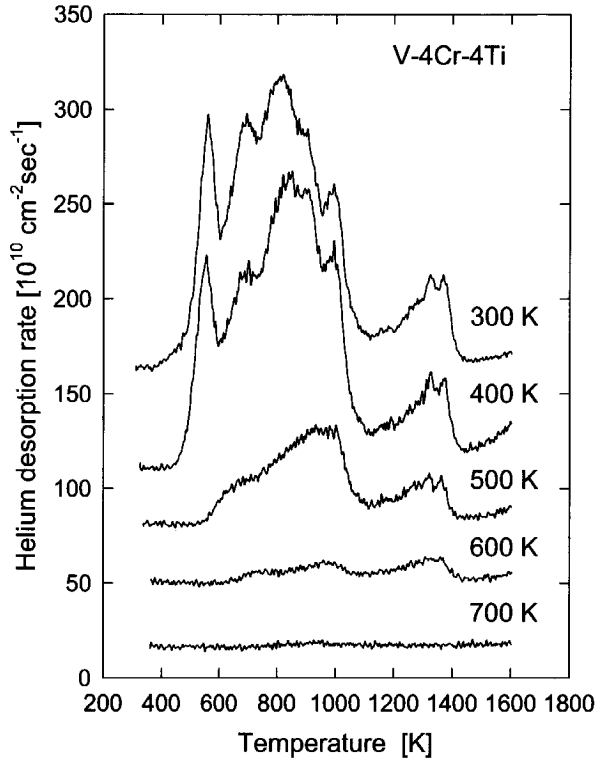


Fig. 4.6. THDS spectra measured in V-4Cr-4Ti after 1 keV He implantation with a dose of 10^{14} cm^{-2} at various temperatures.

can be concluded that the alloys, in particular V-5Ti-5Cr, provide nucleation centres for the accumulation of helium and growth of helium bubbles.

4.2 Thermal stability of helium traps in vanadium alloys

By performing Dynamical Helium Charging Experiments Chung *et al.* [1996] have demonstrated that neutron irradiation up to 31 dpa at 500-600° C in the presence of helium does not result in the formation of helium bubbles. This and similar experimental

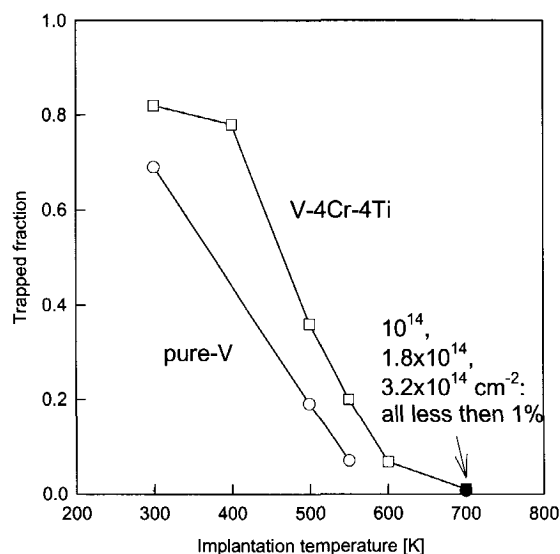


Fig. 4.7. Helium trapped fraction after 1 keV implantation at elevated temperatures in pure-V and V-4Cr-4Ti. Open symbols correspond to the implantation dose of 10^{14} cm^{-2} . In the case of V-4Cr-4Ti, at the implantation temperature of 700 K the trapped fraction for doses up to $3.2 \times 10^{14} \text{ cm}^{-2}$ was less than 1%.

observations have motivated the investigation of helium-vacancy cluster nucleation at elevated temperatures.

It was already shown in section 4.1 that the bigger $\text{He}_n\text{V}_m\text{X}_k$ - clusters appear to be more stable. However, the cluster build-up process can proceed only under the condition that the VX and HeVX - nucleation centres are already created. Keeping in mind that these centres are not stable at 550 K, one can assume that the cluster formation process at elevated temperatures should be suppressed. The THDS spectra obtained after 1 keV helium implantation with a dose of 10^{14} cm^{-2} at various temperatures are shown in Fig. 4.6. Note that already during the implantation at 700 K no defect clusters are created including those that are stable at higher temperatures.

Figure 4.7 shows the fraction of helium trapped in the sample, i. e. the amount of helium trapped in the sample divided by the implantation dose, obtained after the implantation at various temperatures in V-4Cr-4Ti and in pure vanadium. Evidently, in

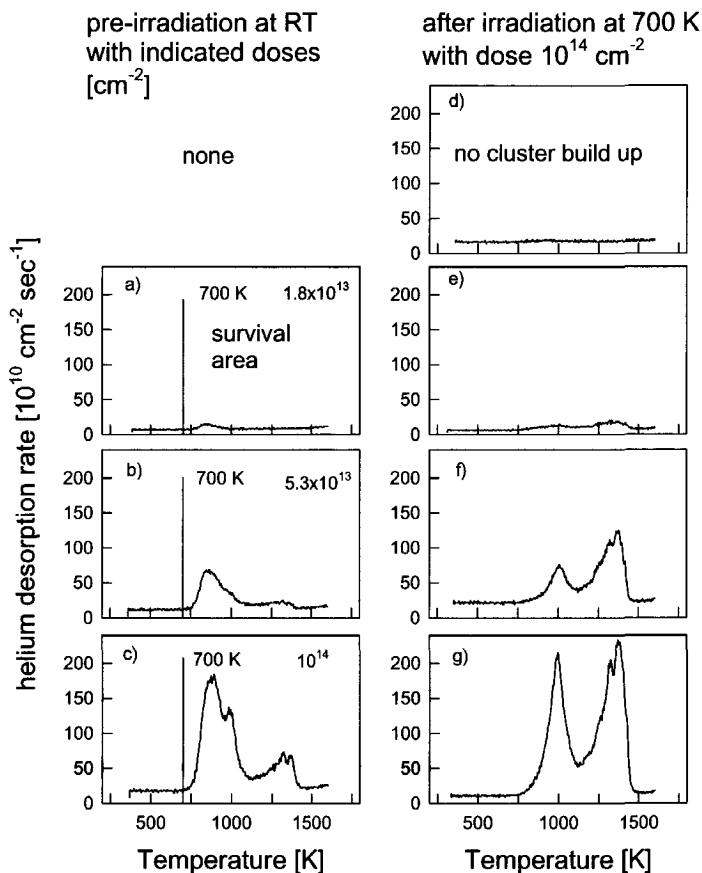


Fig. 4.8. THDS spectra measured after 1 keV , 10^{14} cm^{-2} implantation at 700 K preceded by room temperature implantation with annealing at 700 K. Spectra a, b and c are obtained after room temperature pre-implantation and 700 K annealing. Spectra d, e, f and g are obtained after subsequent implantation at 700 K.

the case of pure vanadium the suppression of the helium-vacancy clustering is more pronounced.

In another set of experiments, the 700 K implantation was preceded by room temperature pre-implantation to various doses. The implantation energy in both cases was 1 keV and the dose was 10^{14} cm^{-2} . The results are shown in Fig. 4.8. The spectra a), b) and c) show helium release in the THDS experiment performed after the room temperature implantation followed by ramp annealing to 700 K. Therefore, the observed

helium release in the spectra a), b) and c) (indicated as the *survival area*) is ascribed to the clusters which are stable above 700 K. The spectrum d) is obtained after the implantation at 700 K without the room temperature pre-implantation. No cluster build-up is observed in this case. The spectra e), f) and g) show helium release when the 700 K implantation was preceded by the room temperature pre-implantation to the doses of 1.8×10^{13} , 5.3×10^{13} and 10^{14} cm^{-2} , respectively. Since no new nucleation centres can be created during the 700 K implantation the only traps for the implanted helium must be the clusters from the *survival area*, shown in Fig. 4.8 a), b) and c).

This observation demonstrates that during a short accidental drop of temperature below 700 K, nucleation centres can be created capable of providing further clustering at high temperature implantation.

4.3 Helium trapping at precipitates

Recent studies on vanadium based alloys have shown their excellent behaviour under irradiation [Matsui *et al.* 1996]. It was reported by Matsui [1996 Vanadium Workshop] that the final thermal treatment had a considerable effect on the ductility. It was also shown that V-4Cr-4Ti and V-4Cr-4Ti-0.1Si have DBTT (Ductile Brittle Temperature Transition) around 290 K if annealed at 1373 K, while they demonstrated remarkable ductility at 77 K after annealing at 1223 K. Chung *et al.* [1996 Van. Workshop] have also reported that among the V-(4-5)Cr-(4-5)Ti alloys annealed for 1 hour at 1223, 1273, 1323 and 1373 K, the ones annealed at 1273 K showed the optimal impact properties. This observation was valid even for V-5Cr-5Ti which earlier has been reported as having poor mechanical properties. Annealing at temperatures lower than 1273 K, e.g. 1023 K, was also shown to worsen the material properties [King *et al.* 1996].

The present thermal desorption study is aimed at investigating the effect of thermal treatment on helium trapping in the V-4Cr-4Ti alloy.

As was shown in the previous section, helium release from the bubbles formed at the interfaces of the fine-size precipitates takes place in the temperature range of $T =$

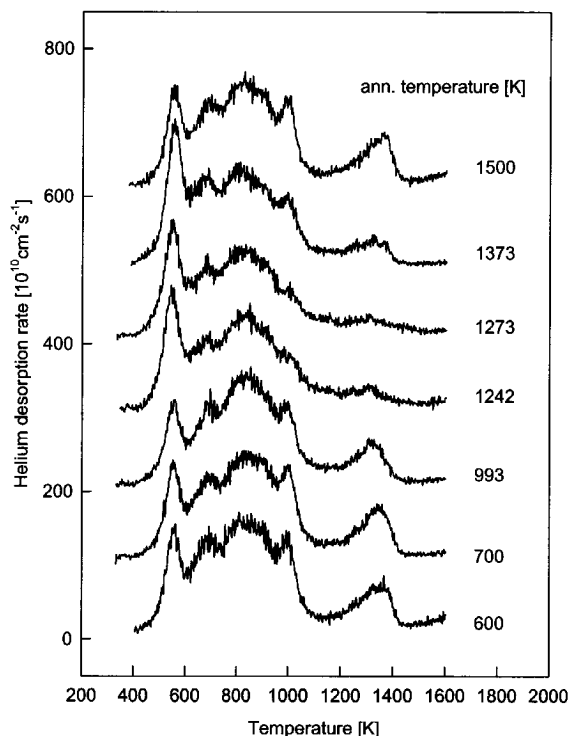


Fig. 4.9. THDS spectra measured in V-4Cr-4Ti after 1 keV, 10^{14} cm^{-2} helium implantation preceded by 1 h annealing at the indicated temperature.

1200 – 1400 K. From the TDS study it was discovered that this contribution depends on the thermal treatment of the sample before the measurements.

This effect is demonstrated in Fig. 4.9 where the desorption spectra for 1 keV 10^{14} cm^{-2} helium implantation in V-4Cr-4Ti are presented. Before every implantation the sample was pre-annealed for 1 hour at the indicated temperature. The pre-anneals at 1242 and 1273 K dramatically suppress helium release at 1300 K. The anneals at temperatures higher than 1300 K and lower than 1200 K seem to restore the 1300 K peak contributions. The contributions from a number of different temperature regions are plotted in Fig. 4.10 versus the pre-annealing temperature. It is clearly observed that the decrease of the 1300 K peak contribution is accompanied by an increase of the 550 K peak related to He-V-X clusters.

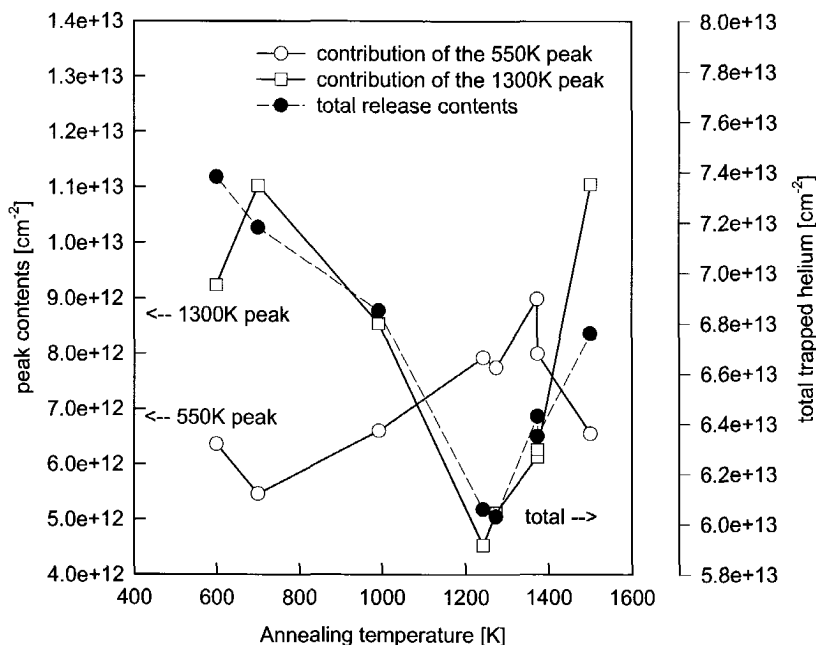


Fig. 4.10. Contributions of the 550 K and 1300 K peaks to the helium release spectra as a function of the pre-annealing temperature.

The following experiment was done to find out whether the restoration of the 1300 K peak at low pre-annealing temperatures was due to the pre-annealing or to the fact that during the previous helium desorption measurement the sample was shortly annealed up to 1600 K. The experiment was carried out in the following steps:

- 1) The sample was annealed for 1 hour at 1252 K to suppress the pre-existing traps responsible for the 1300 K release peak.

- 2) The sample was implanted with 1 keV helium but the subsequent ramp annealing during the measurements was performed only up till 1370 K. As expected, the 1300 K peak was suppressed. The corresponding spectrum is shown in Fig. 4.11, spectrum A.

- 3) The sample was re-implanted with 1 keV helium with the same dose but this time the ramp annealing was performed in the usual way up to 1600 K. The 1300 K peak in the resulting spectrum B is still suppressed. Note that this time the temperature of 1600 K was reached during the measurement.

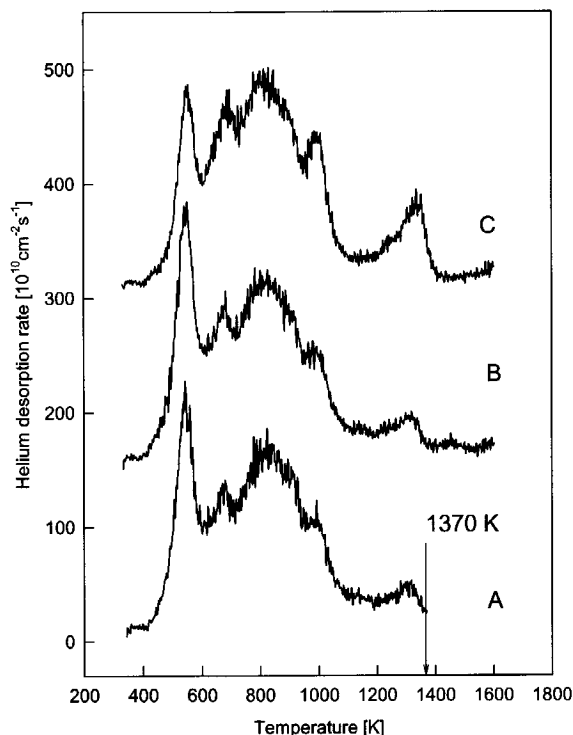


Fig. 4.11. THDS spectra measured in V-4Cr-5Ti after the treatments discussed in the text

4) The 1 keV helium implantation was repeated and the ramp annealing has demonstrated the presence of the 1300 K peak (see Fig. 4.11, spectrum C).

Evidently, the reason for the restoration of the 1300 K peak in the spectrum C was the short annealing of the sample above 1400 K during the previous measurement of the spectrum B.

Figure 4.12 summarises the effects of the thermal treatment and the implantation temperature on the desorption spectra. The relation between the sample treatment and the corresponding spectrum is presented in Table 4.4. The traps that are responsible for helium release are also shown. Note that in Table 4.4 two types of pre-existing traps (PT) are considered: PT-1 are the traps affected by the 1200-1300 K thermal treatment and PT-2 are not. All four spectra A, B, C and D in Fig. 4.12 are measured after the same 1 keV 10^{14} cm^{-2} helium implantation. Implantations A and B were carried out at room temperature and implantations C and D were performed at 500K

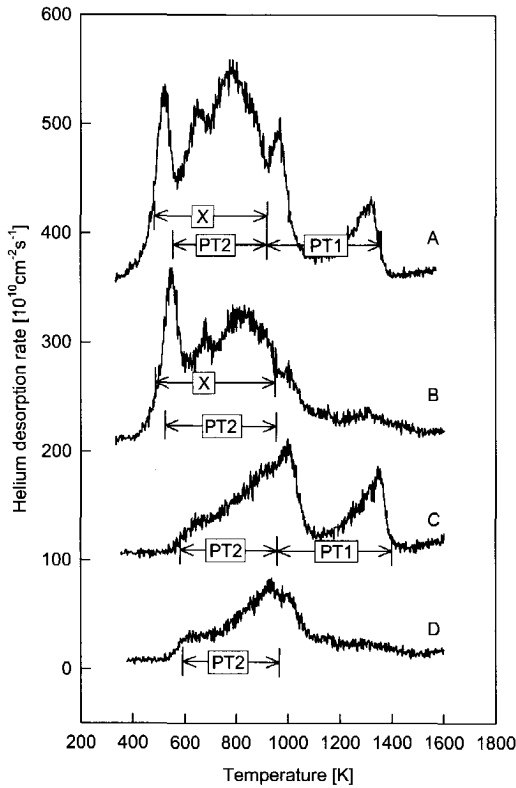


Fig. 4.12. Contributions in helium release from different helium traps present in V-4Cr-4Ti alloy: $\text{He}_n\text{V}_m\text{X}$ clusters nucleated at X – impurities, pre-existing traps PT1 and PT2. Sample treatments corresponding to spectra A, B, C and D are shown in Table 4.4.

Table 4.4. Sample treatment before the THDS measurements presented in Fig. 4.12. Helium traps responsible for the release in the spectra are also given.

Spectrum no.	pre-annealing temp [K], time [s]	Implantation temperature [K]	helium traps
A	> 1400, 10	300	X = C, N, O, PT-1, PT-2
B	1273, 3600	300	X = C, N, O, PT-2
C	> 1400, 10 s	500	PT-1, PT-2
D	1273, 3600	500	PT-2

In the latter case no He-V-X clusters formation can occur since the VX and HeVX - nucleation centres are not stable. Measurements B and D were performed after the 1273K pre-annealing for 1 hour. During this pre-annealing the pre-existing traps PT-1 which are responsible for helium release at 1300 K disappear. Before the measurements A and C no special pre-annealing was done, but the final thermal treatment in this case was the previous THDS measurement during which the sample was ramp annealed above 1400 K for about 25 s.

The probable candidates for the pre-existing traps PT-1 and PT-2 can be the fine-size Ti(O, N, C) precipitates reported by Chung and Smith [1992] or any of the alloying elements: Cr or Ti.

Conclusions

1. The THDS studies on pure vanadium and vanadium based alloys: V-4Cr-4Ti, V-5Cr-5Ti, V-5Ti and V-3Ti-1Si, have revealed two types of traps for helium:
 - $\text{He}_n\text{V}_m\text{X}$ clusters which are formed at high energy He ion implantation, $E > 1$ keV, both in pure V and in the alloys;
 - pre-existing traps observed only in the alloys.
1. Nucleation centres for He-V-X clusters in V-4Cr-4Ti and pure vanadium are shown to be unstable above 700 K.
2. Suppression of the cluster build-up at elevated temperatures ($T = 700$ K) was not observed if the nucleation centres stable above 700 K were created by room temperature pre-implantation. This observation is important with regard to the temperature control during neutron irradiation experiments carried out at nuclear reactors.
3. It was shown that 1 hour annealing at 1200-1300 K suppresses helium trapping at the pre-existing traps associated with precipitates in V-4Cr-4Ti alloy and responsible for the 1300 K release peak in the THDS spectra. However, short annealing at 1400 K restores this pre-existing traps.

CHAPTER 5

Deuterium trapping in beryllium and beryllium pre-implanted with helium

Introduction

In the present concept of the ITER program Be is considered as a prime candidate for the plasma facing material [Matera *et al.* 1996, Gelles *et al.* 1994]. Therefore, during the last years a considerable number of studies have been devoted to deuterium retention in beryllium. Deuterium detrapping from deuterium-vacancy clusters is typically observed in the temperature region 600-800 K which corresponds to an activation energy of 1.8-2.3 eV [Wampler 1992, Markin 1996]. With an increase of the implantation dose the release temperature shifts up to 1000 K and is ascribed to deuterium release from small bubbles filled with D₂. Deuterium release from helium bubbles studied by Wampler [1992] takes place at a temperature of 843 K. Further increase of the implantation dose ($>10^{17}$) according to Markin *et al.* [1996] results in two sharp release peaks located at 470 and 490 K. A TEM study on beryllium samples implanted with deuterium up to the saturation dose of about 0.3 D/Be indicated blisters or bubbles interconnected with channels [Markin *et al.* 1996]. In a different study, where beryllium was exposed to a hydrogen ion beam, Lossev and Koppers [1992] have shown that, unlike molecular hydrogen, H atoms get absorbed at the beryllium surface. The activation energies for desorption were reported to be 0.6 eV for oxygen covered and 0.87 eV for clean beryllium surfaces. According to the latter observation deuterium release from blisters, presumably opened during the implantation, is governed by desorption from the surface. Therefore, the

activation energy of about 1 eV is related to this desorption peak and is close to the values reported by Lossev and Kuppers. However, it is much lower than the values characteristic for deuterium detrapping from vacancy clusters and bubbles in the bulk. Helium introduced by nuclear reactions can also effect deuterium trapping [Chernikov 1998].

The present thermal desorption study is aimed at investigating detrapping of deuterium from implanted beryllium and from beryllium pre-implanted with helium.

5.1. Deuterium trapping in Be

Thermal desorption experiments were performed on a single crystal beryllium in a UHV-chamber equipped with an ion gun and a calibrated quadrupole mass-spectrometer discussed in Chapter 3. The implantation energies used for deuterium were 0.7 and 1.2 keV. The implantation doses varied from 10^{15} to 7×10^{17} cm⁻². The implantation energy for ³He and ⁴He ions was 3.0 keV. During the annealing deuterium release was simultaneously monitored for two masses: HD and D₂.

The desorption spectra for HD and D₂ after 2.5 keV D₂⁺ implantation in Be for the doses 10^{15} , 3.2×10^{15} , 5.6×10^{15} and 10^{16} cm⁻² are shown in Fig. 5.1. The broad desorption peak in the temperature region 600-900 K is ascribed to the deuterium release from small vacancy clusters created by the implantation. The small peak in the beginning of the spectra at 450 K is observed both for HD and D₂ and is ascribed to desorption from the surface. The activation energy of 1.1 eV which corresponds to this release is close to the values reported by Lossev and Kuppers [1992] for hydrogen desorption from beryllium covered with oxygen and clean beryllium of 0.6 and 0.78 eV, respectively. A number of sharp peaks at 1000-1100 K can be ascribed to deuterium release from D₂ filled bubbles or from helium bubbles not fully released from the previous experiments.

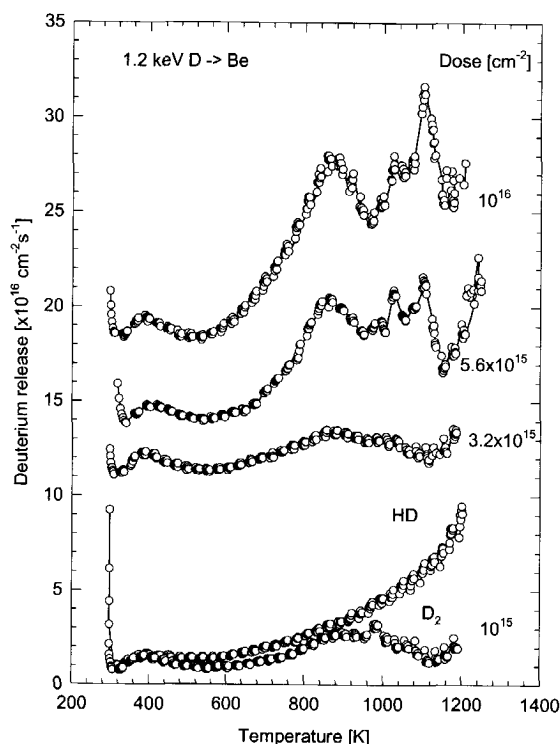


Fig. 5.1. Deuterium desorption spectra in Be after 1.2 keV deuterium implantation with doses 10^{15} , 3.2×10^{15} , 5.6×10^{15} and 10^{16} cm^{-2} .

Thermal desorption spectra for deuterium ions implanted with 0.7 keV in Be with high doses are shown in Fig. 5.2. A sharp peak at 430 K is observed only for the implantation doses higher than 10^{17} cm^{-2} . The activation energy for this release of 1.1 eV is in reasonable agreement with the values reported earlier [Wampler 1992, Markin *et al.* 1996]. In these works the release is ascribed to detrapping from the blisters or bubbles interconnected with channels, which were observed by TEM. Note that the activation energy attributed to this release is close to the value observed for the surface detrapping for low dose deuterium implantation.

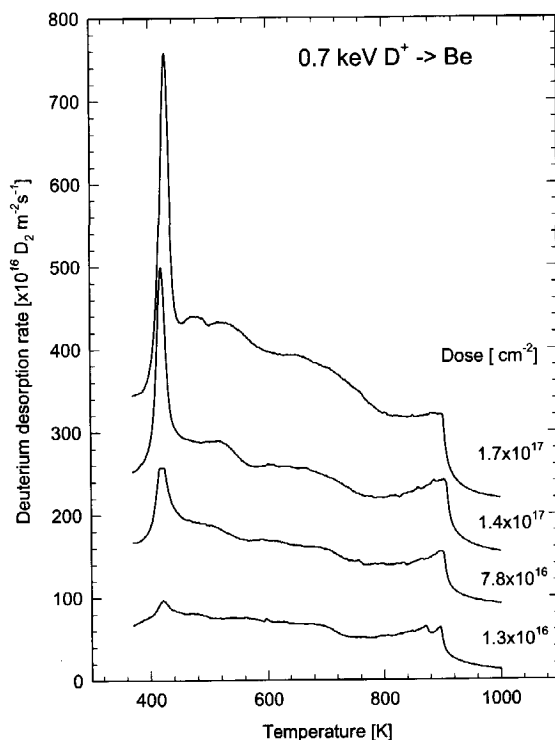


Fig. 5.2. Deuterium desorption spectra in Be after 0.7 keV deuterium implantation with doses of 1.3×10^{16} , 7.8×10^{16} , 1.4×10^{17} and $1.7 \times 10^{17} \text{ cm}^{-2}$.

5.2. Deuterium in Be pre-implanted with helium

Helium desorption spectra following implants into Be with an energy of 3.0 keV and doses between 10^{14} and 10^{15} cm^{-2} are shown in Fig. 5.3. Helium release peaks are located at 490, 700, 950 and 1050 K and are in agreement with the earlier performed THDS study by Eleveld *et al.* [1994]. Assuming the first order release model, which can be justified in the case of D for high implantation doses, these temperatures correspond to activation energies of 1.2, 1.8, 2.5 and 2.8 eV, respectively. In the work of Eleveld *et al.* [1994] on helium irradiated Be it was also shown that after 600-800 K ramp annealing the helium-vacancy clusters evolve into bubbles which appear to be stable above 1000 K.

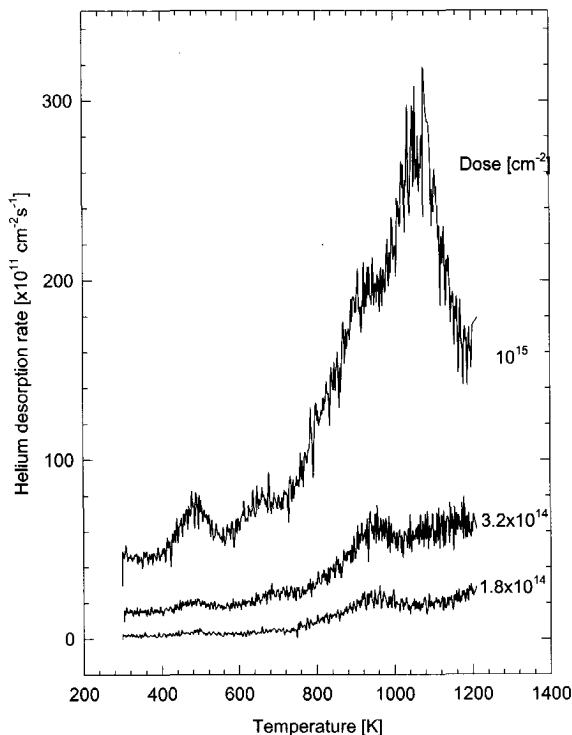


Fig. 5.3. Helium desorption spectra in Be after 3 keV ^4He implantation with doses of 1.8×10^{14} , 3.2×10^{14} and 10^{15} cm^{-2} .

In the following experiment the influence of the helium bubbles on the deuterium trapping in beryllium was investigated. ^3He ions were implanted in beryllium with 3 keV energy and doses 3.2×10^{14} and 10^{15} cm^{-2} . The sample was then ramp annealed up to 800 K to grow helium bubbles, before implanting with 1.2 keV deuterium ions to a dose of 10^{14} cm^{-2} . The resulting spectra are shown in Fig. 5.4 and the actual treatment of the sample before the measurements corresponding to the spectra A, B, C and D are presented in Table 5.1. In all spectra obtained with ^3He pre-implantation a new peak at 950 K is observed. This contribution to the release is ascribed to deuterium escape from the helium clusters or bubbles. The annealing of the sample at 800 K between the helium and deuterium implantation causes the 950 K peak to become broader. In the last experiment (spectrum D in Fig. 5.4) the annealing after the deuterium implantation was

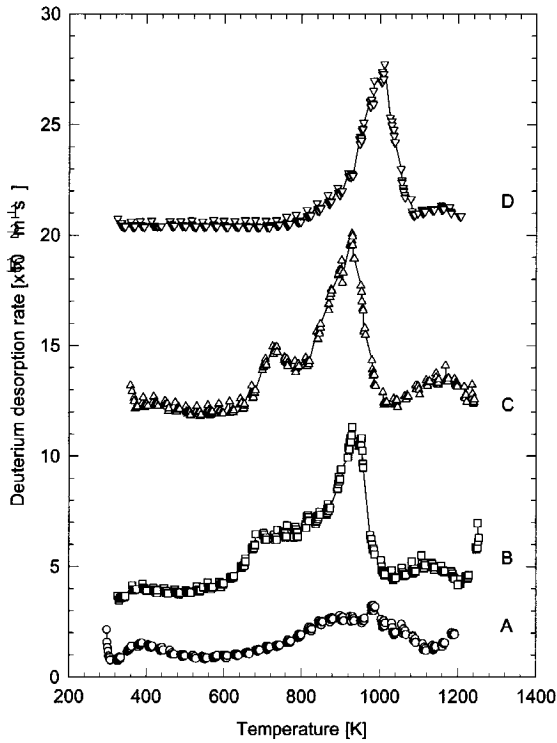


Fig. 5.4. Deuterium spectra in Be preimplanted with ^3He . The actual treatments of the sample for the spectra A, B, C and D are shown in Table 5.1.

Table 5.1. Treatment of the sample before the desorption measurements shown in Fig. 5.4.

Spectrum no.	^3He implantation dose [cm^{-2}]	Annealing at temperature [K]	D implantation dose [cm^{-2}]	Annealing at temperature [K]
A	-	-	10^{15}	-
B	3.2×10^{14}	-	10^{15}	-
C	3.2×10^{14}	800	10^{15}	-
D	10^{15}	800	10^{15}	800

performed in two steps. First, the sample was ramp annealed to 800 K to release the deuterium trapped in vacancy clusters, and then the sample was annealed to 1200 K. As a result, the desorption peak moved to higher temperatures (above 1100 K). A possible explanation for this effect is that during the second annealing the deuterium/helium bubbles became larger and therefore gave rise to a higher desorption temperature.

Deuterium has demonstrated a strong trapping to helium bubbles. However, at high implantation doses, because of the open porosity the traps are exposed to the surface and no strong retention of deuterium is expected.

Conclusions

1. Thermal desorption studies on deuterium trapping in a beryllium single crystal have revealed two desorption stages:
 - deuterium desorption from the surface characterised by an activation energy of 1 eV.
 - deuterium desorption from vacancy clusters and small deuterium bubbles with an activation energy of 1.8-2.5 eV.
2. Helium pre-implantation in beryllium with subsequent annealing at 800 K creates strong traps for deuterium. The activation energy for this release is estimated to be 2.7 eV.

CHAPTER 6

Tritium retention in ceramic breeding materials

Introduction

In the framework of the European Blanket Project (EBP) and ITER programs a series of EXOTIC experiments have been carried out at the HFR reactor in Petten on a number of lithium containing ceramics, including the prime candidates for the tritium breeder material: Li_4SiO_4 , Li_2TiO_3 and Li_2ZrO_3 . The objective of the experiments was to investigate tritium release characteristics and mechanical stability at high lithium burnups. Tritium release should be known in the first place for operational reasons: Fast recovery from the blanket is required to feed into reactor fuelling. Secondly, one needs to minimize inventory which might be released in case of an accident. The results of the experiments are reported by Kwast *et al.* [1995], (see also van der Laan 1998, Bakker *et al.* 1998). In the present work a physical model was designed to simulate tritium transport and release in the EXOTIC experiments. All the details concerning the experimental set-up can be found in Kwast *et al.* [1995]. Therefore, only a short description of the in-pile and post irradiation desorption measurements will be presented. In the in-pile experiments (see Fig. 6.1) the lithium-containing ceramic material in the form of pebbles or pellets is irradiated by neutrons in the reactor core. Tritium is produced as a result of the following nuclear reaction:



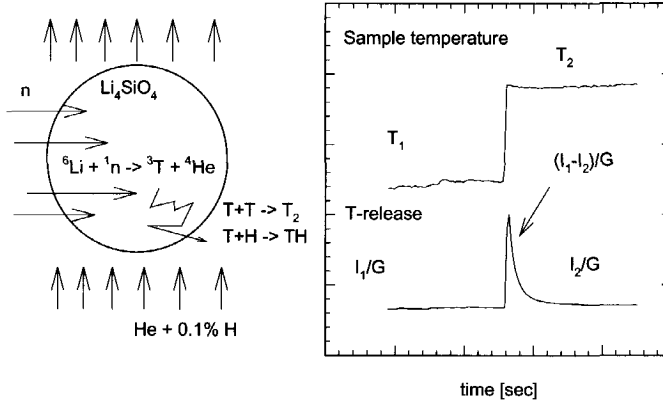


Fig. 6.1. Schematic set-up for in-pile experiments used in the EXOTIC programme.

The pebbles are purged with helium gas containing a small fraction of hydrogen: 0.01-1.0% . After recombination with hydrogen, TH molecules are swept away in the flow of the purge gas from the core and consequently the decay of tritium is registered in the ionisation chamber. The residence time τ_{res} is defined as follows:

$$\tau_{\text{res}} = \frac{I}{G}, \quad (6.2)$$

where I is the current tritium inventory and G is the tritium generation rate. In a number of the in-pile experiments the temperature was changed step-wise from T_1 to T_2 . The change in the inventory was characterised by the difference in the residence time:

$$\Delta\tau = \tau_1 - \tau_2 = \frac{I_1 - I_2}{G}. \quad (6.3)$$

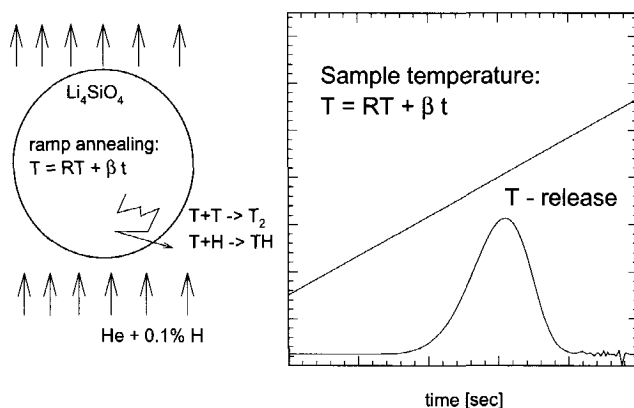


Fig. 6.2. Experimental set-up for the post-irradiated annealing experiments used in the EXOTIC programme.

In the post irradiation experiments (see Fig. 6.2) the neutron irradiated samples were removed from the core and subsequently ramp annealed in the same purging gas. Tritium desorption spectra were measured at various hydrogen partial pressures in the purge gas and at various annealing rates. In the next section the physical model which describes tritium transport and release in both types of experiments, in-pile and post irradiation, is discussed. On the basis of comparing the simulation results to the experimental data an optimal set of parameters characterising tritium release is determined. A method was also developed to compare the experimental results obtained from the in-pile and post irradiation experiments.

6.1. Physical model and basic assumptions

The transport of tritium from the moment it is produced due to the reaction ${}^6\text{Li}(n, {}^4\text{He}){}^3\text{T}$ until tritium radioactive decay is detected by the ionisation chamber can be described by the following number of steps:

- 1) bulk diffusion inside the grain (grain size ranges from 0.2 to 30 μ);
- 2) recombination at the grain surface with hydrogen;

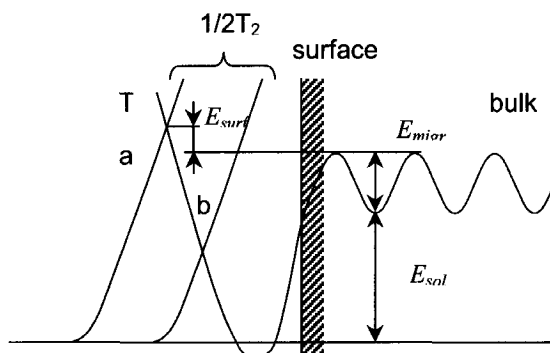


Fig. 6.3. Potential diagram for T and T₂ in the near surface region: a) presents the case with the surface barrier and b) without the surface barrier.

- 3) intergranular diffusion to the surface of the pebble (pebble size is 0.3-0.5 mm);
- 4) transport in the purge gas.

In the model presented below steps (3) and (4) are considered as being fast compared to the steps (1) and (2). Therefore, only the bulk diffusion and the recombination at the grain surface are simulated. Also no exchange interactions with water are taken into account.

Consider a grain as a sphere of radius R . In this case the non-stationary diffusion equation in the spherical geometry should be used:

$$\frac{\partial C}{\partial t} = \frac{1}{r^2} \frac{\partial}{\partial r} (r^2 D(T) \frac{\partial C}{\partial r}) + S, \quad (6.4)$$

where C is the volume tritium concentration, S is the tritium source and $D(T) = D_0 \exp(-E_m/(kT))$ is the diffusion coefficient with E_m being the migration energy. The following boundary conditions were used:

$$\left. \frac{dC}{dr} \right|_{r=0} = 0 \quad (6.5)$$

$$-D \left. \frac{dC}{dr} \right|_{r=R} = k_2 C^2 + k_2 C C_H, \quad (6.5)$$

where the parameter $k_2 = k_{02} \exp(-Q_k/kT)$ defines the tritium-tritium and tritium-hydrogen recombination rates. In the potential diagram shown in Fig. 6.3 two cases are considered. In case a) the intersection point between the potential curves for T and $1/2T_2$ is higher than the sum of the energy of solution and the migration barrier in the bulk: $E_{sol} + E_m$. In this case tritium molecules experience a surface barrier E_{surf} after the recombination takes place, and the activation energy is $Q_k = E_{surf} + E_m$. In the present model no surface barrier is considered (shown as (b) in Fig. 6.3) and, therefore, Q_k has the same value as the migration energy E_m . It was also assumed that the tritium-hydrogen recombination does not influence the hydrogen concentration at the surface C_H which is defined from the following balance equation:

$$0 = -D \left. \frac{dC_H}{dr} \right|_{r=R} = -k_1 p + k_2 C_H^2. \quad (6.6)$$

The first term in the right-hand side of the equation presents the uptake of hydrogen at the surface and is proportional to the external hydrogen partial pressure p in the purge gas. The second term describes hydrogen recombination at the surface in the same manner as in Eq. 6.5. The left-hand side of the equation is equal to zero indicating that the uptake is balanced by the release and the hydrogen concentration is at equilibrium. Since the coefficients k_1 and k_2 both have the Arrhenius type of temperature dependence the hydrogen concentration at the surface C_H can be described by the following equation:

$$C_H = C_0 \exp\left(-\frac{Q_H}{kT}\right) \sqrt{p}, \quad (6.7)$$

where p is the external hydrogen partial pressure and C_0 and Q_H are the parameters to be defined from experiment.

Before considering the cases of the in-pile and post irradiation experiments separately the following substitutions will be made:

$$\begin{aligned}\xi &= \frac{D}{R^2} t, & \Sigma &= S \frac{R^2}{D} \Omega, \\ x &= \frac{r}{R}, & u &= C \Omega,\end{aligned}\tag{6.8}$$

and

$$\alpha = k_2 C_H \frac{R}{D},\tag{6.9}$$

where $\Omega = a^3$ and a is the lattice parameter.

in-pile experiments

Taking into account that in the in-pile experiments the tritium inventory remains in equilibrium, Eq. 6. 4 can be written in the stationary form:

$$\frac{1}{x^2} \frac{d}{dx} \left(x^2 \frac{du}{dx} \right) + \Sigma = 0,\tag{6.10}$$

with the following boundary conditions:

$$\begin{aligned}\frac{du}{dx} &= 0, & x &= 0 \\ -\frac{du}{dx} &= \alpha u, & x &= 1.\end{aligned}\tag{6.11}$$

The solution for the boundary value problem 6.10-6.11 is:

$$u(x) = \frac{\Sigma}{3} \left(\frac{1}{2} + \frac{1}{\alpha} - \frac{x^2}{2} \right).\tag{6.12}$$

Consequently, according to Eq. 6.2, the residence time τ_{res} is:

$$\tau = \frac{4\pi \int_0^R C(r)r^2 dr}{S \frac{4}{3}\pi R^3} = \frac{R^2 \int_0^1 u(x)x^2 dx}{D \Sigma/3} \quad (6.13)$$

After substitution of $u(x)$ from Eq. 6.12 into Eq. 6.13 the residence time is:

$$\tau_{res} = \frac{R^2}{3D} \left(\frac{1}{5} + \frac{1}{\alpha} \right). \quad (6.14)$$

Two limiting cases will be considered. For $\alpha \rightarrow \infty$ the residence time depends only on the diffusion coefficient D and the grain size R :

$$\tau_{res} \approx \frac{R^2}{15D}. \quad (6.15)$$

According to Eq. 6.9 α increases with the increase of the hydrogen pressure C_H or the coefficient k_2 . High values for both parameters provide efficient recombination at the surface. Therefore, tritium desorption in this case is limited only by bulk diffusion. The opposite limiting case is realised at $\alpha \rightarrow 0$, e. g. at low hydrogen concentrations C_H . The residence time depends now only on the parameters characterising tritium recombination at the surface:

$$\tau_{res} \approx \frac{R^2}{3D} \frac{1}{\alpha} = \frac{R^2}{3D} \frac{D}{k_2 C_H R} = \frac{R}{3k_2 C_H}. \quad (6.16)$$

post irradiation experiments:

For the post irradiation ramp anneals the non-stationary form of Eq. 6.4 should be used:

$$\frac{\partial u}{\partial \xi} = \frac{1}{x^2} \frac{\partial}{\partial x} \left(x^2 \frac{\partial u}{\partial x} \right). \quad (6.17)$$

Note that in this case the tritium source $S = 0$. The boundary conditions are the same as in Eq. 6.11. After using the method of separation of variable the solution is expressed in the following form:

$$u(\xi, x) = C_i \Omega e^{-\lambda^2 \xi} \frac{\sin(\lambda x)}{x}, \quad (6.18)$$

where C_i is the initial concentration value which depend on the initial contents of tritium in the grain I_0 ($I_0 = 4/3 \pi R^3 C_i$). The parameter λ is found from the transcendental equation:

$$\alpha = \frac{\sin(\lambda) - \lambda \cos(\lambda)}{\sin(\lambda)}. \quad (6.19)$$

Although Eq. 6.19 has infinite number of solutions because of the decaying exponent term in Eq. 6.18 only the solutions from the interval $0 \leq \lambda < \pi/2$ will be considered. In the original variables the tritium concentration as a function of temperature and radius is

$$C(r, t) = C_i e^{-\frac{D}{R^2} \lambda^2 t} \frac{\sin(\lambda r/R)}{r/R}. \quad (6.20)$$

In order to compare the ramp annealing experiments with the in-pile residence time measurements a time constant which characterises tritium release during ramp annealing should be introduced. Equation 6.20 suggests definition of the characteristic time τ_{ramp} by:

$$\tau_{\text{ramp}} = a \frac{R^2}{D} \frac{1}{\lambda^2}, \quad (6.21)$$

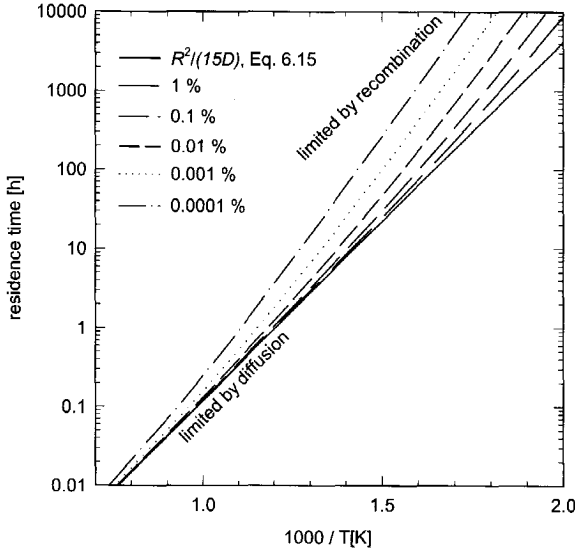


Fig. 6.4. Residence time τ_{res} as a function of reciprocal temperature calculated for various hydrogen fractions in the purge gas. The limiting case, for $\alpha \rightarrow \infty$ (diffusion limited) is shown by the solid line which is calculated according to Eq. 6.15 with the parameters taken from Table 6.1

where $a = 2/3$ for $\alpha \rightarrow \infty$ and $a = 1$ for $\alpha \rightarrow 0$. The choice for the values of the constant a is based on the following considerations. For the case of $\alpha \rightarrow \infty$, large values of α in the left-hand side of Eq. 6.19 can occur only if the right-hand expression has a pole, which is the case at $\lambda = \pi$. From comparing $\tau_{ramp} \approx a(R^2/D)/\pi^2$ with Eq. 6.15 one finds that $a \approx 2/3$. Considering the other limiting case it can be shown that for $\alpha \rightarrow 0$ also $\lambda \rightarrow 0$. Therefore, the right-hand side of Eq. 6.19 can be approximated by the Taylor series:

$$\alpha \approx \frac{\lambda - \frac{\lambda^3}{6} - \lambda(1 - \frac{\lambda^2}{2})}{\lambda} = \frac{\lambda^2}{3}. \quad (6.22)$$

Consequently,

$$\tau_{ramp} \approx a \frac{R^2}{D} \frac{1}{3\alpha}. \quad (6.23)$$

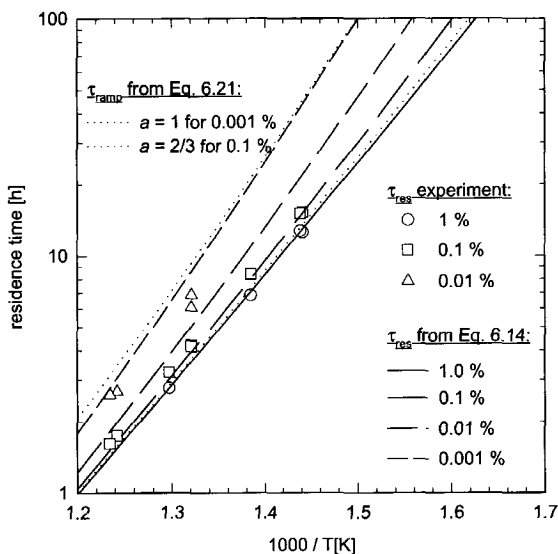


Fig. 6.5. Residence time τ_{res} obtained from the in-pile measurements (shown by symbols) and from simulations (shown by lines) for various hydrogen fractions in the purge gas. For two hydrogen pressures, $p = 3 \text{ Pa}$ (0.001 %) and $p = 300 \text{ Pa}$ (0.1 %), τ_{res} is compared to τ_{ramp} calculated according to Eq. 6.21 with the constant $a = 1$ for $p = 3 \text{ Pa}$ and $a = 2/3$ for $p = 300 \text{ Pa}$

Comparing this equation to Eq. 6.16 one obtains $a = 1$. Equation 6.21 provides the way to compare the in-pile and post irradiation experiments. According to this equation the residence time from the in-pile experiments τ_{res} should be bounded between the values of τ_{ramp} evaluated at $a = 1$ and $a = 2/3$, and should approach these values in the limiting case: at $a = 1$ for $\alpha \rightarrow 0$ and at $a = 2/3$ for $\alpha \rightarrow \infty$.

6.2. Fitting to experiment. Results and discussion

In Fig. 6.4 the residence time evaluated according to Eq. 6.12 is plotted as a function of reciprocal temperature. The simulations were carried out for a number of various hydrogen partial pressures ranging from 0.03 to 3000 Pa which correspond to hydrogen fractions from $10^{-5} \%$ to 1.0 %, respectively. The limiting case for $\alpha \rightarrow \infty$ is

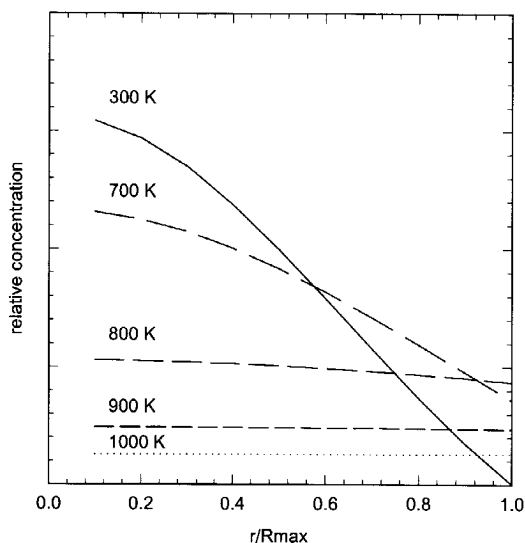


Fig. 6.6. Tritium concentration as a function of radius is plotted for a number of temperatures during the simulation of ramp annealing experiment.

Table 6.1. Input parameters used for in-pile and out of pile simulations.

Parameter	Value	Comment
<u>grain radius</u>		grain size of caps. no.24.1 is 10-30 μm
R [cm]	15×10^{-4}	
<u>tritium diffusion coefficient.</u>		
D_0 [cm^2s^{-1}]	1.2×10^{-5}	
E_m [eV]	0.9	
<u>recombination coefficient:</u>		
k_{20} [cm^4s^{-1}]	$k_{20}C_0=7.3$	0.5 in case of ramp annealing
Q_k [eV]	0.9	
<u>hydrogen surf. concentration:</u>		
C_0 [$\text{cm}^{-3}\text{Pa}^{-0.5}$]	$k_{20}C_0=7.3$	0.5 in case of ramp annealing
Q_H [eV]	0.4	
<u>hydrogen partial pressure:</u>		
p [Pa]	300 for 0.1 %	see Kwast et al. [1995]

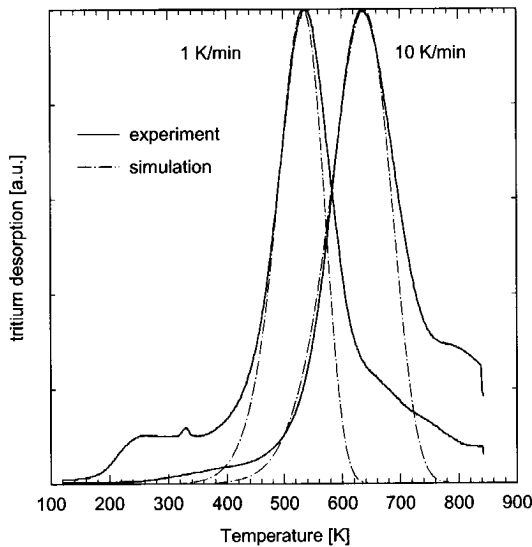


Fig. 6.7. Tritium desorption spectra experimentally obtained for two different annealing rates, $\beta = 1$ K/min and $\beta = 10$ K/min, are compared to the spectra obtained from the simulations.

also shown by the solid line and is indicated as *diffusion limited*. The other limiting case for $\alpha \rightarrow 0$, is realised for low values of the hydrogen pressure and is indicated as *recombination limited*. Note that for temperatures $T > 1000$ K tritium desorption is limited by bulk diffusion even in the cases of relatively low hydrogen pressure. In Fig. 6.5 the results of the simulations are compared to the residence time values obtained from the in-pile measurements, shown by the symbols. The parameters used in the simulations which provide the best match with the experimental data are shown in Table 6.1. Since the boundary condition Eq. 6.5 involves k_2 and C_H as a product, only the sum of the exponent arguments can be defined directly from the fitting procedure: i. e. $Q_k + Q_C = 1.3$ eV. However, the assumption that there is no surface barrier for TH desorption discussed in the previous section suggests that $Q_k = E_m = 0.9$ eV, leaving $Q_H = 1.3 - 0.9 = 0.4$ eV.

The broken lines in Fig. 6.5 present τ_{ramp} calculated according to Eq. 6.21 for two hydrogen pressures $p = 3$ Pa and $p = 300$ Pa. In the first case parameter a was chosen as $a = 3/2$ and in the second one as $a = 1$. Note that for $p = 3$ Pa, τ_{res} approaches τ_{ramp} at low

temperatures, i. e. for $\alpha \rightarrow 0$, and for $p = 300$ Pa, τ_{res} approaches τ_{ramp} for high temperatures, i. e. for $\alpha \rightarrow \infty$.

In Fig. 6.6 the simulation results of ramp anneals are presented: the tritium concentration is plotted as a function of the radius for different annealing temperatures. Note that even if in the beginning of the ramp the release is *diffusion limited*, because of decrease of the tritium inventory in the sample at higher temperatures the release shifts to *recombination limited* case. The non-zero values of the tritium concentration at the surface are the manifestation of the recombination process which limits tritium recombination.

In Fig. 6.7 two ramp annealing spectra measured for the annealing rates $\beta = 1$ K/min and $\beta = 10$ K/min are compared with the simulation results. The parameters of the simulation are the same as for the in-pile simulations except for the value C_0 (see Table 6.1). This discrepancy probably arises from the fact that the pebbles in the in-pile experiments experienced a temperature gradient. Hence, the measured residence time represents the value averaged over the pebbles at temperatures varying within the range of 80-100 K [Kwast et al. 1995]. However, the model can be adapted to this case.

Conclusions

1. The model proved to be capable to simulate the in-pile tritium release measurements and the post irradiation ramp annealing measurements used in the EXOTIC programme.
2. On the basis of the simulation results a list of parameters is determined which provide the best consistency with the experimental data.
3. It was found that for hydrogen partial pressures $p > 300$ Pa (0.1%) tritium release is limited by bulk diffusion.

CHAPTER 7

Nanosize cavities in silicon and MgO

Introduction

This chapter discusses the formation of cavities in Si and MgO. Cavities of nanometer size in Si were found to be useful for gettering transition metal impurities from the Si matrix [Follstaedt *et al.* 1996]. In the case of MgO, cavities can be used to form metal nanoclusters which are known to change the optical properties of the MgO matrix due to Mie resonance [Zimmerman *et al.* 1998, White *et al.* 1998, Chakraborty 1998]. The first section of this chapter presents the model which provides an explanation for the experimentally observed critical implantation dose necessary to form the cavities. The experimental study covers the following topics:

- formation of cavities in Si and MgO by helium and deuterium implantation;
- stability of cavities in Si in the flow of self-interstitials generated at the surface;
- permeation of deuterium from cavities in Si and MgO.

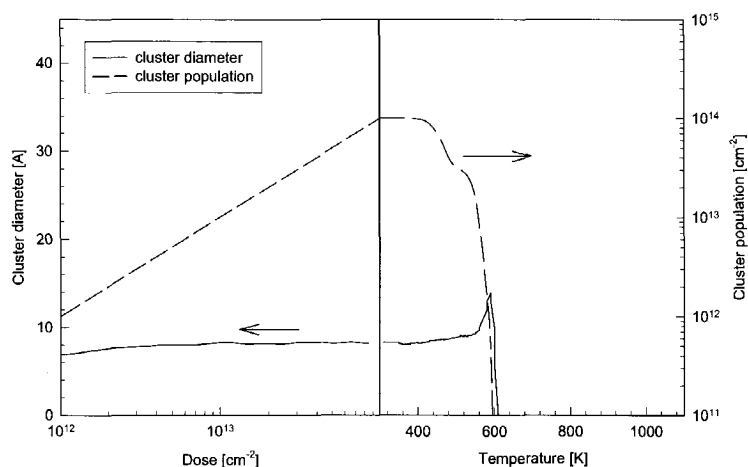
7.1 Threshold implantation dose for cavities formation in silicon

The formation of cavities in Si was first observed by Griffioen *et al.* in 1987. In this work, a Si sample was subjected to a high dose helium implantation of 10 keV, $2 \times 10^{17} \text{ cm}^{-2}$, followed by annealing at 1275 K. During the annealing the implanted He was released and the formation of cavities was observed in TEM. Later it was shown that the cavities were also formed by H implantation [Van Veen 1995 MRS]. In both cases a critical dose corresponding to a concentration of the implanted ions of 1-5 at. % was necessary to form the cavities. Recently it was discovered that the cavities trap transition metal impurities and this effect has been proposed as a method of purifying the Si matrix [Myers *et al.* 1998, Myers *et al.* 1996, Follstaedt *et al.* 1996, Wong-Leung and Williams 1996]. Metals such as Cu, Ni, Co, Fe and Au have already been reported to have a binding of 1.5-2.2 eV to the cavity wall. Up to the present no clear understanding of the cavity formation process in Si has emerged. Here, this process is studied using the computer code MODEX described in Chapter 2. In the discussion which follows, only He implantation was simulated. Nevertheless, the model is applicable in the case of H implantation, as will be discussed below. The mobility of the primary point defects, i. e. interstitial helium, vacancies and Si self – interstitials, is shown in Table 7.1. It can be seen that vacancies and self-interstitials are mobile in Si at room temperature (RT),

Table 7.1. Migration and formation energies of point defects in Si

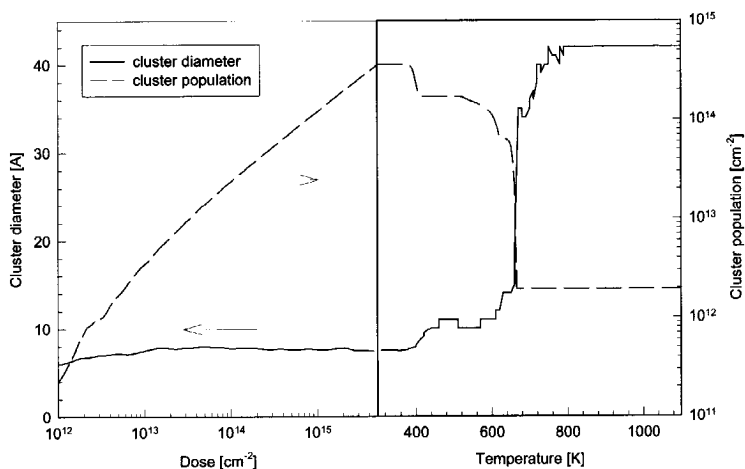
Defect	E^{migr} [eV]	E^{form} [eV]	Source
V	0.37	3.19	Baskes <i>et al.</i> 1989
I		4.81	Baskes <i>et al.</i> 1989
He	1.34	0.46	Van Wieringen and Warmoltz, 1956

the temperature usually used for implantation. Helium atoms, on the other hand, are not mobile and trap vacancies thus nucleating HeV clusters. The stability of small He-V clusters is limited by the helium permeation energy in Si, $E^{\text{perm}} = 1.8 \text{ eV}$,



7.1. MODEX simulation of 2.5 keV helium implantation in silicon: total cluster population and the mean cluster diameter are plotted versus implantation dose and annealing temperature. No cavity formation is observed.

measured by Van Wieringen and Warmoltz [1956]. However, larger clusters or bubbles appear to be more stable and, as was shown by Evans *et al.* [1987] and Van Veen [1991], helium release and formation of nanosize cavities take place at 1000-1100 K. These experimental data were used to simulate the formation of nanocavities in Si with the program MODEX. In Fig. 7.1 the results of the simulation carried out for the case of “low dose” helium implantation are presented: the total cluster population and the mean cluster size are plotted, first versus the implantation dose and then versus the annealing temperature. During the implantation stage both the population of the clusters ($V_n\text{He}_m$ with $n > 0$, $m \geq 0$) and the mean cluster size increase. However, after reaching an implantation dose of 10^{14} cm^{-2} the mean cluster size saturates at about 1 nm. In several cases even a decrease of the mean cluster size was observed. That happens because the concentration of helium atoms, which are the main sink for vacancies, increases almost linearly with the implantation dose. Therefore, at high doses more vacancies are trapped at interstitially dissolved helium, forming HeV – complexes, and fewer vacancies are trapped at the He_nV_m – clusters, limiting further growth. On the other hand, the flow of



7.2. MODEX simulation of 2.5 keV helium implantation in silicon: the total cluster population and the mean cluster diameter are plotted versus implantation dose and annealing temperature. The simultaneous increase in the cluster diameter and decrease in cluster population which takes place at 650-700 K indicates the formation of cavities, i.e. V_n -clusters with $n > 1000$.

self-interstitials is almost constant and He_nV_m -clusters are their main sink. Consequently, relatively large He_nV_m - clusters, with $m = 5-10$, created at the beginning of the implantation, disappear at high implantation doses. That explains why one needs to anneal the sample after the implantation to form cavities. During the implantation stage, helium atoms are used to trap the vacancies inside the sample. In the absence of He, vacancies which are mobile at RT would be absorbed by the surface. Hydrogen (or deuterium) can also be used to immobilise vacancies. Moreover, the cavities can be formed in Si even without gas provided the vacancies are frozen inside the sample. Recently this idea was implemented by Williams *et al.* [1999] when cavities were formed in Si by low temperature, $T = 77$ K, Si ion implantation and subsequent annealing. However, even accumulation of vacancies during the implantation stage does not guarantee the formation of cavities. During the annealing, helium (or hydrogen) is released from the He_nV_m clusters around 1000-1100 K. Small vacancy clusters, V_m with $m < 50$, which are presumably not stable, dissociate providing a source of mobile vacancies. Consequently, the competition between the two main sinks for vacancies, the

outer surface and the larger and more stable clusters, determine the conditions for the formation of cavities. In Fig. 7.1 the annealing of the sample does not result in the formation of cavities because the outer surface is the dominant sink for the vacancies. In the case of "high dose" implantation shown in Fig. 7.2, retrapping of the dissociated vacancies during the annealing dominates and cavities are formed. Evidently, in order to allow the formation of cavities during the coalescence the vacancy diffusion length inside the damaged area should be much less than the distance to the outer surface. That implies the critical implantation dose of $0.5 \times 10^{16} \text{ cm}^{-2}$ below which nanoclusters cannot be formed.

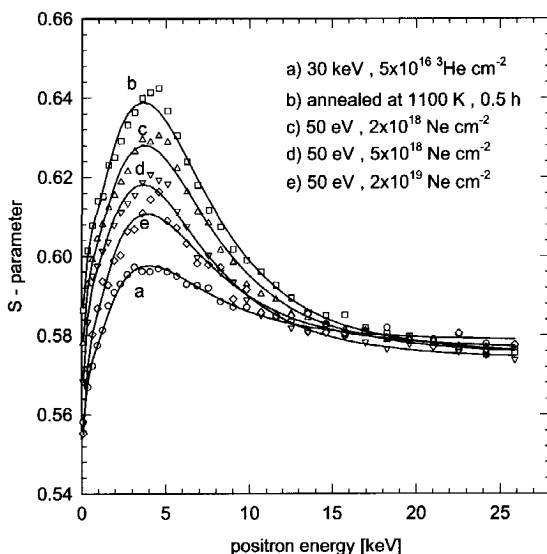
7.2 Interaction of nanocavities with self-interstitials

In the study reported here the cavities were filled with Si self-interstitials in order to regain the original silicon structure. The interstitials were produced by low-energy Ne and Kr irradiation in a plasma ion source. The sequence of the experimental treatments of the monocrystalline (100) Si samples is shown in Table 7.2. To create cavities the

Table 7.2. Sequence of treatments of Si samples and the observed effects.

Treatment	Result
1 30 keV He implantation	Formation of helium-vacancy clusters
2 1100 K, 0.5 h annealing	Release of helium; formation of cavities
3 50 eV Ne surface irradiation	Filling of cavities with self-interstitials
4 1000 K, 0.5 h annealing	Annealing of small clusters
5 Ramp annealing to 1400 K	TDS check for Ne presence in the sample

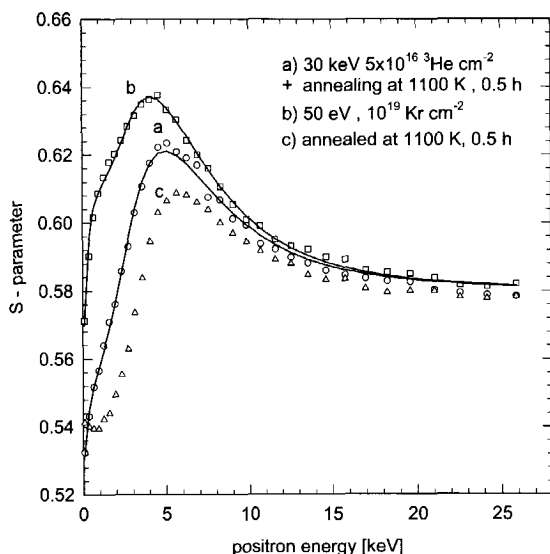
samples were implanted at room temperature with 30 keV ^3He ions with a dose of $5 \times 10^{16} \text{ cm}^{-2}$. Subsequently, 1100 K anneals were performed in a vacuum better than 10^{-7} torr. To generate self-interstitials the samples were irradiated with 50 eV Ne and Kr in a plasma ion source. The doses varied from 10^{18} to $3 \times 10^{19} \text{ cm}^{-2}$. The energy of 50 eV was chosen to avoid introduction of irradiation defects well beneath the surface region. For the same reason the irradiation temperature was kept above 600 K. Thermal desorption



7.3. *S* - curves demonstrating the effect of 50 eV Ne irradiation with various doses. The VEP measurements were carried out after the following sample treatments: a) 30 keV He $5 \times 10^{16} \text{ cm}^{-2}$ implantation at room temperature; b) annealing at 1100 K for 0.5 h; 50 eV Ne irradiations at 620 K with the doses c) $2 \times 10^{18} \text{ cm}^{-2}$, d) $5 \times 10^{18} \text{ cm}^{-2}$, e) $2 \times 10^{19} \text{ cm}^{-2}$. Solid lines present the experimental data fitted with the VEPFIT code.

spectroscopy (TDS) was used to check the presence of Ne inside the sample. The evolution of the implantation induced defects after every treatment of the sample was monitored by the Positron Beam Analysis described in Chapter 3. Two computer codes were involved in the analysis of the experimental data: The Monte - Carlo program MODEX was used to simulate all the processes shown in Table 7.2, i. e. He and Ne implantations and the anneals. To fit the spectra of the positron measurements the VEPFIT program was used [Van Veen *et al.* 1990].

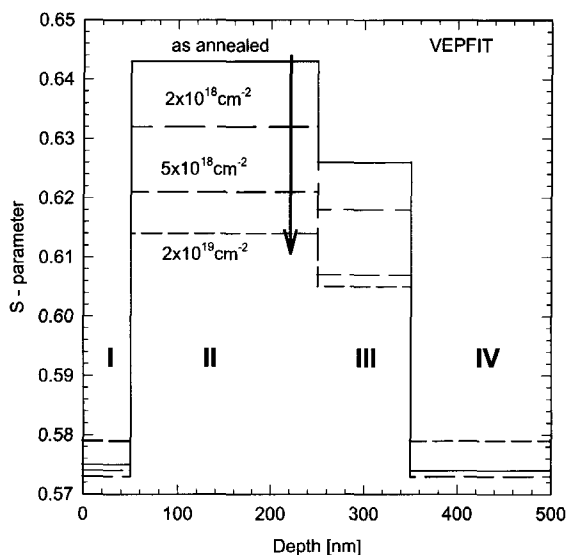
The measured *S*-parameter as a function of the positron energy for Ne and Kr irradiation is shown in Figs. 7.3 and 7.4, respectively. In both cases cavities were created by 30 keV ^3He implantation: curve (a) in Fig. 7.4; and subsequent annealing at 1100 K: curve (b) in Fig. 7.4 and (a) in Fig. 7.5. A high *S* value indicates the presence of free volume, i. e. cavities. Subsequently, as shown in Table 7.2, the samples were irradiated with 50 eV Ne and Kr. In the case of the Ne irradiation the *S*-parameter gradually



7.4. *S*-curves demonstrating the effect of 50 eV Kr irradiation with various doses. The VEP measurements were carried out after the following sample treatments: a) 30 keV He $5 \times 10^{16} \text{ cm}^{-2}$ implantation at room temperature followed by 1100 K annealing; b) 50 eV Kr irradiations at 620 K with a dose of 10^{19} cm^{-2} ; c) annealing at 1100 K for 0.5 h. Solid lines present the experimental data fitted with the VEPFIT code.

decreases with increase of the irradiation dose. Interstitial atoms generated at the surface diffuse into the bulk of the material and become trapped at the cavities. Consequently, the cavities are reduced in size and the *S*-parameter decreases. However, this effect is not observed in the case of Kr irradiation (Fig. 7.4, curve (b)). In contrast to Ne, Kr is not mobile at the irradiation temperature $T = 620 \text{ K}$ [Greuter *et al.* 1994]. Therefore, Kr-vacancy type defects are formed in the near surface region and act as a strong trap for interstitials, preventing them from diffusion into the bulk of the material where cavities are located. By subsequent annealing at 1100 K all the Kr induced defects were removed (curve (c) Fig. 7.4). During the annealing, both Kr and interstitials can fill up cavities resulting in low *S*-values.

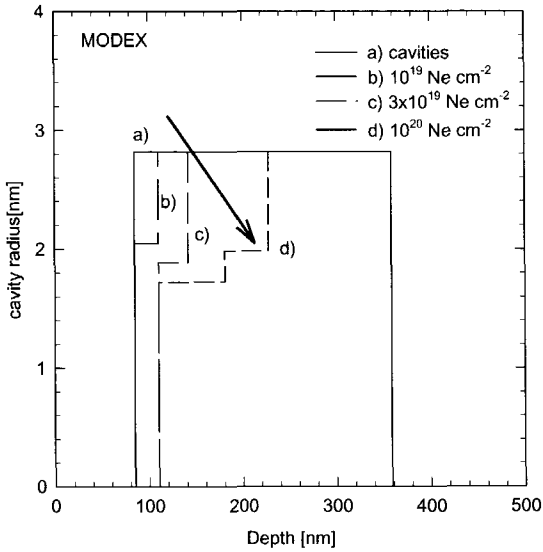
The experimental *S*-curves shown in Figs. 7.3 and 7.4 were fitted with VEPFIT. The results of the fits carried out for the Ne irradiations are shown in Fig. 7.5, where *S*-parameters are plotted versus depth.



7.5. Depth dependence of the S -parameter obtained from the Ne irradiation data fitted with the VEPFIT code.

The fitting model includes 4 slabs. The slabs I and IV are characterised by the S - value of the defect-free silicon. For the set-up used in this experiment this value is $S \sim 0.58$. The slabs II and III contain cavities providing high S values. With the increase of the Ne irradiation dose the S values for the slabs II and III decrease in the agreement with the fact that the cavity size decreases.

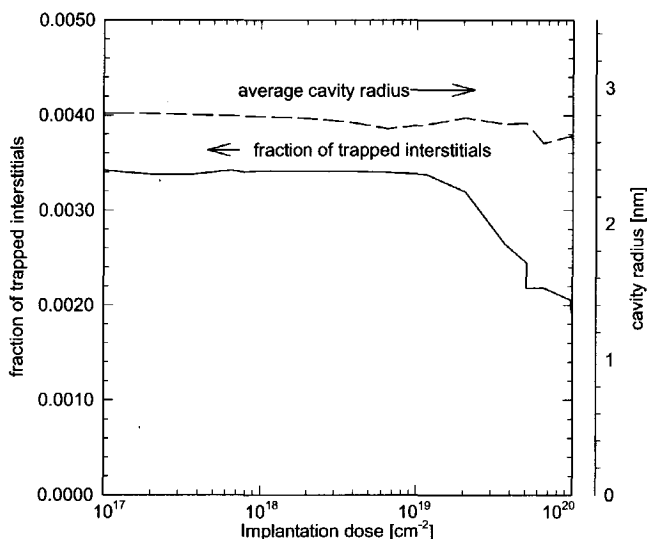
The decrease of the cavity size due to filling by interstitials was simulated by the Monte-Carlo code MODEX. The results of this simulation are shown in Fig. 7.6. In this simulation a layer of cavities located between 100 nm and 350 nm was subjected to 50 eV Ne irradiation. Each cavity of 3 nm radius was represented by a cluster of 5000 vacancies. The initial concentration of the cavities within the layer was 10^{19} cm^{-3} . With the increase of the Ne irradiation dose the cavities decrease in size, with the strongest decrease at shallow depths. It was intended to achieve complete re-growth of the Si structure. However, for doses above $10^{19} \text{ Ne cm}^{-2}$, the S -parameter no longer decreases. According to the computer simulations the fraction of the interstitials trapped inside the sample, $\sim 0.3\%$, depends on the sink strength of the traps. However, due to the reduction



7.6. The decrease in the cavity radius during 50 eV Ne irradiation as a function of depth. Results are obtained with the simulation code MODEX.

in cavity size the sink strength is reduced and, consequently the fraction of the interstitials trapped in the bulk decreases. This effect is demonstrated in Fig. 7.7 where the fraction of the interstitials trapped at the cavities and the mean cavity radius averaged over all the cavities present in the sample are plotted versus the Ne implantation dose. Note that despite small fluctuations the mean cavity radius stays above 2.5 nm. The reduction of the trapped interstitial fraction is mainly caused by the decrease in the size of the cavities located at shallow depths as is shown in Fig. 7.6.

Another possible explanation accounting for the observed decrease in the S -parameter is that the cavities are filled with Ne. Two checks were carried out to eliminate this possibility. First, the samples were annealed at 1000 K for 0.5 h. after the Ne irradiation. If during the irradiation the cavities were filled with Ne the S -parameter would have increased because of the structural relaxation. No such increase was observed. Secondly, a TDS study was carried out on two samples after the Ne irradiation. The TDS results demonstrate that the samples with an area of 0.1 cm^2 exposed to an irradiation dose of $2 \times 10^{19} \text{ Ne cm}^{-2}$ do not contain more than 10^{12} Ne atoms.



7.7. Calculated decrease in the fraction of Si self-interstitials trapped by cavities as a function of the Ne irradiation dose. The average cavity radius is also shown. Results are obtained with the simulation code MODEX.

7.3 Formation of nanocavities in MgO by helium and deuterium implantation

Nanocavities in MgO were formed in a similar way as was previously described for Si in Section 7.1. The MgO (100) monocrystalline samples purchased from Kelpin were implanted with 30 keV ^3He or 15 keV D with various doses ranging from 10^{15} to 10^{16} cm^{-2} . The implantations were carried out at the DANFYSIK 30 kV ion accelerator described in Chapter 3. The ^3He contents was monitored with the help of Neutron Depth Profiling (NDP) and the presence of free-volume defects related to the cavities was measured by Positron Beam Analysis. The evolution of ^3He contents in the MgO sample and the S -parameters measured during the step-wise anneals is shown in Fig 7.8. (for the definition of the S -parameter see Chapter 3.) The release of He observed at 1150-1350 K is correlated with a sharp increase in the S -parameter indicating the formation of cavities. It is quite remarkable that because of high anisotropy in the surface energy

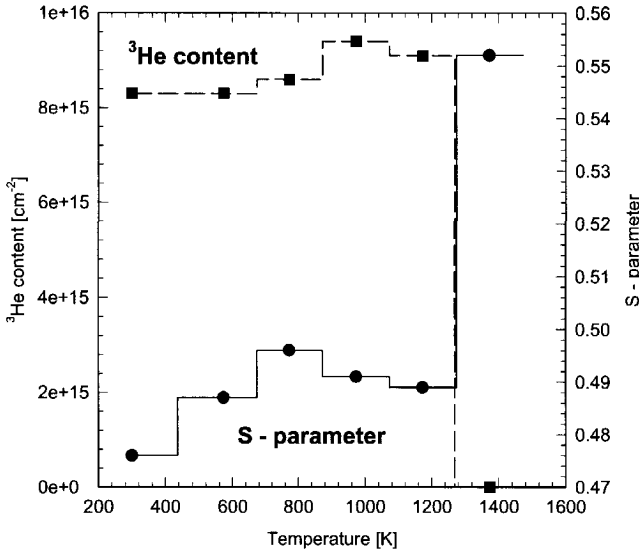


Fig. 7.8. Evolution of ^3He content and S -parameter with the annealing temperature measured in MgO after 30 keV, 10^{16} cm^{-2} ^3He implantation.

the cavities in MgO have a rectangular form as shown in the TEM picture in Fig. 7.9 [Kooi *et al.* 2000].

In Fig. 7.10 the S -curves measured directly after ^3He implantation and after subsequent annealing are compared to those measured for Si. The symbols represent the measured data while the lines are obtained as a result of fitting with the VEPFIT program described by Van Veen *et al.* [1990]. The increase of the S -parameter for the as implanted Si indicates the presence of small helium filled vacancy clusters. In the case of MgO almost no increase is observed. Two explanations can account for this fact. First, the literature value for the threshold displacement energy E_d in MgO for both oxygen and magnesium sublattices is more than 60 eV which is 3 times higher than that for Si [Zinkle and Kinoshita 1997, Crawford 1984]. Secondly, according to Kotomin *et al.* [1998] the radius of direct recombination for a Frenkel pair in the oxygen sublattice in MgO is about 4 lattice parameters. Both considerations suggest that from the 23 Frenkel pairs per ion resulting from the TRIM simulation (see Table 3.1) hardly one vacancy presumably filled with a helium atom survives direct recombination.

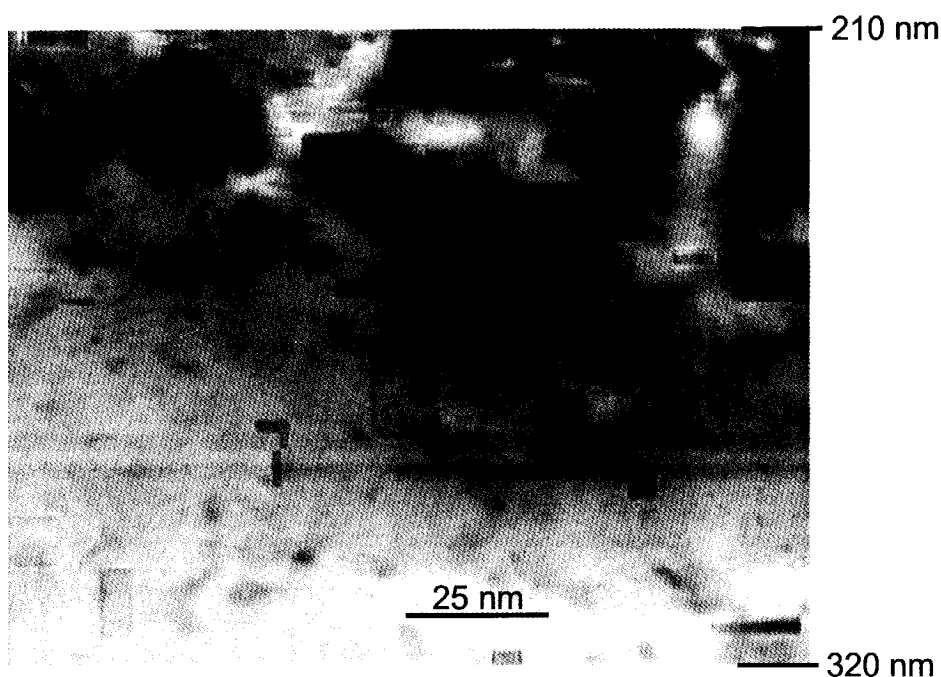


Fig. 7.9. TEM picture of rectangular nanocavities formed in MgO.

Although the bulk S values for Si and MgO are different because of different electron densities the S values measured at the surface are remarkably similar. It should be noted that Si is usually covered with a thin oxide layer, which is difficult to avoid. Evidently, the S values measured at the surface for both materials are characteristic for the oxides.

It was also discovered that the cavities are formed more readily by D implantation rather than He. In Fig. 7.11 the S - parameter measured for the damaged layer is plotted as a function of the implantation doses for D and ^3He implantations. The temperature of the annealing which followed the implantation is indicated at every experimental point and corresponds to the annealing step which yields the highest S . All the points for D implantation lie higher than those for He corresponding to the same implantation dose. The fact that D implantation in MgO provides higher S values can have several reasons. In the first place one has to consider the charges attributed to the point defects produced

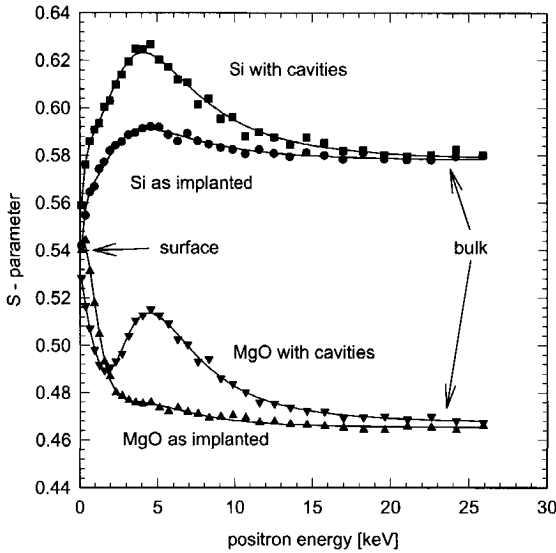
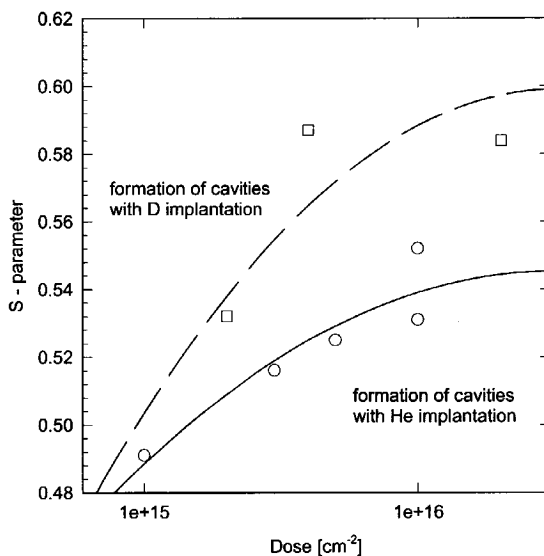


Fig. 7.10. S - curves measured for Si and MgO directly after ^3He 30 keV implantation and subsequent annealing at 1200 K for Si and 1370 K for MgO.

by implantation. Oxygen vacancies, the most commonly observed defects in MgO, are produced in at least two charge states: the O - vacancy with one trapped electron known as the F^+ - centre and the O - vacancy with two trapped electrons or F - centre [Crawford 1984]. An agglomeration of those defects would result in accumulation of charge which would prevent the cluster from further growth. Different from neutral helium, hydrogen in the H^+ state can compensate this accumulation of charge. However, according to literature hydrogen is usually observed in the H^- state [Freund *et al.* 1982]. Another mechanism of defect formation was proposed by Freund *et al.* [1982]. According to this model two hydrogen atoms and one Mg- vacancy (V - centre) can form a neutral peroxy group $\text{H}_2\times\text{O}_2$ removing two O ions from their lattice positions. On the other hand, if the clusters of O - vacancies are negatively charged they will attract positrons due to Coulomb interaction which also results also in higher S values. However, at present there is not enough experimental evidence to rule out any of the explanations discussed above and more experimental study is required.



7.11. *S* - parameter measured for the nanocavities formed in MgO by means of He and D implantation at various implantation doses.

7.4. Permeation of deuterium from nanocavities formed in MgO and Si

In the set of experiments presented in this section the permeation of deuterium from nanocavities was studied. The nanosize cavities were formed in Si and MgO samples as described in Sections 7.1 and 7.3, respectively. Later the samples were re-implanted with 15 keV D with a dose of 10^{15} cm^{-2} . Consequently, a series of step-wise anneals was performed and after every step the free space related to the cavities was monitored with positron beam analysis. The *S* and *W* data were fitted with a model which contained 3 or 4 layers with the last layer describing the defect-free bulk. The boundaries for the layers with the irradiation defects, i.e. helium-vacancy clusters and cavities, were chosen to coincide with the damage profile predicted by TRIM. The evolution of the *S* - parameters for the damaged layer both in MgO and Si during the various

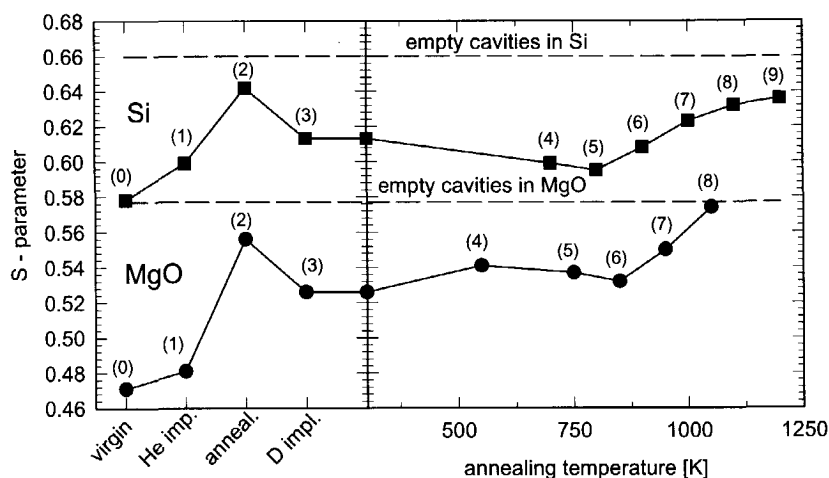


Fig. 7.12. Evolution of the S -parameter for the damaged layer during sample treatment. Dashed lines represent theoretical values of the S -parameter for empty cavities in Si and MgO.

sample treatments is shown in Fig. 7.12. Two horizontal dashed lines show the theoretically predicted values of the S -parameter for the empty cavities in MgO and Si. The values were obtained from the following considerations. It was found that high S -values measured for empty cavities are attributed to the formation of positronium (Ps), a hydrogen type “atom” in which the role of the proton is played by a positron. Positronium is formed in two states: short-lived (125 ps) para - Ps and long-lived (140 ns in vacuum) ortho - Ps. The probabilities for these states are 1/4 and 3/4, respectively. Para -Ps decays into two 511 keV photons which results in a high S -value restricted only by the detector resolution, i.e. $S_{para-Ps} \approx S_{res}$. Ortho-Ps interacts with the electrons of the cavity wall through the “pick-off” mechanism and its contribution to the S -parameter is close to the bulk value, i. e. $S_{ortho-Ps} \approx S_{bulk}$. Hence, the S value for an empty cavity can be estimated as follows:

$$S_{cav} = (1/4 S_{res} + 3/4 S_{bulk}), \quad (7.1)$$

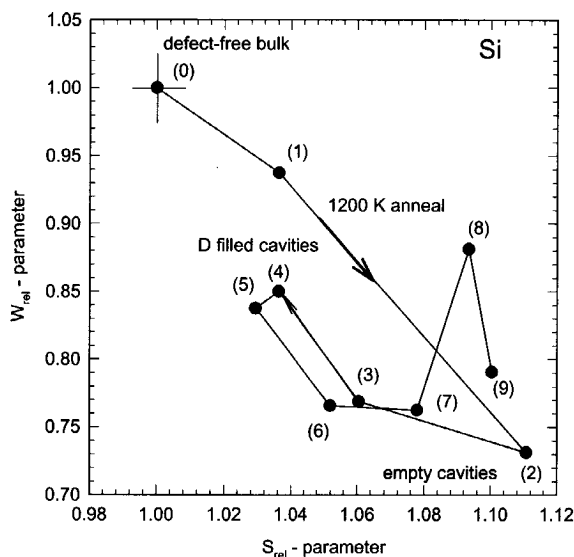


Fig. 7.13 S-W map showing evolution of the S and W parameters of the damaged layer for Si. The numbers of the symbols coincide with the numbers in Fig. 7.12

where $S_{res} = 0.9$ and S_{bulk} is taken from VEPFIT results obtained for the defect-free bulk, $S_{bulk} = 0.58$ for Si and $S_{bulk} = 0.47$ for MgO. However, the experimental curves for both materials lie lower than predicted. This may be caused by positrons annihilating directly without forming positronium, thus the contribution of S_{bulk} in Eq. 7.1 will increase, making the S_{cav} value lower.

After filling the cavities with D the S values for both Si and MgO decrease. In the right-hand part of Fig. 7.12 the S values of the damaged layer are plotted as a function of the annealing temperature. After the low, 550 - 700 K, temperature treatment small clusters containing deuterium dissociate and the released deuterium is retrapped at the cavities, resulting in a further decrease of S . At 900 K deuterium starts to escape from the cavities giving rise to an increase of the S - parameter. For both materials the initial value of S characteristic of empty cavities is restored at 1000-1100 K. Moreover, for MgO a further increase of S is observed. This effect is much more evident when the D

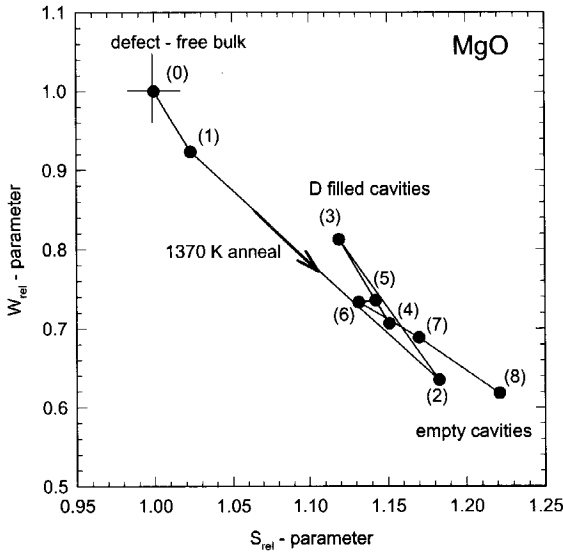


Fig. 7.14. *S*-*W* map showing evolution of the *S* and *W* parameters of the damaged layer for MgO. The numbers of the symbols coincide with the numbers in Fig. 7.12.

implantation dose was taken 4 times higher [Van Veen *et al.* 1998 E-MRS]. The similar behaviour of the *S* curves for Si and MgO during the annealing suggests that the permeation of D from cavities in MgO can be described by the same model used for Si [Van Veen 1991].

In Figs. 7.13 and 7.14 the history of *S* and *W* of the damaged layer are shown for Si and MgO, respectively. Note that this time the relative values, i.e. $S_{rel} = S/S_{bulk}$, $W_{rel} = W/W_{bulk}$, are plotted. In this case the (1,1) point for both plots located in the upper-left corner corresponds to the defect-free bulk material. The *S* and *W* values related to the open volume defects, e. g. cavities, are located in the opposite, bottom-right, corner. All the points are numbered in the same way as in Fig. 7.12. The trajectory defined by the experimental points evidently demonstrates that in both materials cavities were created after He implantation and annealing. Later they were filled with deuterium but during the subsequent anneals the cavities were completely restored.

Conclusions

1. A model accounting for the critical dose required to create nanocavities in Si is presented. The critical dose of 10^{16} cm^{-2} predicted by the model is in agreement with the experiment.
2. According to the model the cavities in Si are created during the annealing stage rather than during the implantation.
3. It is demonstrated that Si self-interstitials generated at the surface by 50 eV Ne irradiation fill cavities located at depths of 100-250 nm and reduce cavity size.
4. At Ne irradiation doses higher than 10^{19} cm^{-2} no effect of irradiation on cavity size is observed. Monte - Carlo modelling shows that the fraction of interstitials trapped by cavities is limited by the decreasing size of the cavities.
5. In the case of Kr a reduction of cavity size was not detected due to the trapping of interstitials by Kr-defects produced in the near surface layer.
6. Formation of nanosize cavities was observed in MgO after D or He high dose implantation followed by 1270 K annealing. The cavities in MgO appear to have a rectangular form.
7. The critical implantation dose for the formation of cavities in MgO is found to be 10^{16} cm^{-2} for ^3He .
8. The nanosize cavities in MgO and Si can be filled with deuterium by means of 15 keV D^+ implantation. During the subsequent annealing deuterium escapes from the cavities at 1000 K, leaving empty cavities behind.
9. In the case of MgO an increase of the cavity size was observed after D implantation.

APPENDIX A

Stationary diffusion equation

The solution of the boundary value problem 2.1-2.3 in the stationary form was described earlier by Van Veen *et. al.* [1990]. The solution method presented below is essentially the same but since the notation used in MODEX is different it is worth considering the most important equations again. By defining a set of intervals x_j , $j = 0, 1 \dots N$ as shown in Fig. 2.1, the equations 2.1-2.3 are transformed into a system of linear equations written for every layer j :

$$D_a \frac{d^2 C_j}{dx^2} + S_j - K_j C_j = 0. \quad (\text{A.1})$$

The boundary conditions at the nodes x_j for $j = 1 \dots N-1$ are:

$$C_j(x_j) = C_{j+1}(x_j) \quad (\text{A.2})$$

$$C'_j(x_j) = C'_{j+1}(x_j). \quad (\text{A.3})$$

For $j = 0$

$$C'_0 - \frac{1}{L_a} C_0 = 0 \quad (\text{A.4})$$

and for $j = N$

$$C'_N + \frac{1}{L_d} C_N = 0. \quad (\text{A.5})$$

The index α in this section will be omitted. The point defect source S_j and the trapping rate K_j are assumed to be constant within the layer j . The prime over C denotes the derivative $C'_j = dC_j/dx$ taken in the node x_j . The parameters L_a and L_d have the same meaning as in section 2.1. The fundamental solution of the Eq. A.1 has the following form [Boyce and Diprima 1986]:

$$C_j(x) = A_j e^{\lambda_j x} + B_j e^{-\lambda_j x} + \Omega_j \quad (\text{A.6})$$

with $\lambda_j = 1/L_{d,j} = (K_j/D)^{1/2}$, where $L_{d,j}$ is the diffusion length in the layer j , and A_j and B_j are the coefficients to be derived from the boundary conditions A.2-A.4; $\Omega_j = S_j/K_j$ is the nonhomogeneous term. Substitution of Eq. A.6 into the boundary conditions A.2-A.5 results in a system of $2N \times 2N$ algebraic linear equations for the coefficients A_j and B_j .

Another approach is to transform the $2N \times 2N$ matrix of equations into two independent $(N+1) \times (N+1)$ tridiagonal matrix equations. The tridiagonal matrix equations can be solved by elimination rather than by an iterative process. Therefore, the solution consumes very little memory and processor time. After making the substitutions $C_j = C_j(x_j)$ and $C'_j = C'_j(x_j)$ the matrix Eq. A.2 will split into two tridiagonal matrix equations:

for $j = 1 \dots N-1$:

$$C'_j(\lambda_{j+1}R_{j+1}^-R_j^+ + \lambda_jR_j^-R_{j+1}^+) - C'_{j-1}R_{j+1}^-\lambda_{j+1} - C'_{j+1}R_j^-\lambda_j = \lambda_j\lambda_{j+1}R_j^-R_{j+1}^-(\Omega_{j+1} - \Omega_j), \quad (\text{A.7})$$

$$C_j(\lambda_{j+1}R_{j+1}^+R_j^- + \lambda_jR_j^+R_{j+1}^-) - \lambda_jC_{j-1}R_{j+1}^- - \lambda_{j+1}C_{j+1}R_j^- = \lambda_j\Omega_jR_{j+1}^-(R_j^+ - 1) + \lambda_{j+1}\Omega_{j+1}R_j^-(R_{j+1}^+ - 1). \quad (\text{A.8})$$

For $j = 0$ and $j = N$:

$$C_0(\lambda_1R_1^+ + \frac{1}{L_a}R_1^-) - \lambda_1C_1 = \lambda_1\Omega_1(R_1^+ - 1), \quad (\text{A.9})$$

$$C_N(\lambda_NR_N^+ + \frac{1}{L_d}R_N^-) - \lambda_NC_{N-1} = \lambda_N\Omega_N(R_N^+ - 1), \quad (\text{A.10})$$

$$C'_0(R_1^+ + L_a\lambda_1R_1^-) - C'_1 = \lambda_1\Omega_1R_1^-, \quad (\text{A.11})$$

$$C'_N(R_N^+ + \lambda_NL_dR_N^- - C'_{N-1}) = -\lambda_N\Omega_NR_N^-, \quad (\text{A.12})$$

where

$$\begin{aligned} R_j^+ &= \cosh(\lambda_j(x_j - x_{j-1})) \\ R_j^- &= \sinh(\lambda_j(x_j - x_{j-1})). \end{aligned} \quad (\text{A.13})$$

The equations A.7 - A.12 form a complete set of equations for two tridiagonal matrixes, one for C_j and another for C'_j . The algorithm for the solution of a tridiagonal matrix equation is described in Press *et al.* [1989].

APPENDIX B

Non-stationary diffusion equation

To obtain the numerical solution of the non-stationary diffusion Eq. 2.1 the equation should be written in a finite difference form by substituting all the partial derivatives according to the following scheme [Press *et al.* 1989]:

$$\frac{\partial C}{\partial t} = \frac{C^{n+1} - C^n}{\delta t} \quad (\text{B.1})$$

$$\frac{\partial^2 C}{\partial x^2} = \frac{C_{j+1}^{n+1} - 2C_j^{n+1} + C_{j-1}^{n+1} + C_{j+1}^n - 2C_j^n + C_{j-1}^n}{2(x_{j+1} - x_j)(x_j - x_{j-1})}, \quad (\text{B.2})$$

where the upper index n denotes the time interval and the lower index j denotes the spatial interval. After making all the necessary substitutions Eq. 2.1 will take the following form:

$$C_j^{n+1} - C_j^n = \alpha_j (C_{j+1}^{n+1} - 2C_j^{n+1} + C_{j-1}^{n+1} + C_{j+1}^n - 2C_j^n + C_{j-1}^n) + S_j \Delta t - \beta_j (C_j^{n+1} + C_j^n), \quad (\text{B.3})$$

where

$$\alpha_j = \frac{D\delta t}{2(x_{j+1} - x_j)(x_j - x_{j-1})}, \quad (\text{B.4})$$

$$\beta_j = \frac{K_j \delta t}{2} \quad (\text{B.5})$$

and S_j and K_j have the same meaning as in Eq. A.1. After simplification the following tridiagonal matrix is obtained:

$$\begin{aligned} -\alpha_j C_{j+1}^{n+1} + C_j^{n+1}(1 + 2\alpha_j + \beta_j) - \alpha_j C_{j-1}^{n+1} = \\ \alpha_j C_{j+1}^n + C_j^n(1 - 2\alpha_j - \beta_j) + \alpha_j C_{j-1}^n + S_j \cdot \delta t. \end{aligned} \quad (\text{B.6})$$

Equation B.6 is defined for the intervals $j=1 \dots N-1$. For the external boundaries $j = 0$ and $j = N$ the boundary conditions 2.5 and 2.6 are used:

$$C_0^{n+1} \left(1 + \frac{L_a}{x_1 - x_0}\right) - \frac{L_a}{x_1 - x_0} C_1^{n+1} = -C_0^n \left(1 + \frac{L_a}{x_1 - x_0}\right) + C_1^n \frac{L_a}{x_1 - x_0}, \quad (\text{B.7})$$

$$C_N^{n+1} \left(1 + \frac{x_N - x_{N-1}}{L_d}\right) - C_{N-1}^{n+1} = -C_N^n \left(1 + \frac{x_N - x_{N-1}}{L_d}\right) + C_{N-1}^n. \quad (\text{B.8})$$

The equations B.6-B.8 form a complete set of matrix equations for evaluating the concentration C_j^{n+1} at time t_{n+1} from the concentrations C_j^n at time t_n . The time step $\delta t = t_{n+1} - t_n$ is much less than the time step Δt used in the program's main loop in Eq. 2.11. The time step δt is kept within the limit: $\delta t < \Delta x^2/D$, where Δx is the minimum layer width and D is the diffusion coefficient. This relation defines the stability of the finite element scheme B.1-B.2 [Press *et al.* 1989].

APPENDIX C

Groups of clusters

So far it was assumed that the cluster structure is characterised by the four-dimensional index $\beta = (n, m, l, k)$, where n , m , l , and k are the number of vacancies, helium atoms, impurities and self-interstitials, respectively. In practice, however, clusters with similar structures can be grouped together so that the whole group is described by one set of parameters. For example, group $V_{4-6}He_{2-3}$ denotes all the clusters containing from 4 to 6 vacancies and from 2 to 3 helium atoms. Index β in this case should be treated as $\beta = (n_{min} - n_{max}; m_{min} - m_{max}; l_{min} - l_{max}; k_{min} - k_{max})$, where n_{min} , n_{max} , m_{min} , m_{max} , l_{min} , l_{max} , k_{min} , k_{max} are the boundary values for the numbers of vacancies, helium atoms, impurities and self-interstitials, respectively. Introduction of groups leads to a new type of reaction: a cluster can trap or dissociate a point defect without transition to the other group. For example, the cluster group V_{4-6} after trapping a vacancy can form a cluster from the next group: $V_{4-6} + V \rightarrow V_7$. The actual reaction in this case is $V_6 + V \rightarrow V_7$. Two other possible reactions, i.e. $V_4 + V \rightarrow V_5$ and $V_5 + V \rightarrow V_6$ form a cluster which belongs to the same group: $V_{4-6} + V \rightarrow V_{4-6}$. In the further discussion reactions which lead to transitions between groups will be called *external* and reactions which take

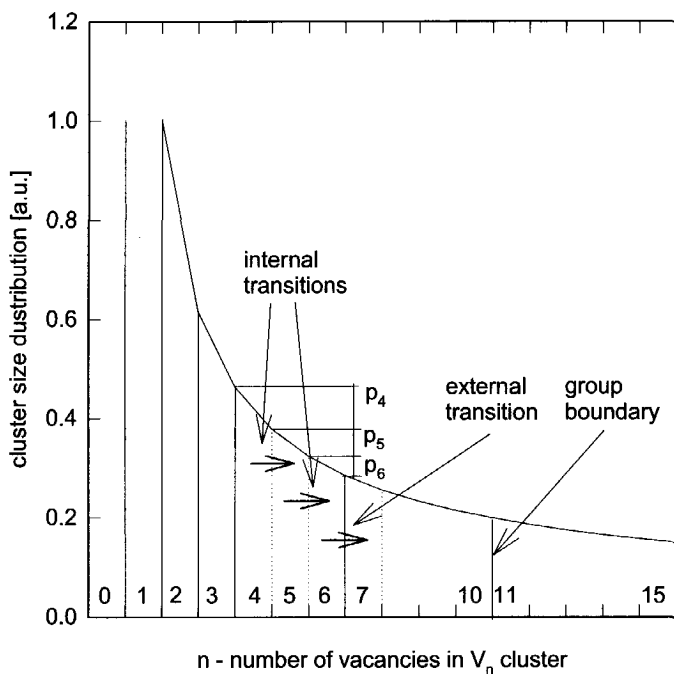


Fig. C1. Illustration of internal and external transitions in the case of vacancy trapping at V_n - vacancy cluster.

place within one group will be called *internal*. In Fig. C-1 both types of reactions are demonstrated.

According to Eq. 2.9 the rate equations for three successive types of clusters V_4 , V_5 and V_6 will look as follows (only one type of point defect is considered, e. g. $\alpha = V$) :

$$\begin{aligned} \frac{dC_4}{dt} &= Z_3 C_3 C_V - Z_4 C_4 C_V + C_5 Q_5 - C_4 Q_4, \\ \frac{dC_5}{dt} &= Z_4 C_4 C_V - Z_5 C_5 C_V + C_6 Q_6 - C_5 Q_5, \\ \frac{dC_6}{dt} &= Z_5 C_5 C_V - Z_6 C_6 C_V + C_7 Q_7 - C_6 Q_6. \end{aligned} \quad (C.1)$$

After forming one group C_{4-6} the reactions will yield:

$$\frac{dC_{4-6}}{dt} = \frac{dC_4}{dt} + \frac{dC_5}{dt} + \frac{dC_6}{dt} = Z_3 C_3 C_V - Z_6 C_6 C_V + C_7 Q_7 - C_4 Q_4. \quad (C.2)$$

Since all the trapping and dissociation parameters are assumed to be the same for all clusters within the group, Eq. C.2 will take the following form:

$$\frac{dC_{4-6}}{dt} = Z_3 C_3 C_V - p_6 Z_{4-6} C_{4-6} C_V + C_7 Q_7 - p_4 C_{4-6} Q_{4-6}, \quad (C.3)$$

where Z_{4-6} is the mean group sink strength, Q_{4-6} is the mean group dissociation rate and p_6 and p_4 are the probabilities for external trapping and external dissociation reactions, respectively. The choice between the external and internal reactions depends on the cluster distribution within the group which is unknown. A straightforward approach is to assume that all the clusters are equally represented. In this case the reactions $V_{4-6} + V \rightarrow V_7$ and $V_{4-6} + V \rightarrow V_{4-6}$ are realised with probabilities of 1/3 and 2/3, respectively. However, this approach is not correct. For the cluster distribution shown in Fig. C.1 the real probability of the external reaction for V_{6-10} , p_6 , is lower than 1/3, obtained from the even distribution. In order to provide the information necessary to reconstruct the cluster distribution one has to keep track of all the point defects, i.e. vacancies, helium atoms etc., which are accumulated inside the group during the trapping reactions or leave the group during the dissociation reactions. If these numbers are available then, for example, the total number of vacancies inside the group divided by the group population provides the mean value of vacancies for the cluster distribution. However, information about higher momenta of this distribution is not available and should be introduced from other considerations at hand. Currently, the cluster distribution inside the group is described by a Gaussian:

$$p_n = \frac{1}{\sqrt{2\pi}\sigma} e^{-\frac{(n-\eta)^2}{2\sigma^2}} \quad (C.4)$$

where $\eta = N_\alpha/N$ and $\sigma = 0.05 N_\alpha$ with N_α and N being the total number of point defects of type α in the group and the cluster population, respectively. If the cluster distribution is known, the group dissociation rate S_α and the group trapping rate $K_{\alpha\beta}$ can be written as follows:

external trapping :

$$K_{\alpha\beta}^e = p_{\max} 4\pi R_{\alpha\beta} D_\alpha \frac{N_\beta \rho}{\Delta x}, \quad (\text{C.5})$$

internal trapping:

$$K_{\alpha\beta}^i = (1 - p_{\max}) 4\pi R_{\alpha\beta} D_\alpha \frac{N_\beta \rho}{\Delta x}, \quad (\text{C.6})$$

external dissociation:

$$S_{\alpha\beta}^e = p_{\min} \frac{N_\beta \rho}{\Delta x} v n_\alpha e^{-\frac{E^d}{kT}}, \quad (\text{C.7})$$

internal dissociation:

$$S_{\alpha\beta}^i = (1 - p_{\min}) \frac{N_\beta \rho}{\Delta x} v n_\alpha e^{-\frac{E^d}{kT}}, \quad (\text{C.8})$$

where p_{\max} and p_{\min} are the probabilities required to obtain the group boundary cluster structures. Evidently, only external trapping and dissociation rates are involved in the set of rate equations 2.9 describing transitions between different groups. However, internal trapping and dissociation rates have an effect on the point defect concentration C_α and should be considered while constructing the point defect source Eq. 2.5 and the trapping term Eq. 2.7 for diffusion equation 2.1.

APPENDIX D

Trapping at unstable sinks

Trapping of point defects at a stable sink of type β is described by $K_{\alpha\beta}C_{\alpha}$, where $K_{\alpha\beta}$ is the group trapping rate defined by Eqs. C.5 and C.6. If the sink is not stable there is a flow of point defects dissociating from the sink in the opposite direction, which is described by $S_{\alpha\beta'}$ (Eqs. C.7 and C.8). Note that the trapping and dissociation rates are attributed to different types of clusters β and β' , related by $\alpha + \beta \rightarrow \beta'$. As an illustration, consider the rate equation 2.9 written for a V_5 -vacancy cluster:

$$\frac{dC_5}{dt} = K_4^e C_V - S_5^e - K_5^e C_V + S_6^e, \quad (D.1)$$

where K_4^e and K_5^e are external trapping rates of groups V_4 and V_5 (Eq. C.5), S_5^e and S_6^e are external dissociation rates of groups V_5 and V_6 and C_V is the vacancy bulk concentration. In this example the terms $K_5^e C_V$ and S_6^e describe external reactions between the groups V_5 and V_6 described by Eqs. C.5 and C.7, respectively. If these last two terms are not equal to zero, they can be compensated by subtraction of an arbitrary value provided this value is the same for both terms. This procedure does not change the

left-hand side of Eq. D.1. The actual value of this compensation depends on the type of the reaction and will be considered separately. All possible cases are reviewed below:

1) *internal trapping*: $\alpha + \beta \rightarrow \beta'$; *dominant trapping*: $K_{\alpha\beta}^i C_\alpha > \gamma S_{\alpha\beta}^i$,

where γ is a compensation parameter, $0 < \gamma < 1$. The choice for γ will be discussed below. In the case of dominant trapping the compensated values for the trapping rate and dissociation rate are calculated as follows:

$$\begin{aligned} K_{\alpha\beta}^{i,c} &= K_{\alpha\beta}^i - \gamma S_{\alpha\beta}^i / C_\alpha \\ S_{\alpha\beta}^{i,c} &= S_{\alpha\beta}^i (1 - \gamma), \end{aligned} \quad (D.2)$$

dominant dissociation: $K_{\alpha\beta}^i C_\alpha < \gamma S_{\alpha\beta}^i$

In this case retrapping is negligible and the compensation values for dissociation and trapping rates are defined as follows:

$$\begin{aligned} K_{\alpha\beta}^{i,c} &= 0 \\ S_{\alpha\beta}^{i,c} &= S_{\alpha\beta}^i - K_{\alpha\beta}^i C_\alpha, \end{aligned} \quad (D.3)$$

2) *external trapping*: $\alpha + \beta \rightarrow \beta'$,

Two different situations are possible depending on whether the final group is present in the cluster list or not:

final group is present; *dominant trapping*: $K_{\alpha\beta}^e C_\alpha > \gamma S_{\alpha\beta}^e$

$$\begin{aligned} K_{\alpha\beta}^{e,c} &= K_{\alpha\beta}^e - \gamma S_{\alpha\beta}^e / C_\alpha \\ S_{\alpha\beta}^{e,c} &= S_{\alpha\beta}^e (1 - \gamma), \end{aligned} \quad (D.4)$$

final group is present; *dominant dissociation*: $K_{\alpha\beta}^e C_\alpha < \gamma S_{\alpha\beta}^e$

$$\begin{aligned}
 K_{\alpha\beta}^{e,c} &= 0 \\
 S_{\alpha\beta'}^{e,c} &= S_{\alpha\beta'}^e - K_{\alpha\beta}^e C_\alpha,
 \end{aligned}
 \tag{D.5}$$

3) *external trapping, final group is not present: $\alpha + \beta \rightarrow \beta'$, $N_{\beta'} = 0$.*

The dissociation rate of the non-existing group β' can be estimated by setting $N_{\beta'}$ to unity: $N_{\beta'} = 1$. Then the external dissociation rate will be:

$$S_{\alpha\beta'}^e = p_{\min} \frac{\rho}{\Delta x} v n_\alpha e^{-\frac{E^d}{kT}}. \tag{D.6}$$

For dominant trapping ($K_{\alpha\beta}^e C_\alpha > \gamma S_{\alpha\beta'}^e$) no changes for $K_{\alpha\beta}^e$ are needed. Dominant dissociation actually means that the final group is unstable and therefore $K_{\alpha\beta}^{e,c} = 0$.

The compensation parameter γ defines the “softness” of the compensation. High values of γ can lead to undesirable oscillations in the solution because of the feedback between the dissociation rate and the trapping rate: the reduction of the dissociation rate $S_{\alpha\beta}$ (see Eqs. D.3 or D.5) causes a reduction of the point defect concentration C_α which in turn reduces the trapping term $K_{\alpha\beta} C_\alpha$. Consequently, the compensation term $K_{\alpha\beta} C_\alpha$ decreases causing an increase in $S_{\alpha\beta}$. This “out of phase” feedback can be eliminated by choosing $\gamma \approx 0.25-0.5$.

SUMMARY

The present study investigates the clustering of point defects during ion implantation and annealing. Historically, the effects of point defect clustering were first encountered in materials used in the nuclear power industry. Materials were seen to exhibit anomalous swelling after irradiation to atomic displacement levels of one or more displacement per atom. However, point defects on themselves seldom lead to the formation of three-dimensional clusters and therefore to swelling. Gases produced in (n,α) and (n,p) nuclear reactions are known to stabilize the three dimensional growth mode of vacancy clusters during the nucleation phase. In future fusion reactors these effects are expected to be even more severe due to the expected higher fluxes of fast neutrons. Besides the occurrence of point defect clustering in materials with a nuclear application the advent of new material deposition techniques and implantation techniques in the semiconductor industry has caused a tremendous increase in defect studies. It is of interest to note that defect clusters are not always considered to be harmful to the operation of the device. Defect engineering has become a tool in achieving the device properties one wants.

In the present thesis a theoretical and experimental study on the clustering of point defects produced by ion implantation is presented. In Chapter 2 the computer program MODEX developed in this study aimed at simulating the evolution of point defect clusters during ion implantation and subsequent annealing is described. The new and unique feature of this program is the ability to handle both stationary and non-stationary diffusion of up to four different mobile point defects. Besides that, instead of solving the appropriate rate equations by conventionally used numeric methods, the program uses a Monte-Carlo algorithm which provides high efficiency and flexibility in choosing the physical model underlying the set of rate equations. By comparing the

simulation results to the experimental data various defect evolution models can be tested and optimized.

Various experimental techniques were used in this study: Thermal Helium Desorption Spectrometry (THDS), Positron Beam Analysis (PBA) and Neutron Depth Profiling (NDP). A detailed description of the THDS technique is presented in Chapter 3. This chapter also describes a number of computer codes developed to conduct the THDS experiment and to process the experimental data.

Experimental studies on irradiation effects are presented in Chapters 4 through 7. They deal with the evolution of defects created by ion implantation in a wide range of materials including metals, semiconductors and insulators. In Chapter 4 helium traps and their thermal stability in vanadium and vanadium based alloys are investigated. Vanadium based alloys, particularly V-4Cr-4Ti are considered as an alternative to conventionally used austenitic and ferritic steels for the structural components of a fusion reactor because of their low activation and high radiation resistance. The present study has revealed the presence of two types of helium traps: $\text{He}_n\text{V}_m\text{X}$ clusters which are formed during He ion implantation and pre-existing traps. The latter are observed only in the alloys. Further, the thermal stability of these helium traps was investigated.

In Chapter 5 a Thermal Desorption Spectrometry study on deuterium retention in beryllium containing helium bubbles is presented. Beryllium is used as a plasma facing material and a neutron multiplier in the present concept of ITER (International Thermal Experimental Reactor). This study has confirmed that deuterium has a low retention in beryllium and is released below 800 K. However, small helium bubbles produced in beryllium due to nuclear reactions account for a strong trapping of deuterium with a dissociation energy of $E^{diss} > 2.7$ eV.

In Chapter 6 lithium containing ceramics are considered. These materials are to be used as the tritium breeder blanket for a fusion reactor. In this study an analytical model describing tritium production and retention in Li_4SiO_4 is presented. The model accounts

for the recombination of tritium at the surface of the grains. Two limiting cases of tritium release are discussed: first, release limited by bulk diffusion and secondly, release limited by recombination at the surface. Comparison of the model to the experimental results allowed to derive a number of important parameters including the diffusion coefficient of tritium in Li_4SiO_4 .

Among the materials of interest for microelectronics and nanotechnology two materials were studied in the present work: Si and MgO are considered in Chapter 7. In both materials the formation and stability of nanosize cavities was investigated. Gettering of impurities on the wall of the cavities in Si is recently proposed as a promising way to purify the Si matrix. Nanocavities in MgO can be used as nucleation centers for metal nanoclusters which are known to change optical properties. By computer simulations carried out with the code MODEX an explanation for the critical implantation dose necessary to form nanocavities has been found. It was shown that the formation of the nanocavities takes place during the annealing stage, which follows the implantation stage. The stability of the cavities in Si was studied by filling the cavities with self-interstitials. The interstitials were generated at the surface by Ne bombardment. In another set of experiments permeation of deuterium from nanocavities in Si and MgO was studied. It was shown that deuterium dissociates from the cavities at 900-1000 K in both materials.

In short, the growth of defect clusters by agglomeration of point defects and their dissociation behavior has been studied. Important detailed insight in the mechanisms has been obtained by a combination of experimental studies and computer simulations carried out with the program MODEX.

SAMENVATTING

In deze studie wordt de clustering van puntdefecten tijdens ionenimplantatie en verhitting onderzocht. Historisch werden de effecten van clustering van puntdefecten voor het eerst waargenomen in materialen die gebruikt werden voor de opwekking van nucleaire energie. Materialen vertoonden ongewone zwellings na bestraling tot atomaire verplaatsingsniveaus van één of meer verplaatsingen per atoom. Puntdefecten zelf leiden echter zelden tot het ontstaan van driedimensionale clusters en dus tot zwellings. Het is bekend dat gassen die worden geproduceerd in (n,α) en (n,p) nucleaire reacties de driedimensionale groei van vacatureclusters stabiliseren tijdens de nucleatiefase. Naar verwachting zijn deze effecten nog sterker in toekomstige fusiereactoren vanwege de verwachte hogere flux van snelle neutronen. Naast het voorkomen van clustering van puntdefecten in materialen met een kernfysische toepassing, heeft het vooruitzicht van nieuwe materiaaldepositietechnieken en implantatietechnieken in de halfgeleiderindustrie een geweldige toename veroorzaakt van defectstudies. Het is van belang op te merken dat defectclusters niet altijd als schadelijk worden beschouwd voor het functioneren van het halfgeleider-element. 'Defect engineering' is een instrument geworden om tot gewilde eigenschappen van het element te komen.

In dit proefschrift wordt een theoretische en experimentele studie gepresenteerd van het clusteren van puntdefecten geproduceerd door ionenimplantatie. In Hoofdstuk 2 wordt het computerprogramma MODEX beschreven dat in deze studie is ontwikkeld en gericht is op het simuleren van de evolutie van clusters van puntdefecten tijdens ionenimplantatie en volgtijdelijke verhitting. De nieuwe en unieke eigenschap van dit programma is de mogelijkheid tot simulatie van zowel stationaire als niet-stationaire diffusie van maximaal vier verschillende mobiele puntdefecten. In plaats van de van toepassing zijnde 'rate equations' op te lossen met conventionele numerieke methodes,

gebruikt het programma een Monte-Carlo algoritme dat een hoge efficiëntie en flexibiliteit biedt in het kiezen van het fysisch model dat ten grondslag ligt aan het stelsel van 'rate equations'. Door de simulatie-resultaten te vergelijken met de experimentele gegevens, kunnen diverse modellen voor de evolutie van defecten worden getest en geoptimaliseerd.

Verscheidene experimentele technieken werden in deze studie gebruikt: Thermal Helium Desorption Spectrometry (THDS), Positron Beam Analysis (PBA) and Neutron Depth Profiling (NDP). Een gedetailleerde beschrijving van de THDS techniek wordt gepresenteerd in Hoofdstuk 3. Dit hoofdstuk beschrijft ook een aantal computercodes die ontwikkeld zijn om het THDS experiment te begeleiden en de experimentele gegevens te verwerken.

Experimentele studies betreffende effecten van bestralingen worden gepresenteerd in de Hoofdstukken 4 tot en met 7. Ze behandelen de evolutie van defecten die gecreëerd zijn door ionenimplantatie in een breed scala van materialen, inclusief metalen, halfgeleiders en isolatoren. In Hoofdstuk 4 worden helium 'traps' (vangst platen) en hun thermische stabiliteit in vanadium en vanadiumlegeringen onderzocht. Vanadium- legeringen, voornamelijk V-4Cr-4Ti, worden beschouwd als een alternatief voor conventioneel gebruikte austenitisch en ferritisch staal voor de structurele componenten van een fusiereactor vanwege hun lage activatie en hoge stralingsweerstand. De huidige studie heeft twee types van traps voor helium aangetoond: $\text{He}_n\text{V}_m\text{X}$ clusters die worden gevormd tijdens helium-ionenimplantatie en de traps die al voor de implantatie aanwezig waren. De laatste worden alleen in de legeringen waargenomen. Tenslotte is de thermische stabiliteit van deze helium traps onderzocht.

In Hoofdstuk 5 wordt een TDS (Thermal Desorption Spectroscopy) studie naar deuteriumretentie in beryllium met heliumbellen gepresenteerd. Beryllium wordt gebruikt als een 'plasma facing material' en als een neutronenvermenigvuldiger binnen het huidige concept van ITER (International Thermal Experimental Reactor). Deze studie heeft bevestigd dat deuterium een lage retentie heeft in beryllium en vrijkomt op een

temperatuur lager dan 800 K. Kleine heliumbellen die in beryllium ontstaan ten gevolge van nucleaire reacties zorgen echter voor een sterke trapping van deuterium met een dissociatie energie van $E^{diss} > 2.7$ eV.

In Hoofdstuk 6 worden lithiumbevattende keramische materialen beschouwd. Deze materialen zullen worden gebruikt als de 'tritium breeder blanket' voor een fusie-reactor. In deze studie wordt een analytisch model gepresenteerd dat tritiumproductie en -retentie in Li_4SiO_4 beschrijft. Het model houdt rekening met de recombinitie van tritium aan het oppervlak van de korrels. Twee extreme gevallen van het vrijkomen van tritium worden besproken: ten eerste vrijkomen van tritium gelimiteerd door bulkdiffusie en ten tweede gelimiteerd door recombinitie aan het oppervlak. Uit vergelijking van het model met de experimentele resultaten valt een aantal belangrijke parameters af te leiden, inclusief de diffusiecoëfficiënt van tritium in Li_4SiO_4 .

Onder de materialen die van toepassing zijn voor de micro-electronica en de nanotechnologie worden twee materialen bestudeerd in dit werk: Si en MgO worden behandeld in Hoofdstuk 7. In beide materialen worden de formatie en stabiliteit van holten met nanometer-afmetingen (nanoholten) onderzocht. Zogenaamde 'gettering' van onzuiverheden aan de wand van de cavities in Si is recentelijk voorgesteld als een veelbelovende manier om de Si matrix te zuiveren. Nanoholten in MgO kunnen worden gebruikt als nucleatiecentra voor metalen nanoclusters, waarvan bekend is dat zij optische eigenschappen veranderen. Met computersimulaties uitgevoerd met de MODEX code werd een verklaring gevonden voor de kritische implantatiedosis die vereist is voor de vorming van nanoholten. Verder werd aangetoond dat de formatie van de nanoholten plaatsvindt tijdens de verhittingsstap, die op de implantatiestap volgt. De stabiliteit van de holten in Si werd bestudeerd door de holten te vullen met zelf-interstitiëlen. De interstitiëlen werden aan het oppervlak gegenereerd door een bombardement van Ne ionen. In een andere reeks experimenten werd permeatie van deuterium van nanoholten in Si en MgO bestudeerd. Er werd aangetoond dat deuterium dissocieert uit de holten op een temperatuur van 900-1000 K in beide materialen.

Samenvattend is de groei van defectclusters door agglomeratie van puntdefecten alsmede hun dissociatiegedrag onderzocht. Belangrijk gedetailleerd inzicht in deze mechanismen is verkregen door combinatie van experimentele studies en computer-simulaties uitgevoerd met het programma MODEX.

REFERENCES

- [Adams and Wolfer 1989] J. B. Adams and W. G. Wolfer, J. of Nucl. Mater. **166**, (1989) 235–242.
- [Adams and Foiles 1990] J. B. Adams and S. M. Foiles, Phys. Rev. B **41** (1990) 3316–3328.
- [Adams *et al.* 1994] J. B. Adams, A. Rockett, J. Kieffer, W. Xu, M. Nomura, K.A. Kilian, D.F. Richards, R. Ramprasad, J. of Nucl. Mater. **216** (1994) 265 – 274.
- [Bacon and de la Rubia, 1994] D. J. Bacon, T. D de la Rubia, J. of Nucl. Mater. **216** (1994) 275–290.
- [Bakker *et al.* 1998] K. Bakker, R. Conrad, J. G. van der Laan M. P. and Stijkel, Proceedings CBBI-7, NRG Report 21099/99.23482, Petten, February 1999, 6/29-38, 4-27
- [Baskes *et al.* 1989] M. I. Baskes, J. S. Nelson and A. F. Wright, Phys. Rev. B **40** (9) (1989) 6085-6100.
- [Borodin 1994] V. A. Borodin, Physica A, **211** (1994) 279-316.
- [Boyce and Diprima 1986] W. E. Boyce, R. C. Diprima, *Elementary Differential Equations and Boundary Value Problems*, John Wiley & Sons, New York 1986.
- [Brailsford and Bullough 1972] A. D. Brailsford and R. Bullough, J. of Nucl. Mater. **44** (1972) 121.
- [Bruel 1998] M. Bruel, MRS Bulletin, **23** no.12, (1998) 35.
- [Chakraborty 1998] P. Chakraborty, J. of Materials Science **33** (1998) 2235-2249.
- [Chernikov *et al.* 1998] V. N. Chernikov, H. Ullmaier, A. P. Zakharov, J. of Nucl. Mater. **258-263 A**, (1998) 694-699.
- [Chung and Smith 1992] H. M. Chung and D. L. Smith, J. of Nucl. Mater. **191-194**, (1992) 942-947.

[Chung *et al.* 1996] H. M. Chung, B. A. Loomis, D. L. Smith, J. of Nucl. Mater. **233-237** (1996) 446-475.

[Chung *et al.* 1996, Vanadium Workshop] H. M. Chung, B. A. Loomis, J. Gazda, D. L. Smith, Procc. 2nd Workshop on Vanadium Alloy Development for Fusion, Edited by E. V. van Osch, 20-22 May, 1996, 39.

[Cocuaud *et al.* 1997] N. Cocuaud, E. Picard, R. J. Koning M., A. Conti, H. Matzke, Proceedings Global 97, (1997) 1044.

[Crawford 1984] J. H. Crawford Jr, Nucl. Inst. and Methods in Phys. Res. **B1** (1984) 159-165.

[De la Rubia 1996] T. de la Rubia, Ann. Rev. Mater. Sci. **26** (1996) 613.

[Eleveld *et al.* 1994] H. Eleveld, A. van Veen, M. Clement and M. de Moor, Plasma Devices and Operations, **3** (1994) 65-78.

[Eleveld *et al.* 1994 J. Nucl Mater] H. Eleveld, A. van Veen, F. Labohm and M. W. de Moor, J. of Nucl. Mater. **212-215** (1994) 971-975.

[Eleveld 1996] H. Eleveld, *Hydrogen and helium in selected fusion reactor materials*, PhD. Thesis (1996), Delft University of Technology, The Netherlands.

[Evans *et al.* 1987] J. H. Evans, A. van Veen and C. C. Griffioen, Nucl. Instr. and Meth. in Phys. Res. **B 28** (1987) 360-363.

[Fedorov *et al.* 1996] A. V. Fedorov, G. P. Buitenhuis, A. van Veen, A. I. Ryazanov, J. H. Evans, W. van Witzenburg, K. T. Westerduin, J. of Nucl. Mat., **227** (1996) 312-321.

[Fedorov *et al.* 1996, ICFRM] A. V. Fedorov, A. van Veen, A. I. Ryazanov, J. of Nucl. Mat. **233-237** (1996) 385-389.

[Fedorov *et al.* 1997, MRS] A. V. Fedorov, A. van Veen and J. Th. de Hosson, MRS Meeting 1996. Mat. Res. Soc. Symp. Proc., Editors I. M. Robertson, G. S. Was, L. W. Hobbs, T. D. de la Rubia, Vol. **439** (1997) 383-388.

- [Fedorov *et al.* 1997, Mito] A. V. Fedorov, A. van Veen A., G. J. Busker, Proc. of the 3rd IAE International Workshop on Beryllium Technology for Fusion, October 22-24, 1997, Mito City, Japan, Eds. H. Kawamura and M. Okamoto, 152-157.
- [Fedorov and van Veen 1998] A. V. Fedorov and A. van Veen, Computational Materials Science **9** (1998) 309-324.
- [Fedorov *et al.* 1998, ICFRM] A. V. Fedorov, A. van Veen , A. I. Ryazanov, J. Nucl. Mater., **258-263** (1998) 1396-1399.
- [Fedorov *et al.* 1998, CBBI] A. V. Fedorov, A. van Veen, K. Bakker J. G. van der Laan, Proceedings CBBI-7, NRG Report 21099/99.23482, Petten, February 1999, 6/29-38, 6-33
- [Fedorov *et al.* 1999, IBMM] A. V. Fedorov, A. van Veen, H. Schut, A. Rivera, Nuclear Instr. and Methods in Phys. Res. Sect. B **148** 1-4 (1999) 289-293.
- [Fedorov *et al.* 1999, MRS] A. V. Fedorov, A. van Veen, H. Schut, MRS Meeting 1999, Mat. Res. Soc. Proc. Editors S. J. Zinkle, G. E. Lucas, R. C. Ewing, J. S. Williams, Vol. **540** (1999) 231-236.
- [Follstaedt *et al.* 1996] D. M. Follstaedt, S. M. Myers, G. A. Petersen and J. W. Medernach, J. of Electronic Materials, **25**(1) (1996) 151-164.
- [Freund *et al.* 1982] F. Freund, H. Wengeler and R. Martens, Geochimica et Cosmochimica Acta, **46** (1982) 1821-1829.
- [Fukumoto *et al.* 1998] K. Fukumoto, H. Matsui, A. Kimura, **258-263** (1998) 1431-1436
- [Gelles *et al.* 1994] D. S. Gelles, G. A. Sernayev, M. Dalle Donne, H. Kawamura, J. of Nucl. Mater. **212-215** (1994) 29-38.
- [Greuter *et al.* 1994] M. J. W. Greuter, L. Niesen, A. van Veen and J.^{*}H. Evans, Philosophical Magazine Letters, **70** (4) (1994) 241-245.
- [Griffioen *et al.* 1987] C. C. Griffioen, J. H. Evans, P. C. de Jong and van A. Veen, Nuclear Instr. and Methods in Phys. Res. Sect.B, **27** (1987) 417.
- [Harrod and Gold 1980] D. L. Harrod and R. E. Gold, Intern. Metals Rev., **4** (1980) 163

[Izumi 1998] K. Izumi, MRS Bulletin, **23**, no.12 (1998) 20.

[Kawamura *et al.* 1990] H. Kawamura, E. Ishituka, A. Sagara, K. Kamada, H. Nakata, M. Saito and Y. Hutamura, J. of Nucl. Mater. **176&177** (1990) 661-665.

[King *et al.* 1996] J. F. King, M. L. Grossbeck, G. M. Goodwin, R. Strain, Chung, H. Gazda J., J. Park, Procc. 2nd Workshop on Vanadium Alloy Development for Fusion, Edited by E. V. van Osch, 20-22 May, (1996) 32.

[Kooi *et al.* 2000] B. J. Kooi, A. van Veen, J. Th. M. De Hosson, H. Schut, A. V. Fedorov and F. Labohm, Appl. Phys. Lett., **76**, 9 (2000) 1110-1112.

[Kotomin and Popov 1998] E. A. Kotomin, A. I. Popov, Nucl. Inst. and Methods in Phys. Res. Sect B **141** (1998) 1.

[Kwast *et al.* 1995] H. Kwast, M. Stijkel, R. Muis, R. Conrad, EXOTIC: Development of ceramic tritium breeding materials for fusion reactor blankets, ECN-C-95-123 (1995).

[Lewis 1988] M. B. Lewis, J. of Nucl. Mater. **152** (1988) 114-122.

[Lossev and Kuppers 1992] V. Lossev and J. Kuppers, J. of Nucl. Mater. **196-198**, (1992) 953-957.

[Mansur and Coghlan 1983] L. K. Mansur, W. A. Coghlan, J. of Nucl. Mater. **119** (1983) 1-25.

[Mansur 1994] L. K. Mansur, J. of Nucl. Mater. **216** (1994) 97-123.

[Markin *et al.* 1996] A. V. Markin, V. N. Chernikov, S. Yu. Rybakov, A. P. Zakharov, J. of Nucl. Mater. **233-237** (1996) 865-869.

[Matera and Federici 1996] R. Matera, R. Federici, J. of Nucl. Mater. **233-237** (1996) 17-25.

[Matsui *et al.* 1992] H. Matsui, M. Tanaka, M. Yamamoto and M. Tada., J. of Nucl. Mater. **191-194** (1992) 919-923.

[Matsui *et al.* 1996] H. Matsui, K. Fukumoto, D. L. Smith, Hee M. Chung, W. van Witenburg, S. N. Votiviv, J. of Nucl. Mater **233-237** (1996) 92-99.

- [**Matsui 1996, Vanadium Workshop**] H. Matsui, Procc. 2nd Workshop on Vanadium Alloy Development for Fusion, Edited by E. V. van Osch, 20-22 May (1996) 36.
- [**Mattas and Billone 1996**] R. F. Mattas and M. C. Billone, J. of Nucl. Mater. **233-237** (1996) 72.
- [**Myers et al. 1998**] S. M. Myers, G. A. Petersen, D. M. Follstaedt, C. H. Seager, T. J. Headley and J. R. Michael, Electrochemical Society Proc., **98-1** (1998) 1150-1161.
- [**Myers et al. 1996**] S. M. Myers, G. A. Petersen and C. H. Seager, J. Appl. Phys., **80** (7) (1996) 3717-3726.
- [**Mills et al. 1980**] R. L. Mills, D. H. Liebenberg and J. C. Bronson, Phys. Rev. B **21** (1980) 5137-5148.
- [**Nakajima et al. 1993**] H. Nakajima, S. Nagata, H. Matsui and S. Yamaguchi, Philosophical Mag. A **67** (3) (1993) 557-571.
- [**Neeft et al. 1998**] E. A. C. Neeft, R. J. M. Konings, A. van Veen, H. Schut, A.V. Fedorov., In Proceedings of the World Ceramics Congress and Forum on New Materials, VIII, CIMTEC- 98, (1998) 531-539.
- [**Press et al. 1989**] W. H. Press, B. P. Flannery, S. A. Teukolsky, W.T. Vetterling, *Numerical Recipes in Pascal*, Cambridge University Press 1989.
- [**Peterson et al. 1997**] G. A. Peterson, S. M. Myers, D. M. Follstaedt, Nucl. Inst. and Methods in Phys. Res., Sect. B **127** (1997) 301.
- [**Reed 1977**] D. J. Reed, Radiation Effects, **31**, (1977) 129-147.
- [**Rebut et al. 1991**] P. H. Rebut, M. L. Watkins, D. J. Gambier, and D. Boucher, Phys. Fluids B **3** (8) (1991) 2209-2219.
- [**Smith et al. 1996**] D. L. Smith, H. M. Chung, B. A. Loomis and H.-C. Tsai, J. of Nucl. Mater **223-237** (1996) 356.
- [**Schroeder 1983**] H. Schroeder, Radiation Effects, **78** (1983) 297-314.

[Schut *et al.* 1998] H. Schut, A. van Veen, F. Labohm, A. V. Fedorov, E. A. C. Neeft, R. J. M. Konings, E-MRS spring meeting, 1998, Nucl. Inst. and Meth. B **147** (1-4) (1998) 212-215.

[Stanley *et al.* 1972] J. T. Stanley, J. M. Williams, W. E. Brundage and M. S. Wechsler, Acta Met. **20**, **191** (1972).

[Trinkaas 1986] H. Trinkaas, Radiation Effects, **101** (1986) 91-107.

[Ullmaier 1984] H. Ullmaier, Nuclear Fusion, **24** (8) (1984) 1039-1083.

[Van der Laan *et al.* 1997] J. G. van der Laan, Progress report 1997 on Fusion Technology Tasks, ECN-C-98-037.

[Van der Laan *et al.* 1998] J. G. van der Laan, K. Bakker, R. Conrad, M. P. Stijkel, N. Roux and H. Werle, Proceedings CBBI-7, NRG Report 21099/99.23482, Petten, February 1999, 6/29-38, 4-9.

[Van Gorkum and Kornelson 1979] A. A. van Gorkum, E. V. Kornelson, Radd. Eff. **42** (1979) 93-111.

[Van Veen *et al.* 1980] A. van Veen, A. Warnaar and L. M. Caspers, Vacuum **30** (1980) 109.

[Van Veen *et al.* 1983] A. van Veen A., J. H. Evans, W. Th. M Buters and L. M. Caspers, Rad. Eff., **78** (1983) 53-66.

[Van Veen *et al.* 1983] A. van Veen, J. H. Evans, W. Th. M Buters and L. M. Caspers, Rad. Eff. Vol. **78** (1983) 53-66.

[Van Veen *et al.* 1988] A. van Veen, P.C. de Jong, K. R. Bijkerk, H. A. Filius, J. H. Evans, (eds. M.J.Aziz, L.E. Rehn and B. Stritzker), Mat. Res. Soc. Proc. **100** (1988) 231-236.

[Van Veen *et al.* 1990] A. van Veen, H. Schut, J. de Vries, R. A. Hakvoort and M. R. Ijpma in: American Institute of Physics conference proceedings 218, *Positron beams for solids and surfaces* (eds. P.J. Shultz, G.R. Massoumi, P.J. Simpson) (1990).

- [**Van Veen 1991**] A. van Veen in: *Fundamental Aspects of Inert Gases in Solids*, NATO ASI series B, Physics 279 (eds. S. E. Donnelly and J. H. Evans), Plenum Publishing Corp., New York, USA (1991) 41-57.
- [**Van Veen et al. 1994**] A. van Veen, H. Eleveld and M. Clement, *J. of Nucl. Mater* **212-215** (1994) 287-292.
- [**Van Veen et al. 1995**] A. van Veen, H. Schut, A. V. Fedorov, R. A. Hakvoort and K.T. Westerduin in: *Microstructure of Irradiated Materials*, eds. I. M. Robertson, S. J. Zinkle, L. E. Rehn, W. J. Phythian, Materials Research Society Symposium .Proceedings **373** (1995) 499-504.
- [**Van Veen et al. 1996 MRS**] A. van Veen, H. Schut, A. Rivera, A. V. Fedorov, *Mat. Res. Soc. Symp. Proc.*, editors D.B. Poker, D. Ila, Y-S. Cheng, L. R. Harriot, T. W. Sigmon, **396** (1996) 155-160.
- [**Van Veen et al. 1996 Vanadium Workshop**] A. van Veen, A. V. Fedorov, A. I. Ryazanov, in *Proceedings of the 2nd Workshop on Vanadium Alloy Development for Fusion*, IEA Vanadium Alloy Working Group ECN Petten, 20-22 May 1996, The Netherlands, editor E.V. van Osch, 47-48.
- [**Van Veen et al. 1998 ICFRM-7**] A. van Veen, A. V. Fedorov, A. I. Ryazanov, *J. of Nuclear Materials*, **258-263** (1998) 1400 – 1403.
- [**Van Veen et al. 1998, E-MRS**] A. van Veen, H. Schut, A. V. Fedorov, E. A. C. Neeft, R. J. M. Konings, B. J. Kooi, J. Th. M. de Hosson, *E-MRS spring meeting, 1998, Strasbourg, Nucl. Inst. and Methods in Phys. Res., Sect. B* **147** (1-4) (1998) 216-220.
- [**Van Veen et al. 1999**] A. van Veen, H. Schut, A. V. Fedorov, F. Labohm, E. A. C. Neeft, R. J. M. Konings, *Nucl. Instr. and Methods in Phys. Res., Sect. B* (**148**) 1-4 (1999) 768-772.
- [**Van Wieringen and Warmoltz 1956**] A. van Wieringen and N. Warmoltz, *Physica* **XII** (1956) 849-865.
- [**Vassen et al. 1991**] R. Vassen, H. Trinkaus, P. Jung, *Phys. Rev. B* **44** 9 (1991) 4206-4213.
- [**Wampler 1984**] W. R. Wampler, *J. of Nucl. Mater.*, **122-123** (1984) 1598-1602.

[Wampler 1992] W. R. Wampler, J. of Nucl. Mater., **196-198** (1992) 981-985.

[White *et al.* 1998] C. W. White, J. D. Budai, S. P. Withrow, J. G. Zhu, E. Sonder, R. A. Zuhr, A. Meldrum, D. M. Hembree, D. O. Henderson, S. Praver, Nucl. Instr. and Meth. in Phys. Res. **B 141** (1998) 308-311.

[Wong-Leung and Williams 1996] J. Wong-Leung and J. S. Williams, Nucl. Instr. and Meth. in Phys. Res. **B 118** (1996) 34-38.

[Zhu *et al.* 1999] X. Zhu, J. S. Williams and J. C. McCallum, Nucl. Instr. and Meth. in Phys. Res. **B 148** (1999) 308-311.

[Ziegler *et al.* 1985] J. F. Ziegler, J. P. Biersack, V. Littmark, *The Stopping and Range of Ions in Solids*, ed. J. F. Ziegler, Pergamon Press (1985).

[Zimmerman *et al.* 1998] R. L. Zimmerman, D. Ila, E. K. Williams, S. Sarkisov, D. B. Poker, D. K. Hensley, Nucl. Instr. and Meth. in Phys. Res. **B 141** (1998) 308-311.

[Zinkle and Kinoshita 1997] S. J. Zinkle and C. Kinoshita, J. Nucl. Mat. **251** (1997) 200

ACKNOWLEDGEMENTS

During my work on this Ph.D. project I have been fortunate to meet many people whose impact on myself, and thus as a consequence on this thesis, I would like to acknowledge.

In the first place I would like to thank Tom van Veen who made the research described in this thesis possible. His help in the interpretation of the experimental results, and his insights and discussions have been invaluable. I would also like to thank my other promoter Hugo van Dam for his interest in my work and his critical comments on the manuscript of this thesis. I am very grateful to Alexander Ryazanov who applied a lot of effort to arrange my first visit to Holland. Although from faraway, he always was keen to discuss the physical aspects of this project. Looking back to my friends and colleagues in Moscow I would like to acknowledge the contribution of Volodia Borodin who has helped me a lot with the thermodynamic models included in MODEX.

I would like to thank Henk Schut for his assistance in performing VEP measurements. His help in the interpretation of experimental results with the VEPFIT program was invaluable. Special thanks go to Freek Labohm for the NDP measurements and his moral support in our small "Delphi/Pascal" lobby within the IRI Fortran community. I am also very grateful to Peter Mijnders for his critical comments on the manuscript of this thesis both on physics and language.

Most of the work presented in Chapters 4, 5 and 6 was performed in collaboration with NRG Petten (at that time still ECN). It was a great pleasure to meet many people from this organization. Among them I would like to thank Jaap van der Laan and Klaas Bakker for their constant interest in my work and many fruitful discussions we had in Petten.

I have also enjoyed the collaboration with the RU Groningen. I would like to thank Jeff de Hosson for his interest in MODEX simulations and Bart Kooi for the wonderful TEM pictures, which I also used for the cover of this thesis.

During my work on vanadium alloys I was fortunate to meet John Evans. Discussions with him full of wisdom and humor were very helpful in the preparation of my first paper.

I would like to use this opportunity to thank Hideki Matsui for his warm hospitality during my short visit to Sendai in 1997. Numerous discussions we had on He trapping in vanadium alloys were both fruitful and enjoyable, especially those of them which took place in the sushi-bars.

Technical support in any experimental work is difficult to overestimate. I am very grateful to Kees Westerduin, Bob Heijenga and Jan de Roode for their willingness to respond on my SOS calls.

Very special thanks also go to the secretaries Riny Purmer and Sonja Jobse for their professional help and numerous splendidly organized outdoors activities.

During my first years in the IRI I was surrounded by a number of Dutch students who were the first to introduce me to Holland and the Dutch culture. Among them I would like to mention Trude Buitenhuis and Gerdjan Busker. Their attempts to feed me with peppermint drops are still one of the most striking and unforgettable experiences. Later, the group became much more international and that enriched my background about other foreign cultures. In this contents I would like to thank Lars Jorgensen for his multiple attempts to learn "many physics lessons from a glass of beer". I hope we can resume these studies some time in the future. My friendship with Todd Adams helped me to enjoy my stay in Holland during our numerous weekend-trips in the search for adventures. During the last couple of years our group was reinforced by a number of Spanish PhD students. Thanks to Antonio Rivera, Ramon Escobar, Alfonso Alba and Iciar Montilla I realized that siesta is not a stand-alone "activity" but is a direct and inevitable consequence of a Spanish lunch. I would like to thank my partner in "nanocluster business" Marijn van Huis for his support in fighting with the DANFYSIK accelerator. I am also indebted to many others in the group: Olof Dankert, Erika Neeft,

Claudiu Falub, Elena Abadjieva, all of you have helped me carry the burdens of the PhD student's life.

This acknowledgments would not be full without thanking my family for the love and support I always felt despite the distance of more than 2000 km separating Delft from Moscow.

CURRICULUM VITAE

The author of this thesis was born in Moscow on February 7, 1963. Between 1970 and 1980 he received primary and secondary education in Moscow. In 1980 he passed the entering exams to the Moscow Engineering Physics Institute, faculty of Theoretical and Experimental Physics. After graduating in 1986 and acquiring the diploma of Nuclear Experimental Physics he started his work in the Russian Research Center "Kurchatov Institute" as an engineer in the group "Radiation defects of materials". From October 1993 to October 1994 he was working in the Interfaculty Reactor Institute in a framework of the collaboration project between IRI and RCC "Kurchatov Institute". In February 1995 he returned to the Defects in Materials group in the IRI to start the Ph.D. project which lasted until March 1999. The results of that work are presented in this thesis.

